

2016

Particle tracking and inference in fluorescence microscopy

<https://hdl.handle.net/2144/19446>

Boston University

BOSTON UNIVERSITY
COLLEGE OF ENGINEERING

Dissertation

**PARTICLE TRACKING AND INFERENCE IN
FLUORESCENCE MICROSCOPY**

by

TREVOR THOMAS ASHLEY

B.S., Harvey Mudd College, 2009

Submitted in partial fulfillment of the
requirements for the degree of
Doctor of Philosophy

2016

© 2016 by
TREVOR THOMAS ASHLEY
All rights reserved

Approved by

First Reader

Sean B. Andersson, PhD
Associate Professor of Mechanical Engineering
Associate Professor of Systems Engineering

Second Reader

John Baillieul, PhD
Distinguished Professor of Mechanical Engineering
Distinguished Professor of Systems Engineering
Distinguished Professor of Electrical and Computer Engineering

Third Reader

Michael L. Smith, PhD
Associate Professor of Biomedical Engineering

Fourth Reader

Hua Wang, PhD
Associate Professor of Mechanical Engineering
Associate Professor of Systems Engineering

*Ich habe keine besondere Begabung,
sondern bin nur leidenschaftlich neugierig.*
Albert Einstein, 1952

Acknowledgments

Thank you to my family, Larry, Donna, and Brent, for always offering their support and encouragement when I needed it.

Thank you to the teachers who encouraged me to pursue my potential. To Bob Newell for inspiring me to pursue math even though I was terrible at it. To Bob Schaffer for showing me how powerful a Fourier transform could be. To Anthony Bright for showing me the beauty of chaotic systems. To Sarah Harris for showing me how to make a symphony out of 0's and 1's.

Thank you to my ESI colleagues, Mychal H., Mark P., Joe F., and Mark M., for encouraging me to pursue graduate school despite losing me as a team member.

Thank you to my best friend, Stephani, for offering her friendship over the years I've known her (which seems like forever) despite living thousands of miles away.

Thank you to my friends and labmates, Peter, Peng, Catherine, Aditi, Brian, Xi, and Jeff, for giving me memories to last a lifetime.

Thank you to all of my middle school students at Atlantic Middle School during my time as a GK-12 fellow. You-all taught me more than I taught you.

Thank you to my committee members for graciously taking the time to review this work and suggest improvements.

Thank you to the National Science Foundation (grants CMMI-0845742 and DBI-1352729) for graciously funding my research.

And last, but certainly not least, thank you to my advisor, Sean Andersson, for spending hundreds (if not thousands!) of hours mentoring me and shaping me into a better engineer, presenter, researcher, and teacher.

PARTICLE TRACKING AND INFERENCE IN FLUORESCENCE MICROSCOPY

TREVOR THOMAS ASHLEY

Boston University, College of Engineering, 2016

Major Professor: Sean B. Andersson, PhD
Associate Professor of Mechanical Engineering
Associate Professor of Systems Engineering

ABSTRACT

Observing biophysical phenomena at the nanometer scale with both high spatial and temporal resolution is a challenging feat. Although many techniques, including atomic force microscopy and scanning electron microscopy, have demonstrated subnanometer spatial resolution, most exhibit drawbacks which limit their temporal resolution. On the other hand, light microscopy exhibits poor spatial resolution (typically greater than 100 nm) due to diffraction. The desire to image features below the resolution of light has spawned the term *super-resolution microscopy* to which many powerful, albeit complicated, techniques may be associated; such techniques include Stimulated Emission-Depletion Microscopy (STED) and Stochastic Optical Reconstruction Microscopy (STORM). Within the field of super-resolution there exists a subset of methods which involve tagging features of interest (e.g., a virus or motor protein) with small, fluorescent molecules and measuring their emitted fluorescence over time. Although the emitted light is diffraction-limited, the precision of localizing the position of the molecule is proportional to the number of photons acquired. Thus, fluorescent particle tracking is a method which augments traditional light microscopy

so that features may be localized to spatial resolutions below the diffraction limit while still maintaining useful temporal resolutions.

One common approach for tracking fluorescent particles involves *passively* observing the particle with a stationary detector; this approach, however, is limited by its inability to observe particles in three dimensions over a large field of view. Consequently, specialized techniques have been developed that *actively* track the particle, but the majority of these methods, unfortunately, utilize non-standard optical paths which complicate their use. Moreover, analysis methods pertaining to both paradigms, which infer both position locations and model-based parameter estimates, are often subjective or employ simplified and potentially inaccurate models. In widefield microscopy, for example, the common approach involves first localizing the particle within each image via a heuristic method, such as calculating the centroid, and then inferring diffusion coefficients by regressing to the mean squared displacement. This approach to localization disregards information involving the optical setup (e.g., the point spread function, aberrations, and noise) as well as information regarding the particle's motion. Although methods exist for optimally calculating diffusion coefficients, they are limited to the case of unconfined diffusion with measurements corrupted by additive, white noise.

The work in this thesis provides two specific contributions. The first presents an active approach to tracking a single fluorescent particle in three dimensions that requires no specialized hardware aside from a standard confocal microscope. Inspired by works involving the autonomous exploration of unknown potential fields, the algorithm operates by moving the microscope's focal volume toward the maximum of the field of light emitted by the particle. For a stationary particle and a radial field, an equilibrium trajectory is derived and its local stability is proven. In addition, the algorithm's ability to track both stationary and diffusive particles is numerically char-

acterized. The second contribution presents the application of a numerical, iterative algorithm to the problem of simultaneously inferring both location and model parameters from particle tracking data of potentially nonlinear and non-Gaussian imaging modalities. The method, which is leveraged from the field of system identification, employs Sequential Monte Carlo methods in conjunction with the Expectation Maximization algorithm to provide approximate maximum likelihood estimates of model parameters (e.g., diffusion coefficients) as well as approximate posterior probability densities of the particle's location over time. The effectiveness of the method is demonstrated through numerical simulations of two- and three-dimensional motion (including free, confined, and tethered diffusion) imaged in a widefield context. Lastly, the effectiveness of both methods is demonstrated by tracking a quantum dot in a hydrogel with the proposed tracking method and by analyzing the resulting data using the aforementioned inference method.

Contents

1	Introduction	1
1.1	Biological Imaging at the Nanometer Scale	1
1.2	Tracking Fluorescent Particles	5
1.2.1	Passive Tracking Methods	7
1.2.2	Active Tracking Methods	11
1.3	Inference from Particle Tracking Experiments	13
1.4	Contributions and Organization of Thesis	16
2	Tracking a Fluorescent Source via Extremum Seeking	19
2.1	Overview of Confocal Microscopy	20
2.2	Problem Statement	23
2.3	A Stationary Particle with Unbounded Support of PSF	25
2.3.1	Existence of Equilibrium Trajectory	26
2.3.2	Stability of Equilibrium Trajectory	28
2.3.3	Numerical Characterization of Equilibrium Trajectory	31
2.4	A Diffusing Particle with Bounded Support of PSF	35
2.4.1	Approximate Formula for First Passage Time	37
2.4.2	Numerical Characterization of First Passage Time	42
2.5	Summary	47
3	Inference for Particle Tracking Experiments	49
3.1	Problem Statement	50
3.2	The Expectation Maximization Algorithm	52

3.2.1	Sequential Monte Carlo	54
3.3	Relevant Models in Fluorescence Microscopy	56
3.3.1	Brownian Motion	56
3.3.2	Diffusive Directed Motion	58
3.3.3	Confined Diffusion	59
3.3.4	Elastic Tethering	60
3.3.5	Normally Distributed Initial Condition	63
3.3.6	Poissonian Shot Noise	63
3.4	Demonstration: Widefield Fluorescence	65
3.4.1	Generation of Ground-Truth Data	66
3.4.2	Algorithm Implementation	70
3.4.3	Metrics for Algorithm Performance	71
3.4.4	Demonstration No. 1: Two-Dimensional Diffusion	74
3.4.5	Demonstration No. 2: Axially-Confined Diffusion	78
3.4.6	Demonstration No. 3: Three-Dimensional Elastic Tethering	81
3.4.7	Demonstration No. 4: Elastic Tethering with Unknown PSF	84
3.5	Summary	86
4	Tracking a Quantum Dot within a Hydrogel	89
4.1	Confocal Microscope Setup	90
4.2	Characterization of Confocal PSF	90
4.3	Experiment Details	94
4.4	Experiment Results	96
4.5	Summary	97
5	Summary and Future Directions	101
5.1	Summary	101
5.2	Future Directions	103

5.2.1	Discrete-Time Analysis of Stability	103
5.2.2	Accounting for Motion Blur	103
5.2.3	Non-Markovian Dynamics	104
A	Summary of Sequential Monte Carlo Methods	105
A.1	Sampling Importance Resampling Algorithm	105
A.2	Forward-Filtering Backward-Smoothing Algorithm	107
	References	108
	Curriculum Vitae	117

List of Tables

3.1	Parameter values used in the generation of ground-truth data and for each of the four widefield imaging demonstrations.	67
-----	---	----

List of Figures

1·1	A common setup for tracking fluorescent particles in a passive widefield setting. Here, a white excitation source is filtered to a specific bandwidth of wavelengths (shown in blue). The filtered excitation light is reflected by a dichroic mirror and focused by the objective onto the sample. The fluorescent particles (shown as red dots within the sample) react to the excitation light and emit a different color light (shown in red). The emitted light passes through the dichroic and through another filter. It is then focused onto a detector, such as a camera.	8
2·1	A ray diagram of a confocal microscope. Here, an excitation source (shown in blue) is passed through a pinhole and reflected to the objective lens by a dichroic. The objective lens focuses the excitation light onto the focal plane of the sample (shown as a black line contained within a gray rectangle). The light emitted by the fluorophore (shown in red) is collected by the objective lens and passed through the dichroic. The emitted light is then passed through another pinhole which is confocal to the excitation pinhole. The intensity of the light is then measured by an avalanche photodiode. Note that the out of focus light (shown by the dashed magenta and orange rays) are not confocal with either pinhole and are subsequently blocked.	21

2·2	A theoretical model of the confocal point spread function (PSF) shown in two different planes. The picture on the left shows a cross-section of the PSF within the focal plane, and the picture on the right shows a cross-section along the axial plane. Note the differences in axis lengths. Image reproduced from (Andersson, 2011).	22
2·3	A typical trajectory for the proposed tracking controller. In the figures shown in the top row, the deviation $(\tilde{x}, \tilde{y}, \tilde{z})$ of the focal volume from the particle is shown in blue whereas the equilibrium trajectory $(\bar{x}, \bar{y}, \bar{z})$ is shown in gray. Here, the deviation asymptotically approaches the equilibrium trajectory in all three axes. In the figures in the bottom row, the error between the deviation and the equilibrium trajectory is shown in blue; we also plot the resulting linearized error (shown in red) as well as the averaged linearized error (shown in dashed black). In all three axes, the errors asymptotically approach zero. Here, the controller parameters were $\omega_1 = 100$ Hz, $\omega_2 = 10$ Hz, $K_p = 0.005$, and $\bar{R} = v/\omega_1 = 0.1$. The PSF was assumed parabolic with the maximum located at the origin.	32
2·4	Stability regions of linear time-varying system (2.12) for three distinct values of ϵ defined in (2.14) as given by the numerical evaluation of the monodromy matrix (2.19). The grey dots indicate the region where the linear time-varying system is stable (<i>i.e.</i> , where the eigenvalues of the monodromy matrix are strictly within the unit circle), whereas the red x's mark the region of instability (<i>i.e.</i> , where the eigenvalues are on or outside the unit circle). Note that the size of the instability region increases as ϵ increases. Also note that the region of instability lies strictly above the solid black line $\omega_1 = \omega_2$	35

2.5	A one-dimensional illustration of a bounded field. The width of the field is R^* and is assumed to be radial about the maximum x^* . When the distance between the focal volume and the maximum exceeds R^* (red region), the PSF becomes constant and the particle becomes untrackable.	36
2.6	A two-dimensional illustration depicting the definition of tracking loss as defined by the stopping time (2.24). The coordinate axis is centered at the particle's location \mathbf{x}^* which exhibits a point spread function of radius R^* (shown as the dashed circle). There are three smaller circles depicting different focal volume locations relative to \mathbf{x}^* , and the center of each circle is $\mathbf{x}_s + \bar{\mathbf{x}}$ which is the position of the focal volume \mathbf{x}_s in addition to the steady state trajectory $\bar{\mathbf{x}}$. Since the steady state trajectory is periodic with amplitude $\bar{R} = v/\omega_1$, the effective radius of each circle is shown by the smaller solid circles of radius \bar{R} . The first circle, shown in green and residing in quadrant I, does not satisfy the stopping criterion $\ \mathbf{e}\ < R^* - \bar{R}$ and is therefore trackable. The second circle, shown in yellow and residing in quadrant IV, satisfies the stopping criterion and indicates the point at which tracking would first be lost. The third circle, shown in red and residing in quadrant III, details the scenario where the particle has significantly deviated from the focal volume and therefore cannot be reliably tracked.	38
2.7	A comparison among the theoretical expected first passage time (2.32) (denoted as a solid line) and numerical simulations of the nonlinear system (2.25) (denoted by 'x' markers) and the linear-averaged system (2.26) (denoted by 'o' markers).	44

- 2·8 The expected first passage time (2.32) as a function of the tracking radius $\bar{R} = v/\omega_1$ as K_p increases. The point spread function for this figure was parabolic with a radius $R^* = 1$ and the particle location was diffusing with $D = 1.0$. Relatively low values of K_p are shown by dash-dotted curves in red and orange, and relatively large values are shown by dashed curves in green, blue, and violet. The black solid curve represents the expected first passage time at the bifurcation point which is denoted by the ‘x’ marker. Note that for small values of K_p the optimal tracking radius is zero; this indicates that if K_p is too low, then the expected first passage time will be maximized by not tracking at all. When K_p is increased to a critical value, however, the optimal tracking radius discontinuously changes to the solid vertical line (here, $R_{\text{Bif}} \approx 0.34$). As K_p is subsequently increased beyond the bifurcation point, the expected first passage time increases in conjunction with the optimal tracking radius. 46
- 3·1 Box plots of the estimated diffusion coefficients as a function of the number of iterations of the SMC-EM algorithm for the first demonstration (2D diffusion, Sec. 3.4.4). The edges of the box represent the first and third quartiles, the red line is the median, the vertical dashed line indicates the bounds for data within 1.5 times the interquartile range, and the red + symbols are data points outside this range. The true values of the diffusion parameters, indicated by the solid black lines, were $D_x = D_y = 0.01 \mu\text{m}^2/\text{s}$ 77

3.2	Box plots of the root mean square (RMS) localization error as a function of the number of iterations of the SMC-EM algorithm for the first demonstration (2D diffusion, Sec. 3.4.4). The edges of the box represent the first and third quartiles, the red line is the median, the vertical dashed line indicates the bounds for data within 1.5 times the interquartile range, and the red + symbols are data points outside this range.	78
3.3	This figure illustrates a typical trajectory from the two-dimensional diffusion in the first demonstration (2D diffusion, Sec. 3.4.4); only the x axis results are shown; y axis results were similar in appearance. The random walk shown in gray represents the true position of the particle over time. The red dots indicate the Gaussian fit (GF) estimates and the red error bars are the 3σ uncertainties of these estimates as determined via maximum likelihood estimation (Michalet and Berglund, 2012). The shaded regions represent the approximate posterior probability densities for the particle positions after ten iterations of the SMC-EM algorithm.	79

- 3.4 Box plots of the estimated parameters as a function of the number of iterations of the SMC-EM algorithm for the second demonstration (confined diffusion, Sec. 3.4.5). In this case, the z position of the diffusing particle was confined to the interval $[-L/2, L/2]$; the diffusion coefficients D_x, D_y, D_z and the confinement length L were assumed unknown. The edges of the box represent the first and third quartiles, the red line is the median, the vertical dashed line indicates the bounds for data within 1.5 times the interquartile range, and the red + symbols are data points outside this range. The true values, indicated by the solid black lines, were $D_x = D_y = D_z = 0.01 \mu\text{m}^2/\text{s}$ and $L = 0.5 \mu\text{m}$. 82
- 3.5 Box plots of the root mean square (RMS) localization error as a function of the number of iterations of the EM algorithm for the second demonstration (confined diffusion, Sec. 3.4.5). The edges of the box represent the first and third quartiles, the red line is the median, the vertical dashed line indicates the bounds for data within 1.5 times the interquartile range, and the red + symbols are data points outside this range. The raw RMS errors for z are indicated in the right-most figure as gray boxes (with outliers denoted by red diamonds), whereas the RMS errors for the absolute value of z are indicated by blue boxes. . 83

3.6 A typical z trajectory from the second demonstration (confined diffusion, Sec. 3.4.5). Here, the true trajectory is shown in grey and the posterior density estimates after ten iterations of the SMC-EM algorithm are shown with values according to the color bar. Note that estimates occur only every 100 ms while the true trajectory is defined (essentially) continuously. The dashed lines indicate the focal plane (at $z = 0$) and the bounds of the channel ($z = \pm 0.25 \mu\text{m}$). From this figure, it is clear that the PSF's symmetry about the focal point at $z = 0$ creates potential localization error in which the trajectory is essentially reflected through the focal plane (for example, from time 0 s to approximately 1 s and again from approximately 4.5 s through the end at 10 s). We note that this phenomenon is solely due to the PSF's symmetry about the focal point and is exhibited by all localization algorithms; PSFs that are asymmetric will not produce this behavior. Use of the motion model and the entire set of data prevent the estimates from randomly changing their sign relative to the focal plane and thus the motion model parameters can still be effectively estimated. 84

- 3·7 Box plots of the estimated parameters as a function of the number of iterations of the SMC-EM algorithm for the third demonstration (3D tether, Sec. 3.4.6). In this case, the particle was assumed to be elastically tethered to a known location; the stiffness coefficient A and the diffusion coefficient D were assumed unknown. The edges of the box represent the first and third quartiles, the red line is the median, the vertical dashed line indicates the bounds for data within 1.5 times the interquartile range, and the red + symbols are data points outside this range. The true values, indicated by the solid black lines, were $A = 1.0 \text{ s}^{-1}$ and $D = 0.01 \text{ } \mu\text{m}^2/\text{s}$ 85
- 3·8 Box plots of the root mean square (RMS) localization error as a function of the number of iterations of the SMC-EM algorithm for the third demonstration (3D tether, Sec. 3.4.6). The edges of the box represent the first and third quartiles, the red line is the median, the vertical dashed line indicates the bounds for data within 1.5 times the interquartile range, and the red + symbols are data points outside this range. The raw RMS errors for z are indicated in the right-most figure as gray boxes (with outliers denoted by red diamonds), whereas the RMS errors for the absolute value of z are indicated by blue boxes. 86

- 3·9 Box plots of the estimated parameters as a function of the number of iterations of the SMC-EM algorithm for the fourth demonstration (3D tether with unknown G , Sec. 3.4.7). In this case, the particle was assumed to be elastically tethered to a known location; the stiffness coefficient A , the diffusion coefficient D , and the peak fluorescence intensity G were assumed unknown. The edges of the box represent the first and third quartiles, the red line is the median, the vertical dashed line indicates the bounds for data within 1.5 times the interquartile range, and the red + symbols are data points outside this range. The true values, indicated by the solid black lines, were $A = 1.0 \text{ s}^{-1}$, $D = 0.01 \text{ } \mu\text{m}^2/\text{s}$, and $G = 100 \text{ counts}$ 87
- 3·10 Box plots of the root mean square (RMS) localization error as a function of the number of iterations of the SMC-EM algorithm for the fourth demonstration (3D tether with unknown G , Sec. 3.4.7). The edges of the box represent the first and third quartiles, the red line is the median, the vertical dashed line indicates the bounds for data within 1.5 times the interquartile range, and the red + symbols are data points outside this range. The raw RMS errors for z are indicated in the right-most figure as gray boxes (with outliers denoted by red diamonds), whereas the RMS errors for the absolute value of z are indicated by blue boxes. 88

- 4.1 In image of the confocal microscope used for the experiment described in this work. The device is based upon a Zeiss Axiovert 200 inverted microscope which can operate in both widefield and confocal modes. The devices contains an internal dichroic (not shown) which reflects the excitation source (shown in red) to a 3D piezoelectric nanostage (shown in dashed orange). The nanostage holds the specimen and can displace it in three dimensions. The fluorescence generated by the specimen is passed through the dichroic and is reflected to both the pinhole (shown in green) and the CCD camera (shown in purple) by a beam splitter. In confocal operation the avalanche photodiode (shown in yellow) measures the emitted light, whereas in widefield operation the CCD camera measures it. 91
- 4.2 A block diagram of the optical path for the microscope described in this work. The excitation light (shown in blue) is generated by a laser diode. The light is then reflected off a dichroic, passed through the objective lens, and focused onto the sample. The sample is held by a piezoelectric nanostage. The emitted fluorescence generated by the sample is collected by the objective and passed through the dichroic where it is focused onto a pinhole which is confocal with the laser excitation. The intensity of the emitted light is then measured by the avalanche photodiode. A real-time controller (here, an NI cRIO) observes the APD's intensity measurement and, during tracking, generates real-time position commands to the piezostages. Note that although a beam-splitter reflects some of the emitted light onto a CCD camera, the image is recorded by a host computer and is not used during tracking. 92

4.3	Three-dimensional point spread function (PSF) measurements (left) and the corresponding Gaussian model (right) which was calculated by a nonlinear least-squares fit. Three planes are shown in magenta, orange, and green which enable the depiction of the cross sections shown in Fig. 4.4. These planes were determined by calculating the planes through the estimated particle center, given by the least-squares fit, and normal vectors specified by the three standard Cartesian unit vectors transformed via (4.2) and the three rotations $(\hat{\psi}_x, \hat{\psi}_y, \hat{\psi}_z)$, also given by the least-squares fit. The intensity values in the measured PSF (left) are normalized by the maximum measured intensity value, and the intensity values in the model PSF (right) are normalized by the peak intensity value calculated by least-squares fit.	94
4.4	Two-dimensional point spread function measurements (top row) and their corresponding Gaussian models (bottom row) through the three planes depicted in Fig. 4.3.	95
4.5	The inferred three-dimensional position of a quantum dot, in blue, diffusing in a hydrogel relative to the position of the focal volume, in black, which followed the particle in real-time using the extremum seeking method described in this work. The particle position was inferred by employing the SMC-EM algorithm described in Chapter 3. In the bottom graph, the measured intensity, in black, is shown in relation to the theoretical intensity, in blue, which was calculated by evaluating a Gaussian model of the point spread function (PSF) as a function of the inferred particle position and the measured focal volume position.	99

4.6 The inferred three-dimensional trajectory of a quantum dot diffusing in a hydrogel as parametrized by time. The quantum dot was tracked in a confocal microscope using the method presented in this work; the resulting particle position was inferred using the SMC-EM algorithm described in Chapter 3. 100

List of Abbreviations

AFM	Atomic Force Microscope
APD	Avalanche Photodiode
CCD	Charge-Coupled Device
cRIO	Compact Reconfigurable Input Output
CRLB	Cramér-Rao Lower Bound
DOF	Depth of Field
EFPT	Expected First Passage Time
EKF	Extended Kalman Filter
EM	Expectation Maximization
EMCCD	Electron-Multiplying Charge-Coupled Device
FFBS	Forward-Filtering Backward-Smoothing
FPGA	Field Programmable Gate Array
GF	Gaussian Fit
LSCM	Laser-Scanning Confocal Microscope
MSD	Mean Squared Displacement
ML	Maximum Likelihood
NA	Numerical Aperture
NI	National Instruments
OLSF	Optimal Least Squares Fit
OU	Ornstein-Uhlenbeck
PSF	Point Spread Function
QD	Quantum Dot
RMS	Root Mean Square
sCMOS	Scientific Complimentary Metal-Oxide Semiconductor
SDE	Stochastic Differential Equation
SEM	Scanning Electron Microscope
SIR	Sampling Importance Resampling
SMC	Sequential Monte Carlo

Chapter 1

Introduction

1.1 Biological Imaging at the Nanometer Scale

The understanding of biological phenomena has significantly improved over the recent century due to the development of tools which enable the observation of micro and nanoscale objects. Important examples of these tools, all of which were awarded a Nobel Prize, include the sub-diffraction light microscope by Zsigmondy in 1925, the phase contrast microscope by Zernike in 1953, the electron microscope by Ruska in 1986, and the scanning tunneling microscope by Binnig and Rohrer also in 1986. These inventions, among many others, have been applied to a multitude of applications, including those involving the structure of deoxyribonucleic acid (Driscoll et al., 1990), the human immunodeficiency virus (Fuller et al., 1997), and fibrillar actin (Masai et al., 1991). Although these inventions are particularly momentous, each of them is not without its own set of performance limitations.

Within the field of biological microscopy, one may adjudicate the performance of a microscope by four important criteria. These include (1) its ability to image living (*in vitro* or *in vivo*) systems without extraneous and uncontrollable interference, (2) its spatial resolution, which is preferably small enough to adequately characterize the size and length of the features of interest, (3) its temporal resolution, which should be small enough such that the dynamic behaviors of the organisms are sufficiently captured, and (4) its cost, ease of use, and maintainability. As one may expect, these criteria are codependent and every microscope offers various trade-offs.

A particularly important and commonly used tool in biology is the scanning electron microscope (SEM). The SEM operates by directing a tightly-focused beam of electrons onto the specimen. The energy exchange between the beam and the specimen results in the deflection of electrons that are detected during the imaging process. Perhaps the most substantial benefit of the SEM is its superior spatial resolution which is typically on the order of 10 nanometers for mid-line conventional instruments; the device achieves this, however, by sacrificing its performance among the other three aforementioned criteria. Regarding its ability of imaging living specimens, SEM often requires that the specimen's surface be electrically conductive which is usually achieved by coating the surface with a metal such as gold or by impregnating the material with osmium. Moreover, the specimen chamber must be at a relatively high vacuum for operation. Consequently, the applicability to imaging living specimens within a realistic environment is limited. Although certain techniques exist which may preserve the structure of the specimen prior to coating, this tends to complicate the use of the device. A relatively new mode of operation, Environmental SEM, aims to lift these limitations, but there is currently no commercial device available and it has yet to reach widespread use.

Another important tool used in biology is the atomic force microscope (AFM). The AFM operates by scanning a small, nanometer-scale tip across the specimen surface. As the tip nears the surface, various atomic interactions create attractive and repulsive forces depending on their relative distance. During the imaging process, the tip, which resides at the end of a flexible cantilever, is scanned in a planar raster pattern via an actuator capable of nanometer precision (*e.g.*, a piezoactuator). As the tip interacts with the surface during the imaging process, the axial position of the tip (perpendicular to the specimen plane) is regulated by a feedback loop. Thus, the topography of the specimen may be inferred by observing the axial distance

fluctuations during the scanning process. Much like the SEM, the primary benefit of the AFM is that it is capable of subnanometer spatial resolution; in fact, the primary limiting factor contributing to its spatial resolution is the size of the tip. Unlike the SEM, however, the AFM may be more readily applied to living biological systems since it does not necessarily require operation in a vacuum nor does it require the specimen be conductive. Additionally, with the invention of intermittent-contact (*i.e.*, tapping-mode) AFM, imaging is a relatively non-invasive process. It is to be noted, however, that the AFM can only provide information regarding the structure's surface. Perhaps the biggest limitation of the AFM, unfortunately, is its poor temporal resolution which is due to the raster scanning process. Even though a significant amount of research has been done to improve the imaging process, resulting in both algorithmic and hardware innovations (Leang et al., 2009; Butterworth et al., 2010; Yong et al., 2012; Ando, 2012), commercial AFMs are still limited by their inability to acquire large images of living systems at a reasonably fast rate.

Despite the aforementioned advantages of SEM and AFM, light microscopy remains a very popular method for imaging biological specimens for several reasons. In particular, it can operate in a large variety of media, and, when operated in a widefield manner, can acquire large images at relatively fast frame rates due to the parallel-nature of photon acquisition. Even transparent samples may be imaged with the addition of phase contrast and differential interference optics. Additionally, the imaging process is mostly passive as photons do not significantly influence the specimen, although heating may occur with large intensities. Given these benefits, light microscopy may appear to be an optimal solution to imaging biological specimens. Unfortunately, light microscopy is limited by its poor spatial resolution which is fundamentally limited by diffraction.

An analytical formula for the resolution of a widefield light microscope was dis-

covered by Abbe to be

$$R_{\text{WF}} = \frac{\lambda}{2\text{NA}}, \quad (1.1)$$

where λ is the wavelength of the emitted light and NA is the numerical aperture of the objective lens (Abbe, 1873). Here, R_{WF} denotes the radius of the Airy disk within the image plane. The numerical aperture is directly proportional to the index of refraction of the imaging medium (with common values 1.33, 1.47, and 1.51 for water, glycerol, and oil, respectively) and the sine of the semi-angle of light entering the objective. Since the sine of this semi-angle is bounded by unity, the limiting factor for the numerical aperture (and therefore the resolution of light) is the index of refraction - a value which is governed by the immersion medium. As water is often the preferred medium for biological samples, the NA of objective lenses rarely exceeds 1.3. Thus, a reasonable lower bound on the resolution of light for the visible spectrum is approximately 100 nm.

Unfortunately, this lower bound severely limits the applicability of light microscopy within the field of biology as there are many structures at or below its resolution. For example, several viruses, such as measles, hepatitis, influenza, and the human immunodeficiency virus are all approximately 100 nm in size. Additionally, many critically important biomolecules, including hemoglobin, myoglobin, tRNA, lysozymes, motor proteins, phospholipids, and antibodies, are all approximately 10 nm or smaller in size. Consequently, conventional light microscopy cannot elucidate many biological phenomena that may occur within the cell or its environment.

Given the existence of a multitude of biological structures with features smaller than the diffraction limit of light, much effort has been devoted to inventing devices and algorithms which can transcend this barrier. Over the past few decades, a new category of *super-resolution* techniques has been established; some popular techniques

include Structured Illumination Microscopy (Gustafsson, 2000), Near-field Scanning Optical Microscopy (Betzig and Chichester, 1993), Stimulated Emission-Depletion Microscopy (Hell and Wichmann, 1994), Photoactivated Localization Microscopy (Hess et al., 2006), and Stochastic Optical Reconstruction Microscopy (Rust et al., 2006). Although all of the aforementioned methods have proven successful at imaging living specimens with resolutions far below that of conventional light microscopy, all of them provide varying degrees of performance in terms of their temporal resolution and their ease of use. Details regarding these specific methods are beyond the scope of this work; instead, however, we turn our attention to a class of light-based super-resolution methods which involve tracking fluorescent particles.

1.2 Tracking Fluorescent Particles

One approach to inferring the dynamical characteristics of a biomolecule is by attaching a small fluorescent molecule to it and by measuring the position of the fluorescent molecule over time. These fluorescent molecules, also known as fluorophores, are typically much smaller than the resolution of a light-based microscope, and common choices include proteins, such as green fluorescent protein, dyes, such as rhodamine, or crystals, such as quantum dots. Although the light emitted by the fluorophore is still diffraction-limited, the resulting spatial pattern is predictable and is dependent on the microscope's optical configuration as well as the three-dimensional position of the fluorophore. This pattern is known as the Point Spread Function (PSF) and is reminiscent of the impulse response of linear, time-invariant differential equations. Since the PSF may be mathematically characterized using the theory of optics (Born and Wolf, 1999), the position of the particle may therefore be estimated by some inference procedure, such as a nonlinear regression which minimizes the error between the measured intensity pattern and the predicted intensity pattern given the PSF model

and the position of the particle. Perhaps the most profound utility of this method is governed by the relationship between the localization precision and the number of photons acquired per measurement. In fact, it was shown in (Thompson et al., 2002) that these two quantities are inversely proportional and that the localization precision will asymptotically approach zero given a sufficiently large number of collected photons. Thus, even though the spatial pattern of light is diffraction-limited, the position of the fluorophore can be estimated to within arbitrary precision.

The utility of tracking fluorophores has been demonstrated in several scenarios. For example, single phospholipids were tracked as they diffused on a membrane, and the resulting images allowed the experimenters to localize the particle to within a reported precision of 30 nm (Schmidt et al., 1996). In addition, the motor protein myosin was tagged with a fluorescent molecule and imaged at 30 Hz as it traversed an actin filament (Funatsu et al., 1995); as detector and fluorophore efficiency improved over time it was determined, again via fluorescent particle tracking, that myosin V walked in a hand-over-hand manner (Yildiz et al., 2003). A year later, kinesin was determined to walk in a similar fashion (Yildiz et al., 2004). Furthermore, the mechanisms behind the viral trafficking of influenza were deduced from single particle tracking experiments (Lakadamyali et al., 2004). More recent developments involve the cellular uptake of (HIV1-Tat)-modified nanoparticles (Welsher and Yang, 2014), the structure of intestinal mucous (Macierzanka et al., 2014), and synaptic membrane compartments (Biermann et al., 2014). In fact, super-resolution techniques have become so influential that the 2014 Nobel Prize in chemistry was awarded to Hell, the inventor of STED, as well as Betzig and Moerner, two of the original pioneers of single-molecule microscopy.

Within this thesis, we distinguish between two different categories of tracking methods: *active* methods which localize, seek, or track the particle in real-time, as

well as *passive* methods which do not. To clarify, it is assumed that the categories discussed in the following sections do not influence the particle in any fashion, such as by applying a force to the particle either mechanically or electromagnetically (*e.g.*, via an optical trap). We note, however, that the field of trapping particles is vast and has proven to be very useful to biologists; see, for example, the well-known anti-Brownian electrophoretic trap (Cohen and Moerner, 2005).

1.2.1 Passive Tracking Methods

Perhaps the most common device used for passively tracking fluorescent particles is the widefield epifluorescence microscope. This device, illustrated in Fig. 1-1, consists of two optical paths: an excitation path and an emission path. The excitation path often consists of a white excitation source which is filtered to a bandwidth of wavelengths specific to the fluorophore. The filtered excitation is then reflected off a dichroic mirror and passed through the microscope's objective lens which focuses it onto the sample. When the excitation light interacts with the fluorophore a different color of light is emitted. The emitted light is then collected by the objective and passed through the dichroic and subsequently filtered to remove any extraneous background light. The emitted light is then collected onto an imaging device, such as a Charge-Coupled Device (CCD) camera.

Within the passive paradigm, inferring the particle's location as a function of time occurs after the experiment is complete, and the entire experimental process usually consists of simply taking videos of the fluorophores. After the images have been acquired, the position of each individual particle may be localized and a time-series of its trajectory may be inferred. Clearly, the greatest benefit of this paradigm is the fact that the experimental process is relatively simple to implement since no real-time actuation or online estimation is performed. Additionally, the passive paradigm offers a significant degree of modularity since the method for inference is mostly decoupled

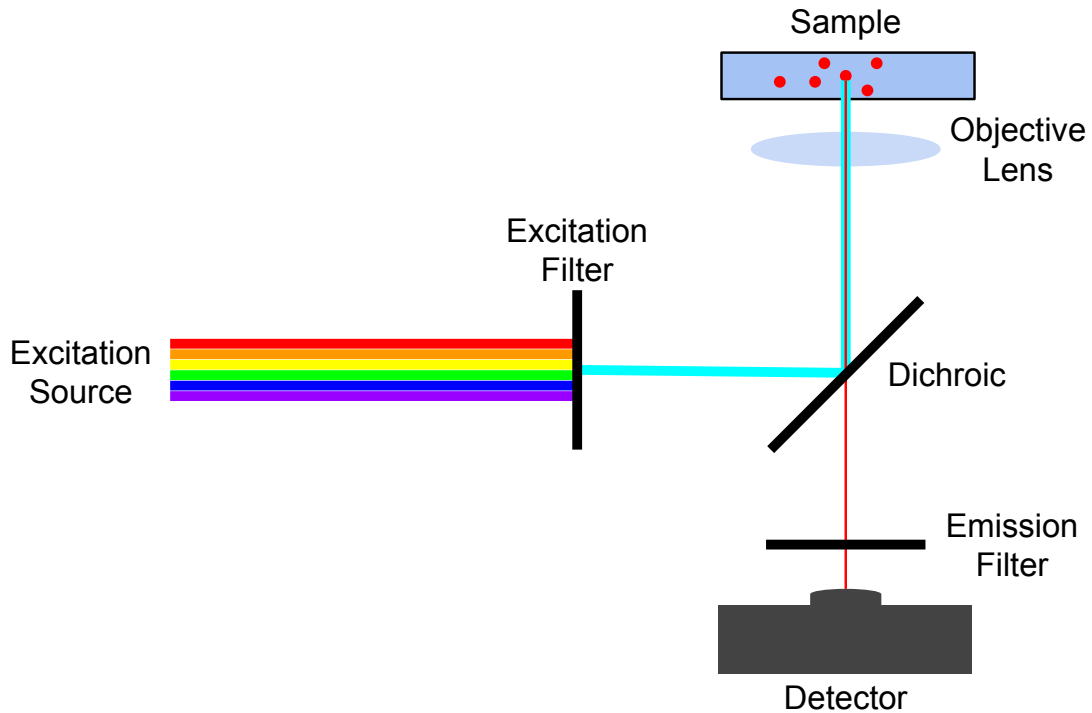


Figure 1-1: A common setup for tracking fluorescent particles in a passive widefield setting. Here, a white excitation source is filtered to a specific bandwidth of wavelengths (shown in blue). The filtered excitation light is reflected by a dichroic mirror and focused by the objective onto the sample. The fluorescent particles (shown as red dots within the sample) react to the excitation light and emit a different color light (shown in red). The emitted light passes through the dichroic and through another filter. It is then focused onto a detector, such as a camera.

from the measurement acquisition process. For example, different cameras, lenses, or dichroics could be interchanged without greatly affecting the inference process. Moreover, since no real-time constraints are imposed during the experiment itself, a large variety of computationally complex algorithms may be used to infer the position of the particle after the experiment is complete.

Although simplicity and modularity are both key benefits of the passive paradigm, it is not without its limitations. Perhaps the most severe limitation of the passive

paradigm is due to the microscope's limited depth of field (DOF). The DOF determines how well the device is able to resolve a particle when it is axially displaced from the plane of focus; the DOF is determined by several factors which include the optical properties of the objective lens and immersion medium, the sensitivity of the optical detector, and the brightness of the fluorophore relative to background noise. For perspective, most widefield fluorescence microscopes rarely exhibit a DOF that exceeds $1 \mu\text{m}$. Considering that biological dynamics are inherently three dimensional, it is probable that one or more particles may move axially outside the DOF during the experiment, and, consequently, would be impossible to localize. Thus, the fact that the passive paradigm does not actively keep particles within the DOF may significantly limit the information acquired during the experiment.

Another significant limitation of the passive paradigm is its inability to produce images which allow for accurate three-dimensional localization. In a standard wide-field fluorescence microscope, the PSF exhibits spatial symmetry about the plane of focus; thus, if one particle is above the focal plane and another is below by an equidistant amount, then the resulting images recorded by the camera for both particles would be identical. Once again, given a scenario where axial motion of the particle is significant, this problem could limit the information acquired during the experiment.

Unlike the depth of field problem which is inherent to the passive paradigm itself, the problem of axial symmetry can actually be resolved and a significant amount of research has been devoted to doing so. One of the earliest attempts, first described in (Kao and Verkman, 1994), used a cylindrical lens within the emission path to induce an asymmetric astigmatic aberration into the PSF. This approach was successfully applied in the context of imaging clathrin-coated pits in BS-C-1 cells where the experimenters achieved a 50-60 nm axial resolution using a technique known as STORM

(Huang et al., 2008). A different technique, first proposed in (Prabhat et al., 2004), required a beamsplitter to split the emitted light onto two distinct detectors which are positioned at different optical distances relative to one another. Since two optical “sections” are acquired simultaneously, the axial position of the fluorophore can therefore be inferred. A minor extension to this method which only required a single detector was presented in (Toprak et al., 2007); the method was applied in the context of imaging large ($4\ \mu\text{m}$) beads in (Juetten et al., 2008) where they achieved an axial resolution of $75\ \text{nm}$ when imaged in conjunction with a technique known as PALM. Another distinct approach placed a tilted mirror behind the sample which reflected emitted light back through the objective and thus created a virtual image which could be detected and decoded (Tang et al., 2010). Another approach used single-photon interferometry to provide axial information (Shtengel et al., 2009). A recent development introduced specifically engineered phase masks that distorted the PSF in a user-specified manner. One example of this was the “double-helix” PSF which resulted in a spatial pattern consisting of two distinct lobes that rotated about a fixed axis as the particle moved axially (Pavani et al., 2009). Very recent improvements in the field of PSF engineering have produced PSFs with resulting DOFs of nearly $20\ \mu\text{m}$ with the introduction of the “tetrapod” pattern (Shechtman et al., 2015); it is to be noted, however, that PSFs offering large DOFs often result in relatively poor localization precision.

In light of the advantages offered by the passive tracking paradigm, which include its ease of use, its modularity, and, with the addition of specialized optics, its ability to produce images which allow for three-dimensional localization, the paradigm is ultimately best-suited for the scenario where several particles are to be imaged over a small axial range of motion and all of which move with timescales longer than $100\ \text{ms}$. The reason for this timescale limitation is mostly due to the limited frame

rates available from common, commercially available cameras. In the case where a particle is moving with a timescale much faster than that of the acquisition period of the camera, a phenomenon known as motion blur occurs which is an additional noise source that reduces the precision of localization. Thus, there is a need for optical devices that are capable of tracking particles over a large range of motion and that can acquire measurements with periods much faster than 100 ms. In this regime, active tracking methods offer much value.

1.2.2 Active Tracking Methods

The problems encountered by the aforementioned passive tracking methods may be circumvented by employing one of several techniques which actively follow the particle of interest as it moves throughout its environment. To accomplish this, a large number of methods localize the particle in real-time and use the resulting estimated position in a feedback algorithm that reduces the tracking error. In the context of two-photon imaging, one such method localized the particle by scanning a laser beam in a circular fashion centered about the estimated particle center; axial information was provided by scanning circles in two separate axial planes (Levi et al., 2003; Ragan et al., 2006). In contrast, a different method localized the particle by measuring the intensity at a finite set of points around the particle; this constellation of points were optimal in the sense that they provided a minimum variance unbiased estimate of the particle location when localized with the fluoroBancroft algorithm (Andersson, 2008; Shen and Andersson, 2011; Shen and Andersson, 2012).

Both of the aforementioned methods are limited in their ability to track quickly moving particles due to the time required in obtaining intensity measurements that allowed for the particle to be localized in real-time. While the former method was limited by the maximum angular speed of the circle and the time to switch between axial planes, the latter was limited by the time it took to travel to each constellation

point. Clearly, if more focal volumes were added so that more measurements could be performed in parallel, then the quality of tracking could be improved. Consequently, a high-speed dual-beam instrument was built which demonstrated the effectiveness of the active paradigm by tracking particles with diffusion coefficients up to $20 \mu\text{m}^2/\text{s}$ (McHale et al., 2007); it is to be noted, however, that despite being able to track quickly diffusing particles, this particular device resulted in a relatively poor localization precision (352 nm lateral and 272 nm axial). To avoid scanning multiple beams, different approaches were developed which instead localized the particle using multiple independent avalanche photodiodes (Cang et al., 2007; Han et al., 2012). We note that even though the latter two instruments are quite promising in their ability to track quickly moving particles, they are significantly more complicated than standard, off-the-shelf instruments. A more optically straightforward approach has been developed that uses multi focal-plane imaging in a wide-field setting combined with active laser positioning for tracking of a single particle (Juette and Bewersdorf, 2010). Since it is based on a widefield modality, however, it still requires online position estimation and is subject to issues of motion blur and similar challenges common to this setup.

The aforementioned active tracking methods all offer various degrees of temporal performance that outperform that allowed by the passive tracking paradigm. However, most of the techniques require specialized and potentially expensive hardware and tend to be overly complicated to implement. Consequently, these methods have yet to reach widespread use despite how informative they may be.

With these two distinctions, namely the difference between passive and active tracking, we now turn our attention to how information is extracted from the data collected from particle tracking experiments.

1.3 Inference from Particle Tracking Experiments

After acquiring data from a particle tracking experiment, the analyst often seeks answers to two questions: (1) Where was the particle during the experiment? and (2) How did the particle behave according to some model? The common paradigm for answering these two questions is inherently serial in nature. In fact, most researchers first localize the position of the particle at each time-instant using a localization algorithm (which answers the first question) and then subsequently apply regression analysis to the localized positions to extract model parameters (which answers the second question).

Regarding the first question, in the context of widefield microscopy there are many methods that provide estimates of the particle position for each frame. One such method approximates the center of the particle by calculating the centroid of the particle's image, and another method uses a nonlinear fit to a Gaussian model. A quantitative comparison of these two methods, among others, is given in (Cheezum et al., 2001). A more recent method, which is capable of localizing the particle in three dimensions, is the radial symmetry center method (Parthasarathy, 2012); here, the center of the particle is determined by a numerical calculation of the gradient. Although the aforementioned methods are relatively simple, provide straightforward implementations, and yield intuitive estimates, more accurate and computationally expensive methods have been developed. Fourteen of these methods were demonstrated in a recent competition involving the tracking of particles in four biologically-inspired scenarios and the results are given in (Chenouard et al., 2014). Every method tested had clear advantages and disadvantages; as such, there was no clear winner.

Regarding the second question, when an estimate of the particle's position is known, various methods from statistics may be used to estimate model-based param-

eters that describe the motion behavior. The most commonly used method involves calculating the mean squared displacement (MSD) from the position estimates and then regressing to a known function. The MSD, which measures the correlation between points in time separated by time τ , is defined as

$$\text{MSD}(\tau) = \langle x(t + \tau) - x(t) \rangle^2 + \langle y(t + \tau) - y(t) \rangle^2 + \langle z(t + \tau) - z(t) \rangle^2, \quad (1.2)$$

where $\langle \cdot \rangle$ denotes a time average. For some physical processes relevant to biology, the MSD may be analytically representable; for example, the MSD for an n -dimensional isotropic diffusion with coefficient D is

$$\text{MSD}(\tau) = 2nD\tau. \quad (1.3)$$

Thus, to estimate the diffusion coefficient, one need only fit a line to the estimated MSD and estimate the slope. Several other models relevant to biology have analytical MSDs; a review of these is given in (Saxton and Jacobson, 1997).

Despite its popularity, it has been shown that naively fitting a curve to the MSD may lead to erroneous estimates. For example, it is rarely the case that the position of the particle is perfectly known without error; in fact, the noise in the position estimate has been shown in (Martin et al., 2002) to create a constant bias in the MSD dependent on the variance of the error in estimation. This bias, however, is never known in practice and must be used as a fit parameter which consequently reduces the localization precision. Additionally, the optimal number of data points to be used in the regression must be determined. In (Saxton, 1997), the effect of temporal correlation was described and how it creates discrepancies from the expected MSD; their recommendation is that the analyst limit the regression to the first one-quarter of points of the MSD. This recommendation, however, has no analytical justification and is merely rule-of-thumb.

Recognizing these problems, Michalet first attempted to determine the optimal number of points with which to fit the MSD. In (Michalet, 2010), he provides a method, the Optimal Least Squares Fit (OLSF), for numerically determining the number of points to fit the MSD for a simple diffusion model with unknown localization error. The method, albeit effective, is based on heuristics and is limited to the case of diffusive motion. Moreover, the method assumes that the localization error is additive, white Gaussian noise - an assumption that has not been justified.

At the same time as Michalet, Berglund developed a computationally efficient approach to estimating diffusion coefficients using a maximum likelihood (ML) estimator (Berglund, 2010); the two later reconciled their methods in (Michalet and Berglund, 2012). In particular, Berglund recognized that a diffusion with intraframe blur and additive white noise had a pair-wise correlated displacement process, and, with this, he developed a Whittle-type estimator which could be computationally realized with the Fast Fourier Transform. Moreover, he was able to provide analytical formulae for the Cramér-Rao bounds associated with the diffusion coefficient and measurement noise variance. The approach was later extended in (Shuang et al., 2012) to the case where the fluorescent particle “turned off” during the measurement period. Much like Michalet’s algorithm, Berglund’s algorithm was only applicable to the case of diffusive motion and with normally distributed localization error.

Despite the work that has been done in this area, the two aforementioned questions have not been sufficiently answered. One potential problem with the common paradigm is due to the fact that the particle is localized without regard to the entire data set; intuitively, it seems that taking all the measurements into account would produce a better estimate of position, especially in light of a given motion or observation model. In addition, the act of localizing the particle only produces a point estimate of the location at a given time. Instead, more information could be inferred if an entire

probability density function of the particle’s location were available for each time-instant. Parameter estimation via regression to the MSD, despite being applicable to many types of particle motion, is still limited to normally distributed localization uncertainty which is an assumption that has not been justified. Berglund’s approach, via maximum likelihood estimation, appears promising, but it is only limited to diffusive motion with normally distributed localization error. Thus, there exists a need for a method that can produce probability densities of the particle’s location given all the *raw* measurements in addition to providing estimates of the parameters that describe the particle’s motion for any motion or observation model.

1.4 Contributions and Organization of Thesis

We present two main contributions within this thesis. The first contribution pertains to the issue of actively tracking a fluorescent particle in three dimensions, and the second contribution pertains to the issue of inferring localization information and parameter estimates from particle tracking data.

The tracking method proposed in this thesis improves upon previously developed methods for several reasons. In particular, the method is unique in the fact that, despite belonging to the class of active tracking methods, it requires no online localization and can therefore be implemented at high update rates. Moreover, the generated trajectories are smooth and do not require discontinuous jumps to various points in space. In addition, the method operates without any knowledge of the particle’s motion and does not require knowledge of the microscope’s PSF apart from the existence of an isolated maximum which is coincident with the location of the particle. Furthermore, it requires no specialized hardware and can be implemented, with varying degrees of performance, on a variety of confocal microscopes. Perhaps most importantly, the method allows for substantial theoretical analysis regarding its abil-

ity to track fluorescent particles. In this thesis, we mathematically describe several important properties and characteristics of the method which include the existence of an equilibrium trajectory, the stability of the equilibrium trajectory, a performance metric that describes its ability to track a diffusing particle, and guidelines for parameter selection.

Secondly, we present a numerical method, based on prior techniques developed in the field nonlinear system identification, which is capable of simultaneous localization and parameter estimation from particle tracking data. The method produces two results: (1) a probability density function of the particle's location as a function of time and given the measurements, and (2) maximum likelihood estimates of the model parameters. In addition, the method allows for nonlinear motion and observation models and only requires that the motion be Markovian and that measurements at a given time only depend on the particle's location at that particular time-instant. This thesis applies the method to several simulated scenarios in a widefield imaging context. In particular, we consider several different modes of motion, including free, confined, and tethered diffusions, and use the proposed inference method to simultaneously localize the particle and estimate model parameters. We show that the method reliably estimates the model parameters and that it is capable of super-resolution position localization.

This thesis is organized in the following manner. In Chapter 2, a brief overview of confocal microscopy is given, and, following this, the tracking algorithm is presented and is analyzed in two separate scenarios. In particular, we first consider the case where the particle is immobile and the PSF is radial and of unbounded support. For this scenario, we prove the existence of a sinusoidal equilibrium trajectory centered about the extremum, we prove its stability using averaging theory, and we numerically characterize its stability using Floquet theory. We then consider a second

scenario which assumes the particle is moving according to a Brownian motion and that the PSF exhibits bounded support. In this case, we derive a metric for tracking performance which is based on an approximation of the expected first passage time. This approximation is then numerically characterized and used to provide information regarding optimal parameter selection.

Chapter 3 describes the inference algorithm in the context of tracking fluorescent particles. The algorithm is then demonstrated through its application to several different simulated scenarios within a widefield fluorescence microscope, including a particle undergoing free, confined, and tethered diffusions.

Lastly, Chapter 4 demonstrates an experimental application of both the methods presented in Chapters 2 and 3. Specifically, we implement the real-time tracking algorithm in a confocal microscope and use it to track a quantum dot in a hydrogel. We then use the presented inference method to both localize the particle and estimate its diffusion coefficient and speed.

Chapter 2

Tracking a Fluorescent Source via Extremum Seeking

In this chapter, a feedback algorithm is described which is capable of tracking a fluorescent particle in a confocal microscope. We begin by briefly introducing the function of a confocal microscope and how it uses point-measurements of intensity to form a three-dimensional image; a full treatment of confocal microscopy is, however, beyond the scope of this work and the reader is referred to (Pawley, 2006) for further information. Next, the feedback algorithm is presented and then characterized. In particular, two different scenarios are considered. The first scenario considers the case of a stationary particle with a point spread function exhibiting unbounded support. Here, we prove the existence of an equilibrium trajectory, prove its stability, and numerically characterize its stability using Floquet theory. The second scenario considers the case of a diffusing particle with a point spread function exhibiting bounded support. In this case, we establish a performance metric based off an approximation to the expected first passage time. We then numerically characterize the performance metric and then use those results to offer guidance on optimal parameter selection. For more information on how the algorithm is implemented on a real confocal microscope, see Chapter 4. The work presented in this chapter is based on (Ashley and Andersson, 2016) where it was described in the context of the autonomous extremum-seeking of three-dimensional scalar potential fields.

2.1 Overview of Confocal Microscopy

The confocal microscope is an extension of the widefield epifluorescent microscope illustrated in Fig. 1-1 that attempts to solve two issues inherent to widefield measurements. First, the confocal microscope modestly improves the lateral resolution of the microscope in the plane of focus. More importantly, the confocal microscope allows for three-dimensional imaging due to the addition of confocal pinholes which block out of focus light; thus, the confocal microscope possesses a finite axial resolution unlike the widefield epifluorescent microscope.

A typical beam path for an epifluorescent confocal microscope is shown in Fig. 2-1. In this configuration, an excitation light source, which is often a laser, is passed through a pinhole and is reflected off a dichroic mirror. The light is then passed through the objective lens where it is focused onto the sample. The fluorescent light emitted by the sample (which is of a different wavelength relative to the excitation light) is collected by the objective, passed through the dichroic, and focused onto a single-pixel device, such as an avalanche photodiode (APD). Note that out-of-focus light emitted by the sample is also collected by the objective but is subsequently blocked by the pinhole which is confocal to the excitation pinhole. This, in fact, is the primary reason why confocal microscopes have a finite axial resolution.

The process by which an image is acquired for confocal microscopes differs greatly from that of widefield. Recall that widefield microscopes typically acquire pixelated images of a large portion of the sample; in the confocal microscope, only a single pixel is used. Thus, the confocal microscope must move the sample relative to the fixed focal volume (or, in a laser-scanning confocal microscope, move the focal volume relative to the fixed sample) and acquire point measurements of the intensity of the emitted light. Consequently, acquiring full images of a specimen takes much longer for confocal microscopes since it becomes akin to raster-based instruments like the AFM.

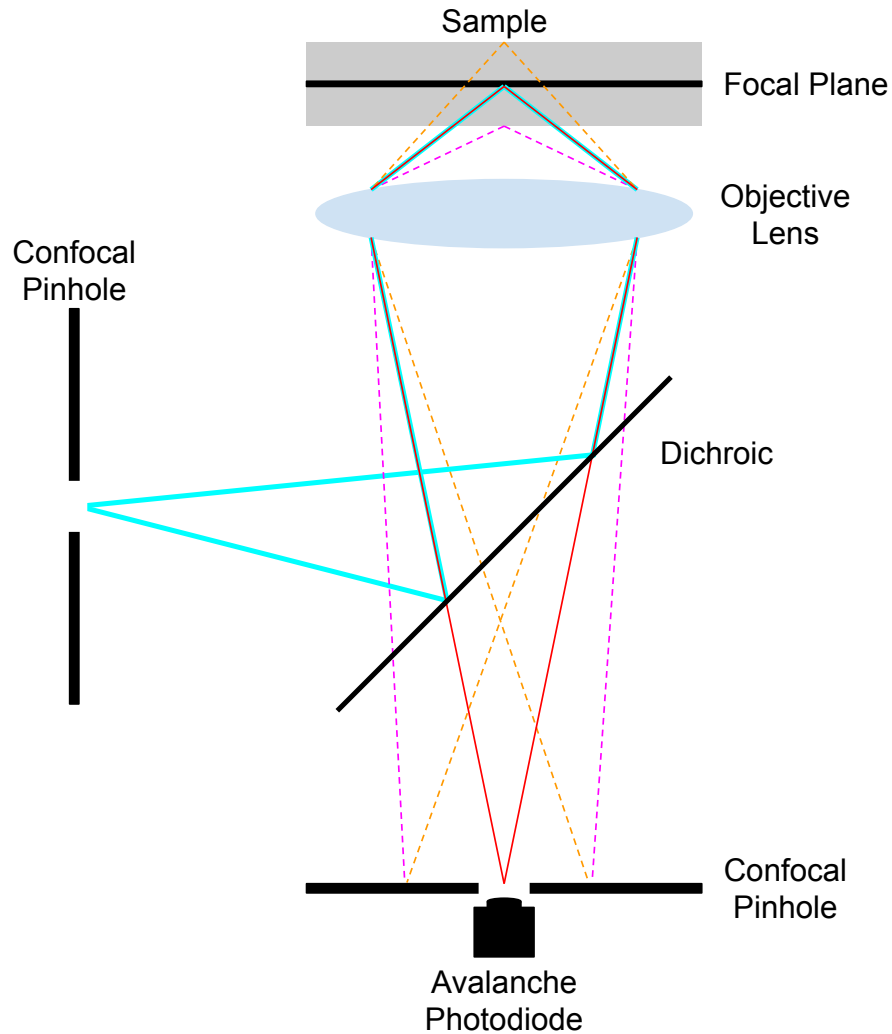


Figure 2·1: A ray diagram of a confocal microscope. Here, an excitation source (shown in blue) is passed through a pinhole and reflected to the objective lens by a dichroic. The objective lens focuses the excitation light onto the focal plane of the sample (shown as a black line contained within a gray rectangle). The light emitted by the fluorophore (shown in red) is collected by the objective lens and passed through the dichroic. The emitted light is then passed through another pinhole which is confocal to the excitation pinhole. The intensity of the light is then measured by an avalanche photodiode. Note that the out of focus light (shown by the dashed magenta and orange rays) are not confocal with either pinhole and are subsequently blocked.

However, the improved spatial resolution and the capability of three-dimensional optical sectioning often makes the sacrifice in temporal resolution worth it.

A very important feature of the confocal microscope, which we shall later exploit in the tracking of a fluorescent particle, is the shape of its PSF. A theoretical model of the confocal PSF sans aberration is illustrated in Fig. 2-2. Here, we observe two main characteristics of the PSF: (1) it has a shape similar to that of a three-dimensional Gaussian function, and (2) it has a maximum at the point-source. Regarding the first point, it has been shown that, for a certain non-paraxial optical model based off a Debye integral, a Gaussian approximation is “nearly perfect” for the confocal microscope (Zhang et al., 2007). In regard to the second point, the maximum at the center of the particle is global, isolated, and coincident with the particle.

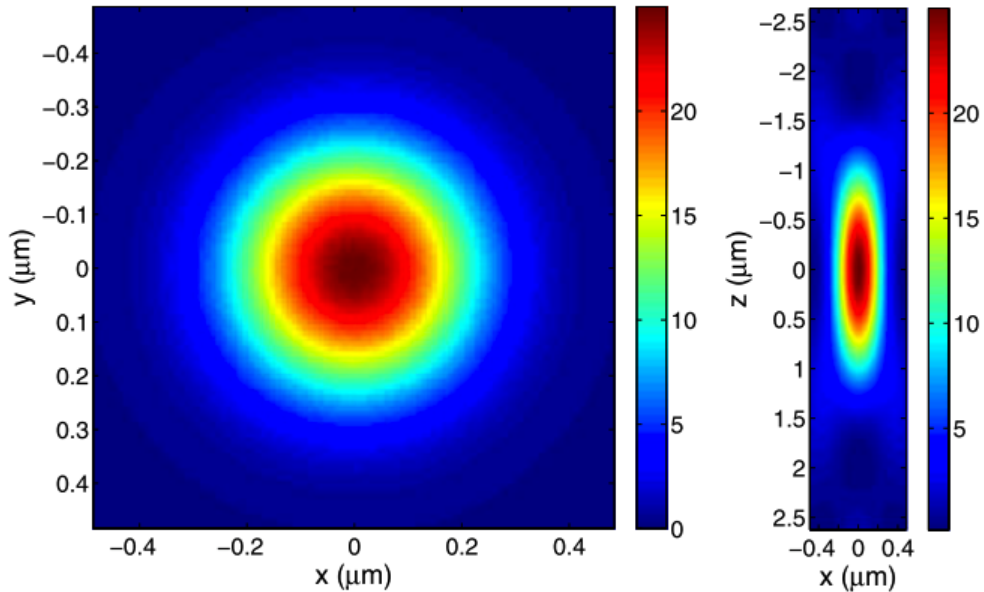


Figure 2-2: A theoretical model of the confocal point spread function (PSF) shown in two different planes. The picture on the left shows a cross-section of the PSF within the focal plane, and the picture on the right shows a cross-section along the axial plane. Note the differences in axis lengths. Image reproduced from (Andersson, 2011).

Given the nature of image acquisition (which is formed by measuring the emitted

intensity at single points in space) as well as the features of the PSF (which includes the existence of a maximum coincident with the particle), one potential method for tracking a fluorescent particle within a confocal microscope is by using the intensity measurements as feedback to move the focal volume's position so that it follows the extremum of the PSF (and thereby follows the particle). This is the principle of operation behind the tracking algorithm described in this chapter.

2.2 Problem Statement

The basis of the tracking algorithm presented here is built upon the two-dimensional extremum-seeking control law proposed in (Baronov and Baillieul, 2011) which considers a single sensor moving within a plane. It was assumed that the sensor follows the nonholonomic dynamics given by

$$\dot{x} = v \cos(\theta), \quad x(0) = x_0, \quad (2.1a)$$

$$\dot{y} = v \sin(\theta), \quad y(0) = y_0, \quad (2.1b)$$

where $v > 0$ is a constant speed and $\theta = \theta(t)$ is the time-varying heading angle; in the context of confocal microscopy, the position of the sensor is synonymous with the position of the focal volume. The sensor takes collocated, noiseless measurements of an unknown scalar field $F : \mathbb{R}^2 \rightarrow \mathbb{R}$, which is synonymous with the confocal PSF. Under the assumption that the field is a Morse function with a single maximum, it was shown that by choosing

$$\theta(t) = \theta_0 + \omega_1 (t - K_p F), \quad \theta(0) = \theta_0, \quad (2.2)$$

the sensor would move to a finite trapping region containing the maximum of the field in finite time for certain values of parameters ω_1 and K_p . Moreover, if in addition the field F were radial (that is, if F only depended on the Euclidean norm of the

sensor relative to the maximum), then (2.2) would drive the sensor to a periodic orbit centered about the maximum. (Changing the sign of K_p would yield equivalent results for F having instead a single minimum.) As compared to the scheme proposed in (Cochran and Krstic, 2009), the controller in (2.2) has fewer controller parameters to adjust, possesses a much simpler attractor, and does not require averaging methods to prove its stability. Unfortunately, this algorithm is only applicable to the two-dimensional case.

An extension to the control law (2.1) and (2.2) into three dimensions was originally described in (Andersson, 2011). To extrapolate the two-dimensional trajectory into three dimensions, a slow, time-varying $SO(3)$ rotation was applied to the velocities (2.1) to yield the sensor dynamics

$$\dot{x} = v \cos(\theta), \quad x(0) = x_0, \quad (2.3a)$$

$$\dot{y} = v \sin(\theta) \cos(\phi), \quad y(0) = y_0, \quad (2.3b)$$

$$\dot{z} = -v \sin(\theta) \sin(\phi), \quad z(0) = z_0, \quad (2.3c)$$

where $v > 0$ is a constant speed, θ is still defined by (2.2), and $\phi = \phi(t)$ is the rotation angle about the x axis. This rotation is governed by

$$\phi(t) = \phi_0 + \omega_2 t, \quad \phi(0) = \phi_0, \quad (2.4)$$

with $\omega_2 \neq 0$ controlling the rate of the axial rotation. This control law was successfully demonstrated in the context of tracking a fluorescent particle in a confocal microscope via simulation in (Andersson, 2011) and later experimentally in (Ashley et al., 2012).

A rigorous analysis of (2.3) is, unfortunately, quite challenging due to the fact that no analytical formulae exist that describe its steady state solution, even for the simplest PSFs. One approach for analysis that appears intuitive is to let ω_2 be a small perturbation on the two-dimensional dynamics (2.1); thus, a singular perturbation

approach could be used to infer the known stability properties of the two-dimensional system (provided in (Baronov and Baillieul, 2011)) into the three-dimensional one. The reduced system, however, cannot be shown to be exponentially stable and, as a result, stability cannot be inferred using variants of Tikhonov's theorem (Verhulst, 2005).

With this difficulty in mind, a contribution provided by this thesis is a modification to (2.3) that allows for tractable analysis. Consider a confocal microscope which is able to move the position of its focal volume $\mathbf{x}_s \triangleq [x_s, y_s, z_s]^T \in \mathbb{R}^3$ relative to some stationary frame and that takes collocated, noiseless intensity measurements $F : \mathbb{R}^3 \rightarrow \mathbb{R}$ of the fluorescence generated by a single point-source. The modification to (2.3) proposed in this thesis is

$$\dot{x}_s = v \cos(\theta), \quad x_s(0) = x_{s,0}, \quad (2.5a)$$

$$\dot{y}_s = v \sin(\theta) \cos(\phi) + v \left(\frac{\omega_2}{\omega_1} \right) \cos(\theta) \sin(\phi), \quad y_s(0) = y_{s,0}, \quad (2.5b)$$

$$\dot{z}_s = -v \sin(\theta) \sin(\phi) + v \left(\frac{\omega_2}{\omega_1} \right) \cos(\theta) \cos(\phi), \quad z_s(0) = z_{s,0}, \quad (2.5c)$$

where $v > 0$ is the constant speed of the focal volume, and ω_1 and ω_2 are angular velocities describing the time-varying rotations $\theta(t)$ and $\phi(t)$. These angles evolve according to (2.2) and (2.4). Note that the only difference between the original dynamics (2.3) and the modified dynamics (2.5) is the addition of two perturbation terms in the y and z velocities.

2.3 A Stationary Particle with Unbounded Support of PSF

For the results that follow in this section, we consider only the case where the PSF has a single maximum located at $\mathbf{x}^* \in \mathbb{R}^3$. In addition, we assume the PSF is radial about the maximum such that $F(\mathbf{x}^* - \mathbf{x}_s) = f(\|\mathbf{x}^* - \mathbf{x}_s\|)$.

2.3.1 Existence of Equilibrium Trajectory

Before discussing the stability of the algorithm, we first derive the equilibrium trajectory. In the following proposition, we prove the existence of a sinusoidal equilibrium trajectory which is centered about the maximum of the PSF.

Proposition 1. *Consider the focal volume position (2.5) with angle dynamics defined by (2.2) and (2.4). Assume that the confocal microscope takes noiseless measurements of the point spread function $F(\tilde{\mathbf{x}}(t)) = f(\|\tilde{\mathbf{x}}\|)$ which is radial about the isolated maximum \mathbf{x}^* . Then, an equilibrium trajectory $\bar{\mathbf{x}}(t)$ for the focal volume displacement relative to the maximum $\tilde{\mathbf{x}}(t) \triangleq \mathbf{x}^* - \mathbf{x}_s$ is*

$$\bar{x}(t) = -\bar{R} \sin(\omega_1 t + \bar{\alpha}), \quad (2.6a)$$

$$\bar{y}(t) = \bar{R} \cos(\omega_1 t + \bar{\alpha}) \cos(\omega_2 t + \bar{\beta}), \quad (2.6b)$$

$$\bar{z}(t) = -\bar{R} \cos(\omega_1 t + \bar{\alpha}) \sin(\omega_2 t + \bar{\beta}), \quad (2.6c)$$

where

$$\bar{R} \triangleq \frac{v}{\omega_1} \quad (2.7)$$

is the steady state radius,

$$\bar{\alpha} \triangleq \theta_0 - \omega_1 K_p f(\bar{R}) \quad (2.8)$$

is the primary phase offset, and

$$\bar{\beta} \triangleq \phi_0 \quad (2.9)$$

is the secondary phase offset.

Proof. Define the difference between the focal volume displacement and the candidate equilibrium trajectory as $\mathbf{e}(t) \triangleq \tilde{\mathbf{x}}(t) - \bar{\mathbf{x}}(t)$. The error coordinate thus has a candidate equilibrium at the origin. Differentiating $\mathbf{e}(t)$ with respect to time yields

$$\dot{e}_x = v (\cos(\omega_1 t + \bar{\alpha}) - \cos(\omega_1 t + \Theta(\mathbf{e} + \bar{\mathbf{x}}))), \quad (2.10a)$$

$$\begin{aligned} \dot{e}_y &= v \left(\sin(\omega_1 t + \bar{\alpha}) \cos(\omega_2 t + \bar{\beta}) - \sin(\omega_1 t + \Theta(\mathbf{e} + \bar{\mathbf{x}})) \cos(\omega_2 t + \bar{\beta}) \right) \\ &\quad + v \left(\frac{\omega_2}{\omega_1} \right) \left(\cos(\omega_1 t + \bar{\alpha}) \sin(\omega_2 t + \bar{\beta}) - \cos(\omega_1 t + \Theta(\mathbf{e} + \bar{\mathbf{x}})) \sin(\omega_2 t + \bar{\beta}) \right), \end{aligned} \quad (2.10b)$$

$$\begin{aligned} \dot{e}_z &= -v \left(\sin(\omega_1 t + \bar{\alpha}) \sin(\omega_2 t + \bar{\beta}) - \sin(\omega_1 t + \Theta(\mathbf{e} + \bar{\mathbf{x}})) \sin(\omega_2 t + \bar{\beta}) \right) \\ &\quad + v \left(\frac{\omega_2}{\omega_1} \right) \left(\cos(\omega_1 t + \bar{\alpha}) \cos(\omega_2 t + \bar{\beta}) - \cos(\omega_1 t + \Theta(\mathbf{e} + \bar{\mathbf{x}})) \cos(\omega_2 t + \bar{\beta}) \right), \end{aligned} \quad (2.10c)$$

with

$$\Theta(\mathbf{x}) \triangleq \theta_0 - \omega_1 K_p F(\mathbf{x}). \quad (2.11)$$

Evaluating (2.10) at the origin and noting that

$$\begin{aligned} \Theta(\bar{\mathbf{x}}) &= \theta_0 - \omega_1 K_p F(\bar{\mathbf{x}}), \\ &= \theta_0 - \omega_1 K_p f(\bar{R}), \\ &= \bar{\alpha}, \end{aligned}$$

allows us to verify that the origin is an equilibrium point. It follows that (2.6) is an equilibrium trajectory for \tilde{x} . \square

Proposition 1 indicates that the equilibrium trajectory (2.6) is sinusoidal with frequencies ω_1 , $\omega_1 + \omega_2$, and $\omega_1 - \omega_2$. Specifically, the x coordinate exhibits the frequency ω_1 and the y and z coordinates exhibit the frequencies $\omega_1 + \omega_2$ and $\omega_1 - \omega_2$. Moreover, the amplitudes and phase shifts are governed by both the controller parameters and the shape of the point spread function. Thus, the equilibrium trajectory provides the user some guidance for controller parameter selection. For example, the user could set the frequencies ω_1 and ω_2 in accordance with the microscope's actuator bandwidths such that $\omega_1 + \omega_2 < \omega_{\max}$. Additionally, a value for v may be selected to set the steady-state radius \bar{R} which determines the distance between the focal volume orbit and the point-source. Note, however, that K_p does not appear in the equilibrium trajectory; as will be made apparent in the following proposition, this parameter only

affects the stability of the algorithm.

2.3.2 Stability of Equilibrium Trajectory

We next consider the stability of the equilibrium trajectory developed in the previous section. First, we propose a lemma which will be used in a later proposition which shows the equilibrium trajectory is locally exponentially stable given certain conditions. Recall that the system defined by the error coordinates (2.10) has an equilibrium point at the origin. Linearizing this system about the origin yields the linear time-varying system

$$\delta\dot{\mathbf{e}}(t) = \epsilon A(t)\delta\mathbf{e}(t), \quad (2.12)$$

with the components of $A(t)$ defined by

$$\begin{aligned} A_{11} &\triangleq -\omega_1^2 \sin^2(\omega_1 t + \bar{\alpha}), \\ A_{12} &\triangleq \left(\frac{\omega_1^2}{2}\right) \sin(2\omega_1 t + 2\bar{\alpha}) \cos(\omega_2 t + \bar{\beta}), \\ A_{13} &\triangleq -\left(\frac{\omega_1^2}{2}\right) \sin(2\omega_1 t + 2\bar{\alpha}) \sin(\omega_2 t + \bar{\beta}), \\ A_{21} &\triangleq \left(\frac{\omega_1^2}{2}\right) \sin(2\omega_1 t + 2\bar{\alpha}) \cos(\omega_2 t + \bar{\beta}) - \omega_1 \omega_2 \sin^2(\omega_1 t + \bar{\alpha}) \sin(\omega_2 t + \bar{\beta}), \\ A_{22} &\triangleq -\omega_1^2 \cos^2(\omega_1 t + \bar{\alpha}) \cos^2(\omega_2 t + \bar{\beta}) + \left(\frac{\omega_1 \omega_2}{4}\right) \sin(2\omega_1 t + 2\bar{\alpha}) \sin(2\omega_2 t + 2\bar{\beta}), \\ A_{23} &\triangleq \left(\frac{\omega_1^2}{2}\right) \cos^2(\omega_1 t + \bar{\alpha}) \sin(2\omega_2 t + 2\bar{\beta}) - \left(\frac{\omega_1 \omega_2}{2}\right) \sin(2\omega_1 t + 2\bar{\alpha}) \sin^2(\omega_2 t + \bar{\beta}), \\ A_{31} &\triangleq -\left(\frac{\omega_1^2}{2}\right) \sin(2\omega_1 t + 2\bar{\alpha}) \sin(\omega_2 t + \bar{\beta}) - \omega_1 \omega_2 \sin^2(\omega_1 t + \bar{\alpha}) \cos(\omega_2 t + \bar{\beta}), \\ A_{32} &\triangleq \left(\frac{\omega_1^2}{2}\right) \cos^2(\omega_1 t + \bar{\alpha}) \sin(2\omega_2 t + 2\bar{\beta}) + \left(\frac{\omega_1 \omega_2}{2}\right) \sin(2\omega_1 t + 2\bar{\alpha}) \cos^2(\omega_2 t + \bar{\beta}), \\ A_{33} &\triangleq -\omega_1^2 \cos^2(\omega_1 t + \bar{\alpha}) \sin^2(\omega_2 t + \bar{\beta}) - \left(\frac{\omega_1 \omega_2}{4}\right) \sin(2\omega_1 t + 2\bar{\alpha}) \sin(2\omega_2 t + 2\bar{\beta}), \end{aligned}$$

and

$$\epsilon \triangleq -K_p \bar{R} \left(\frac{\partial f}{\partial \|\mathbf{x}\|} \Big|_{\|\mathbf{x}\|=\bar{R}} \right). \quad (2.14)$$

Here, A_{ij} denotes the i th column and the j th row of matrix $A(t)$. Under proper choice of the frequencies ω_1 and ω_2 , the time-varying matrix $A(t)$ is periodic. With this, we have the following lemma.

Lemma 1. *Consider the linear time-varying system given by (2.12). Assume that K_p , \bar{R} , ω_1 , and ω_2 are chosen strictly positive. Additionally, assume that ω_1 and ω_2 are commensurate with a common period T and that the point spread function $f(\|\mathbf{x}\|)$ is radial with a single maximum. Then, there exists a positive constant ϵ^* such that for all $0 < \epsilon < \epsilon^*$, the origin is an exponentially stable equilibrium point for (2.12).*

Proof. Since (2.12) is a linear time-varying system, it is not sufficient to show that the eigenvalues of $A(t)$ are contained within the left half plane. Instead, consider the time-averaged system defined by

$$\dot{\mathbf{e}}_{\text{avg}} = \epsilon A_{\text{avg}} \mathbf{e}_{\text{avg}} \quad (2.15)$$

with

$$A_{\text{avg}} \triangleq \frac{1}{T} \int_0^T A(\sigma) d\sigma. \quad (2.16)$$

Evaluation of (2.16) over the commensurate period T yields

$$A_{\text{avg}}^= = \begin{bmatrix} -\omega_1^2/2 & 0 & 0 \\ 0 & -\omega_1^2(1+2\delta)/8 & 0 \\ 0 & 0 & -\omega_1^2(3-2\delta)/8 \end{bmatrix} \quad (2.17)$$

for $\omega_1 = \omega_2$ with $\delta \triangleq \cos^2(2(\bar{\alpha} - \bar{\beta}))$, and

$$A_{\text{avg}}^{\neq} = \begin{bmatrix} -\omega_1^2/2 & 0 & 0 \\ 0 & -\omega_1^2/4 & 0 \\ 0 & 0 & -\omega_1^2/4 \end{bmatrix} \quad (2.18)$$

for $\omega_1 \neq \omega_2$ but commensurate. Note that $\epsilon > 0$ since $\frac{\partial f}{\partial \|\mathbf{x}\|} < 0$ for all $\|\mathbf{x}\| \neq 0$ due to

the existence of a single maximum. With this and the fact that both $A_{\text{avg}}^=$ and A_{avg}^{\neq} are Hurwitz, it follows that the origin is an exponentially stable equilibrium point for the averaged system (2.15). From Theorem 10.4 in (Khalil, 2002) it follows that there exists a positive constant ϵ^* such that for all $0 < \epsilon < \epsilon^*$, the origin is an exponentially stable equilibrium point for the original (linearized) system (2.12). \square

Lemma 1 establishes that the linearized system (2.12) has an exponentially stable equilibrium point at the origin for some non-zero choice of ϵ defined by (2.14). Given this lemma, we may now infer stability for the full nonlinear system (2.10).

Proposition 2. *Assume that K_p , \bar{R} , ω_1 , and ω_2 are chosen strictly positive. Additionally, assume that ω_1 and ω_2 are commensurate with a common period T and that the point spread function $f(\|\mathbf{x}\|)$ is radial with a single maximum. Then, (2.6) is an exponentially stable equilibrium trajectory for the deviation coordinates $\tilde{\mathbf{x}}$.*

Proof. In the nonlinear system $\dot{\mathbf{e}} = f(t, \mathbf{e})$ defined by (2.10), the function f is continuously differentiable, and its Jacobian $A(t)$ evaluated at the origin defined by (2.12) is bounded and Lipschitz uniformly in t . By Lemma 1, there exists an ϵ^* such that for all $0 < \epsilon < \epsilon^*$ the origin is an exponentially stable equilibrium point for (2.12), and it follows from Theorem 4.13 in (Khalil, 2002) that the origin is an exponentially stable equilibrium point for (2.10). Since the origin is an exponentially stable equilibrium point for (2.10), the equilibrium trajectory (2.6) defined in Proposition 1 is also exponentially stable for the deviation coordinates $\tilde{\mathbf{x}}$. \square

Proposition 2 establishes the existence of a non-zero choice of ϵ such that the equilibrium trajectory defined in Proposition 1 is locally exponentially stable. Recall from (2.14) that ϵ is directly proportional to K_p , \bar{R} , and the slope of the PSF evaluated at \bar{R} ; Proposition 2 therefore implies there are values for these parameters guaranteeing exponential stability. The majority of these parameters can be controlled by the user. As mentioned before, v in conjunction with ω_1 may be chosen to guarantee a regulated steady state distance from the maximum; if v (and therefore \bar{R}) is chosen to be particularly large, K_p may be reduced to compensate for a potential lack of stability. Moreover, if a particular value for ϵ is known to result in stability and if an

upper bound of the point spread function's slope is known, values for K_p and \bar{R} may be chosen relative to this upper bound that guarantee stability. We also note that the evaluation of the slope of the PSF can be controlled by adjusting the intensity of the microscope's excitation source. Note that the secondary frequency ω_2 *does not* appear in ϵ ; although this may appear to imply that it does not influence stability, it will be shown in the following section that choosing ω_2 too large relative to ω_1 may result in instability.

Fig. 2.3 presents a trajectory for the proposed feedback controller. The controller parameters for this simulation were $\omega_1 = 100$ Hz, $\omega_2 = 10$ Hz, $K_p = 0.005$, and $\bar{R} = v/\omega_1 = 0.1$; the PSF was parabolic $f(\|\mathbf{x}\|) = 10(1 - \|\mathbf{x}\|^2)$ with the extremum located at the origin. We note that the trajectory $\tilde{\mathbf{x}}(t)$ asymptotically approaches the equilibrium trajectory $\bar{\mathbf{x}}(t)$ as t increases. The error $\mathbf{e}(t)$ (as well as the linearized $\delta\mathbf{e}(t)$ and averaged linearized errors) is also shown, and it appears to approach zero asymptotically as t increases. In addition, the convergence to the equilibrium trajectory in the x axis was much faster than that of y and z ; this is to be expected due to the definition of A_{avg} in the proof of Lemma 1 where it is shown that the magnitude of the x eigenvalue is twice that of both y and z .

2.3.3 Numerical Characterization of Equilibrium Trajectory

Although Proposition 2 indicates exponential stability for some non-zero values of ϵ , it does not provide any information on the values for which the result holds. Understanding the stability as a function of ϵ is of significant practical importance as the candidate values for ϵ may be too small to be of any use to the user. Thus, in the following section, we study the stability of (2.12) as a function of ϵ by using results provided by Floquet theory.

Consider the linear, time-varying system defined by (2.12) with associated transition matrix $\Phi(t, t_0)$ describing the transfer of the state $\delta\mathbf{e}$ from time t_0 to time t . We

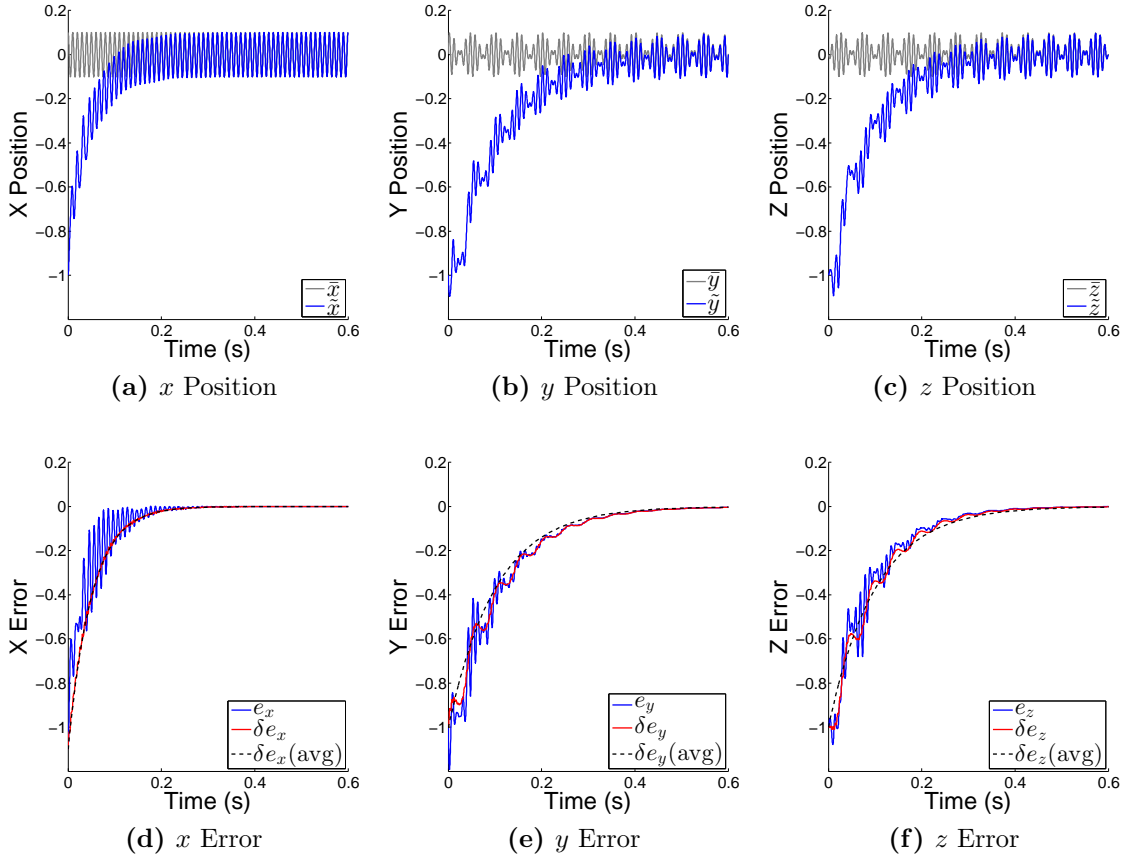


Figure 2-3: A typical trajectory for the proposed tracking controller. In the figures shown in the top row, the deviation (\tilde{x} , \tilde{y} , \tilde{z}) of the focal volume from the particle is shown in blue whereas the equilibrium trajectory (\bar{x} , \bar{y} , \bar{z}) is shown in gray. Here, the deviation asymptotically approaches the equilibrium trajectory in all three axes. In the figures in the bottom row, the error between the deviation and the equilibrium trajectory is shown in blue; we also plot the resulting linearized error (shown in red) as well as the averaged linearized error (shown in dashed black). In all three axes, the errors asymptotically approach zero. Here, the controller parameters were $\omega_1 = 100$ Hz, $\omega_2 = 10$ Hz, $K_p = 0.005$, and $\bar{R} = v/\omega_1 = 0.1$. The PSF was assumed parabolic with the maximum located at the origin.

once again assume ω_1 and ω_2 are chosen to have a commensurate period T so that $A(t)$ is also periodic with the same period. Define the corresponding monodromy

matrix as

$$\Phi(T, 0) \triangleq e^{RT}, \quad (2.19)$$

which yields a particular value for $R \in \mathbb{C}^{3 \times 3}$. It follows by the Floquet-Lyapunov theorem (see, *e.g.*, Theorem 8.1 in (Brockett, 2015)) that the transition matrix for $A(t)$ may be written as

$$\Phi(t, t_0) = P^{-1}(t)e^{R(t-t_0)}P(t_0), \quad (2.20)$$

with $P^{-1}(t) \triangleq \Phi(t, 0)e^{-Rt}$; it can be shown that $P^{-1}(t)$ (and consequently $P(t)$) is periodic with period T . It follows that all solutions for (2.12) approach zero as t approaches infinity if the zeros of $\det(s\mathbb{I} - \Phi(t_0 + T, t_0))$ lie within the unit disk $|s| < 1$ (see Theorem 10.3 in (Brockett, 2015)). Since Φ is periodic, it is sufficient to show that exponential stability is implied if the eigenvalues of the monodromy matrix $\Phi(T, 0)$ are contained within the unit circle, and consequently by Proposition 2, that exponential stability is implied for the error coordinates (2.10).

To determine the stability of (2.12), one must first determine the monodromy matrix (2.19) as a function of ϵ and then assess whether its eigenvalues lie within the unit circle. Unfortunately, evaluation of the monodromy matrix in this case is not analytically tractable, so it must be calculated numerically. To evaluate the monodromy matrix, we use

$$\frac{d}{dt}\Phi(t, t_0) = \epsilon A(t)\Phi(t, t_0), \quad \Phi(t_0, t_0) = \mathbb{I}, \quad (2.21)$$

and solve for $\Phi(T, 0)$ by numerically integrating over the time interval $[0, T]$ as a function of the parameters ϵ , ω_1 , and ω_2 . Specifically, (ω_1, ω_2) was varied over the region $(0, 10] \times (0, 25]$ Hz discretized with a spacing of 0.1 Hz, and ϵ was varied over the interval $[0.1, 2.5]$. To reduce the size of the parameter space, we chose the

initial conditions θ_0 and ϕ_0 such that $\bar{\alpha}$ and $\bar{\beta}$ are zero; although this assumption limits the generality of the result, we note that the initial conditions do not appear to significantly affect the results that follow. Equation (2.21) was integrated using an explicit Runge-Kutta (4,5) method (Dormand and Prince, 1980) for the values described in the aforementioned parameter space, and the eigenvalues of $\Phi(T, 0)$ were numerically evaluated via the well-known QR algorithm.

Fig. 2.4 shows the resulting stability/instability regions for three particular values of ϵ , namely $\epsilon = (0.1, 0.25, 0.5)$, over the (ω_1, ω_2) space. Given these results, it appears that the region of instability (shown in red x's) is approximately triangular in shape and lies above the line $\omega_1 = \omega_2$. However, as ϵ increases, the region expands in size with ω_1 . Further increasing ϵ beyond 0.5 makes no significant difference and generates a result similar to $\epsilon = 0.5$; thus, it appears that there may be a limiting behavior to the shape of the instability region as ϵ increases. We also note that the general raggedness of the instability region is likely due to numerical errors resulting from both numerically evaluating $\Phi(T, 0)$ and its eigenvalues; this could be improved by using more reliable methods such as those proposed in (Lust, 2001).

Although the red regions are labeled as “unstable” in Fig. 2.4, this claim is specific to the particular linearized system (2.12) and is *not necessarily* true for the full nonlinear system (2.10). In general, instability of (2.10) cannot be inferred via the method of linearization unless its linearization had yielded a linear time-invariant system. Consequently, the red regions shown in Fig. 2.4 should be interpreted as “potentially unstable” regions in the context of the full nonlinear system despite being definitively unstable for the linearized system. It is to be noted, however, simulation studies indicate that the red regions are reliable predictors of instability in the full nonlinear system.

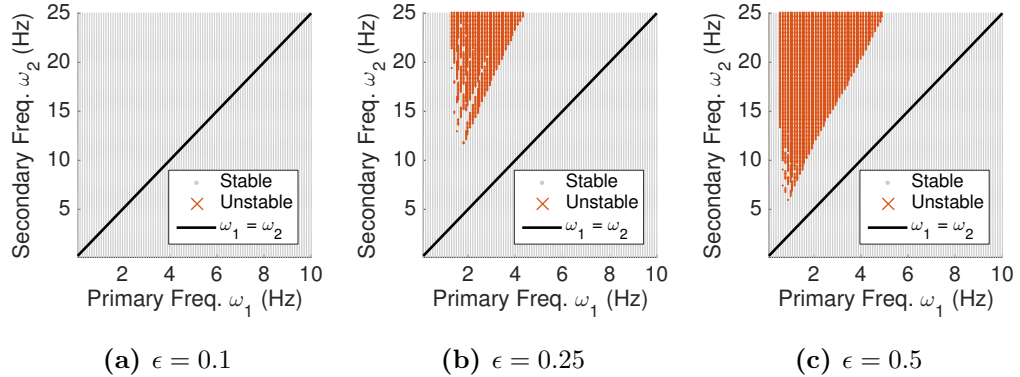


Figure 2-4: Stability regions of linear time-varying system (2.12) for three distinct values of ϵ defined in (2.14) as given by the numerical evaluation of the monodromy matrix (2.19). The grey dots indicate the region where the linear time-varying system is stable (*i.e.*, where the eigenvalues of the monodromy matrix are strictly within the unit circle), whereas the red x's mark the region of instability (*i.e.*, where the eigenvalues are on or outside the unit circle). Note that the size of the instability region increases as ϵ increases. Also note that the region of instability lies strictly above the solid black line $\omega_1 = \omega_2$.

2.4 A Diffusing Particle with Bounded Support of PSF

In the previous sections, we established that the position of the focal volume will converge to a sinusoidal trajectory centered about the location of the source. These results, however, depend on several rather strict assumptions. One limiting assumption is that the slope of the PSF is strictly negative at all locations other than the maximum; this is not true for realistic PSFs, especially when considering background noise. The second limiting assumption is that the location of the particle does not change in time. Thus, in the subsequent sections, we leverage the results from the previous sections to determine the expected first passage time for the cases where the PSF is bounded and the particle moves according to a Brownian motion.

For the results that follow, we assume the PSF is radial about the maximum location \mathbf{x}^* and that its value becomes constant beyond a distance of R^* from the

maximum. Mathematically, this is defined as

$$f_{R^*}(\|x\|) = \begin{cases} f(\|x\|) & \|x\| < R^* \\ f(R^*) & \text{otherwise.} \end{cases} \quad (2.22)$$

A one-dimensional depiction is shown in Fig. 2·5. The utility in this definition allows us to define regions where the focal volume has significantly deviated from the particle such that it is no longer trackable. Regions beyond R^* are deemed untrackable since no gradient information exists when the PSF is constant, and the focal volume will be unable to converge toward the particle.

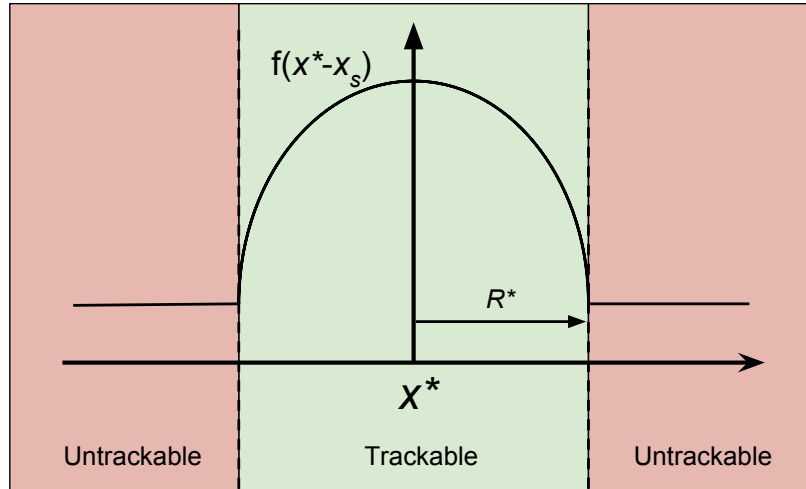


Figure 2·5: A one-dimensional illustration of a bounded field. The width of the field is R^* and is assumed to be radial about the maximum x^* . When the distance between the focal volume and the maximum exceeds R^* (red region), the PSF becomes constant and the particle becomes untrackable.

In addition to PSF boundedness, it is most often the case that the location of the particle is not time-invariant nor deterministic. Given that the behavior of the field is unknown to the tracking algorithm, one potentially useful motion model of the particle is that of a random walk with unknown isotropic diffusion coefficient D . In other words, the location of the particle is defined by the Itô stochastic differential

equation (SDE)

$$d\mathbf{x}^*(t) = \sqrt{2D} d\mathbf{W}(t), \quad (2.23)$$

where $\mathbf{W}(t)$ is a Wiener process on \mathbb{R}^3 . As the particle moves, so does the location of the maximum; as such, the focal volume, as it is driven toward the maximum of the PSF, will also follow the particle. On the other hand, if D becomes large, then the distance between the focal volume and the particle may become excessive. This is problematic because if the particle deviates too far away from the focal volume, then, due to the boundedness of the field (2.22), the focal volume may diverge from the particle.

2.4.1 Approximate Formula for First Passage Time

One useful metric of tracking performance is the time at which the focal volume first exceeds a certain distance from the particle. Recall that the error coordinates $\mathbf{e} \triangleq \mathbf{x}^* - \mathbf{x}_s - \bar{\mathbf{x}}$ denote the deviation of the particle (relative to the steady state trajectory) from the focal volume. Given this, the time when the norm of the error first exceeds the value $\rho \in \mathbb{R}^+$ is known as the first passage time and is defined for a particular sample path to be

$$\tau_\rho = \inf \{t : t \geq 0, \|\mathbf{e}(t)\| = \rho\}. \quad (2.24)$$

The value of ρ , which determines an upper limit on how large the tracking error may be, can be specified in numerous ways. One potential selection for ρ is the width of the PSF minus the effective tracking radius, *i.e.* $R^* - \bar{R}$ with \bar{R} defined in (2.7). This selection guarantees that the position of the focal volume is sufficiently close to the particle so that no acquired information pertaining to the PSF is lost. In contrast, if ρ were selected to be some value greater than $R^* - \bar{R}$, then the focal volume may be

allowed to spend much (if not all) of its time in the region where the field gradient is zero. Since it is unknown whether tracking can be maintained when the focal volume exits this bound, the best conservative value for ρ is $R^* - \bar{R}$. A two-dimensional illustration of this concept is shown in Fig. 2-6.

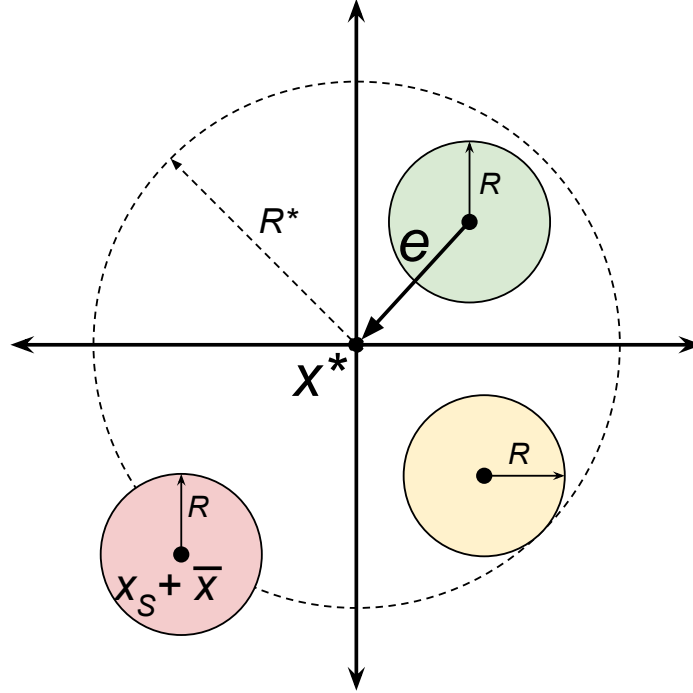


Figure 2-6: A two-dimensional illustration depicting the definition of tracking loss as defined by the stopping time (2.24). The coordinate axis is centered at the particle's location \mathbf{x}^* which exhibits a point spread function of radius R^* (shown as the dashed circle). There are three smaller circles depicting different focal volume locations relative to \mathbf{x}^* , and the center of each circle is $\mathbf{x}_s + \bar{\mathbf{x}}$ which is the position of the focal volume \mathbf{x}_s in addition to the steady state trajectory $\bar{\mathbf{x}}$. Since the steady state trajectory is periodic with amplitude $\bar{R} = v/\omega_1$, the effective radius of each circle is shown by the smaller solid circles of radius \bar{R} . The first circle, shown in green and residing in quadrant I, does not satisfy the stopping criterion $\|\mathbf{e}\| < R^* - \bar{R}$ and is therefore trackable. The second circle, shown in yellow and residing in quadrant IV, satisfies the stopping criterion and indicates the point at which tracking would first be lost. The third circle, shown in red and residing in quadrant III, details the scenario where the particle has significantly deviated from the focal volume and therefore cannot be reliably tracked.

To evaluate the expected first passage time (EFPT) for $\rho = R^* - \bar{R}$, we consider the time evolution of the error coordinates. The error coordinates, originally defined in the deterministic case as (2.10), may be rewritten as the solution of the Itô SDE

$$de_x = v (\cos(\omega_1 t + \bar{\alpha}) - \cos(\omega_1 t + \Theta(\mathbf{e} + \bar{\mathbf{x}}))) dt + \sqrt{2D} dW_x, \quad (2.25a)$$

$$\begin{aligned} de_y = & v (\sin(\omega_1 t + \bar{\alpha}) \cos(\omega_2 t + \bar{\beta}) - \sin(\omega_1 t + \Theta(\mathbf{e} + \bar{\mathbf{x}})) \cos(\omega_2 t + \bar{\beta})) dt \\ & + v \left(\frac{\omega_2}{\omega_1} \right) (\cos(\omega_1 t + \bar{\alpha}) \sin(\omega_2 t + \bar{\beta}) - \cos(\omega_1 t + \Theta(\mathbf{e} + \bar{\mathbf{x}})) \sin(\omega_2 t + \bar{\beta})) dt \\ & + \sqrt{2D} dW_y, \end{aligned} \quad (2.25b)$$

$$\begin{aligned} de_z = & -v (\sin(\omega_1 t + \bar{\alpha}) \sin(\omega_2 t + \bar{\beta}) - \sin(\omega_1 t + \Theta(\mathbf{e} + \bar{\mathbf{x}})) \sin(\omega_2 t + \bar{\beta})) dt \\ & + v \left(\frac{\omega_2}{\omega_1} \right) (\cos(\omega_1 t + \bar{\alpha}) \cos(\omega_2 t + \bar{\beta}) - \cos(\omega_1 t + \Theta(\mathbf{e} + \bar{\mathbf{x}})) \cos(\omega_2 t + \bar{\beta})) dt \\ & + \sqrt{2D} dW_z, \end{aligned} \quad (2.25c)$$

with $\bar{\alpha}$, $\bar{\beta}$, and $\Theta(\cdot)$ defined as before. As expected, determining an analytical expression for the EFPT for this particular system of nonlinear SDEs is nontrivial. An approximation to this system, however, may be made that allows for analytical results.

Recall that the stability of the full nonlinear system (2.10) was inferred from the much simpler linearized-then-averaged system. Following this notion and leveraging the fact that the diffusion coefficient is independent of the state, then by substituting the linearized-then-averaged dynamics (2.15) for the full stochastic error dynamics (2.25) we obtain the approximation

$$d\hat{e}_x = -\epsilon \left(\frac{\omega_1^2}{2} \right) \hat{e}_x dt + \sqrt{2D} dW_x, \quad (2.26a)$$

$$d\hat{e}_y = -\epsilon \left(\frac{\omega_1^2}{4} \right) \hat{e}_y dt + \sqrt{2D} dW_y, \quad (2.26b)$$

$$d\hat{e}_z = -\epsilon \left(\frac{\omega_1^2}{4} \right) \hat{e}_z dt + \sqrt{2D} dW_z, \quad (2.26c)$$

which is a system of independent Ornstein-Uhlenbeck (OU) processes (Uhlenbeck and Ornstein, 1930) with ϵ defined in (2.14). The OU process, commonly used in financial mathematics, not only possesses several convenient properties, such as mean reversion, but it also admits a closed-form solution for its EFPT. Note that (2.26) assumes $\omega_1 \neq \omega_2$; an equivalent system may be derived for the case of $\omega_1 = \omega_2$ by considering $A_{\text{avg}}^=$ in (2.17) instead of A_{avg}^\neq in (2.18).

The OU process admits an analytical formula for its EFPT out of the n -ball of known radius. It was shown in (Graczyk and Jakubowski, 2008) that, for an isotropic three-dimensional OU process $\mathbf{X}(t)$ governed by the Itô SDE

$$d\mathbf{X} = -\lambda \mathbf{X} dt + \sqrt{2D} d\mathbf{W} \quad (2.27)$$

with $\mathbf{X}(0) \stackrel{\text{a.s.}}{=} \mathbf{0}$, the EFPT time out of the three-dimensional-ball of radius ρ is

$$\mathbb{E}[\tau_\rho] = \left(\frac{\rho^2}{6D} \right) {}_2F_2 \left(1, 1; \frac{5}{2}, 2; \frac{\lambda \rho^2}{2D} \right) \quad (2.28)$$

where ${}_2F_2(\cdot; \cdot; \cdot)$ is the generalized hypergeometric function defined to be

$${}_2F_2(a_1, a_2; b_1, b_2; x) = \sum_{k=0}^{\infty} \frac{(a_1)_k (a_2)_k x^k}{(b_1)_k (b_2)_k k!}, \quad (2.29)$$

and with $(\cdot)_k$ denoting the k th Pochhammer symbol

$$(a)_k = \begin{cases} 1, & k = 0, \\ a(a+1)(a+2) \cdots (a+n-1), & k \geq 1. \end{cases} \quad (2.30)$$

Note that when the parameter λ becomes zero, the OU process becomes a three-

dimensional Brownian motion and ${}_2F_2(\cdot; \cdot; \cdot)$ in (2.28) becomes unity; the EFPT then is $\rho^2/(6D)$ which is to be expected (Øksendal, 2013).

Unfortunately, (2.28) only pertains to OU processes that are isotropic with a single parameter λ , and the linearized-then-averaged system (2.26) is anisotropic with parameters $\epsilon\omega_1^2/2$, $\epsilon\omega_1^2/4$, and $\epsilon\omega_1^2/4$. To make use of the analytical formula (2.28), several numerical experiments were performed to determine a single value of λ that best characterizes three isotropic parameters. These simulations indicated that the geometric mean of the anisotropic parameters results in a useful approximation; that is,

$$\lambda \approx \frac{\epsilon\omega_1^2}{2\sqrt[3]{4}}, \quad (2.31)$$

for ϵ in (2.14) results in the theoretical EFPT (2.28) accurately approximating the EFPT for (2.26).

Given the analytical formula for the EFPT (2.28) and the approximation (2.31), the EFPT for the linearized-then-averaged system (2.26) out of the three-dimensional ball of radius $R^* - \bar{R}$ is

$$\mathbb{E} \left[\tau_{(R^* - \bar{R})} \right] = \left(\frac{\gamma_1}{3} \right) {}_2F_2 \left[1, 1; \frac{5}{2}, 2; \frac{\gamma_1\gamma_2}{2\sqrt[3]{4}} \right], \quad (2.32a)$$

$$\gamma_1 \triangleq \frac{(R^* - \bar{R})^2}{2D}, \quad (2.32b)$$

$$\gamma_2 \triangleq -K_p\omega_1^2\bar{R} \left(\frac{\partial f}{\partial \|\mathbf{x}\|} \Big|_{\|\mathbf{x}\|=\bar{R}} \right), \quad (2.32c)$$

for $\mathbf{e}(0) \stackrel{\text{a.s.}}{=} \mathbf{0}$. Although a general expression for the EFPT exists in (Graczyk and Jakubowski, 2008) for the case of a non-zero initial condition, in this work we will only consider the case where the focal volume begins sufficiently close to the particle so as to provide an upper bound for the expected tracking time until it is lost.

2.4.2 Numerical Characterization of First Passage Time

In the previous section, an analytical formula was provided for the approximate EFPT of the nonlinear system (2.25). This formula relies on two important approximations; the first approximation is the substitution of the linearized-then-averaged dynamics (2.26) for the full nonlinear dynamics, and the second approximation is the use of the geometric mean (2.31). To determine the validity of these of approximations and to provide guidance on selecting the user-defined parameters ω_1 , ω_2 , K_p , and \bar{R} , several numerical experiments were performed.

Both the linearized-then-averaged system (2.26) and the nonlinear system (2.25) were simulated for several parameter sets which were varied over a finite set of values. Specifically, ω_1 was varied among 10 Hz, 100 Hz, and 1000 Hz, D was varied among 0.5 s^{-2} , 1.0 s^{-2} , and 2.0 s^{-2} , and \bar{R} was varied between 0 and 1 with a granularity of 0.01. For all of these parameter choices, the value K_p was varied over three discrete values which were chosen individually for a given parameter set; these values will be specified later. For all simulations, the secondary frequency ω_2 was assumed to be exactly 1/4 the value of ω_1 within the respective simulation; this is valid since the value of ϵ has no dependence on ω_2 and the results from Sec. 2.3.3 indicate that choosing $\omega_2 < \omega_1$ should result in a stable system. Additionally, the PSF was assumed to be parabolic with a radius $R^* = 1$; specifically, this is

$$f(\|x\|) = \begin{cases} 1 - \|x\|^2 & \|x\| < 1 \\ 0 & \text{otherwise} \end{cases} \quad (2.33)$$

Both systems were simulated using the Euler-Maruyama method with a time step of $\Delta t = 10^{-8}$ s; since the diffusion coefficient is independent of the state, this simulation method achieves strong convergence of order 1.0 (Kloeden and Platen, 1999). All simulations proceeded until the exit condition was met and the resulting duration

was recorded. A total of 1000 simulations per parameter set were performed and the means of the first passage times were evaluated. The means for both systems are shown in Fig. 2·7.

Note that the shapes of the solid curves of respective color appear identical within each subfigure in Fig. 2·7. This is due to the carefully chosen values of K_p which were selected so that, given a value of D (*i.e.*, within a row), the resulting $\epsilon\omega_1^2$ value was equivalent. For example, ω_1 was reduced by a factor of 10 from subfigure (a) to subfigure (b); consequently, K_p was increased in (b) by a factor of 100 since $\epsilon \propto K_p$. Since the value of $\epsilon\omega_1^2$ is constant for a particular color and diffusion coefficient (*i.e.*, row), the solid curves are identical.

The resulting simulations illustrated in Fig. 2·7 indicate four important facts. First, the mean of the simulated EFPTs for the linearized-then-averaged system matches the theoretical EFPT. This can be seen by comparing the circle markers (*i.e.*, the mean value of the simulated EFPT) to the solid curve (*i.e.*, the theoretical EFPT) of the same color. This validates the use of the geometric mean (2.31) in the derivation of the EFPT (2.32).

The second fact pertains to selecting a value for ω_1 that maximizes the EFPT. First, in Fig. 2·7 note that the mean of the simulated EFPTs of the nonlinear system match the theoretical EFPTs for relatively large values of ω_1 . This can be seen by observing the ‘x’ markers (*i.e.*, the mean value of the simulated EFPTs for the nonlinear system) relative to the solid curve of the same color. As the primary frequency ω_1 decreases (*i.e.*, looking from left-to-right within the figure), not only does the accuracy of the theoretical EFPT decrease but the mean simulated EFPT approaches that of a pure Brownian motion. Further note that, given a fixed value of ω_1 , the accuracy of the theoretical EFPT decreases as the diffusion coefficient increases (*i.e.*, looking from top-to-bottom within the figure). These observations indicate two

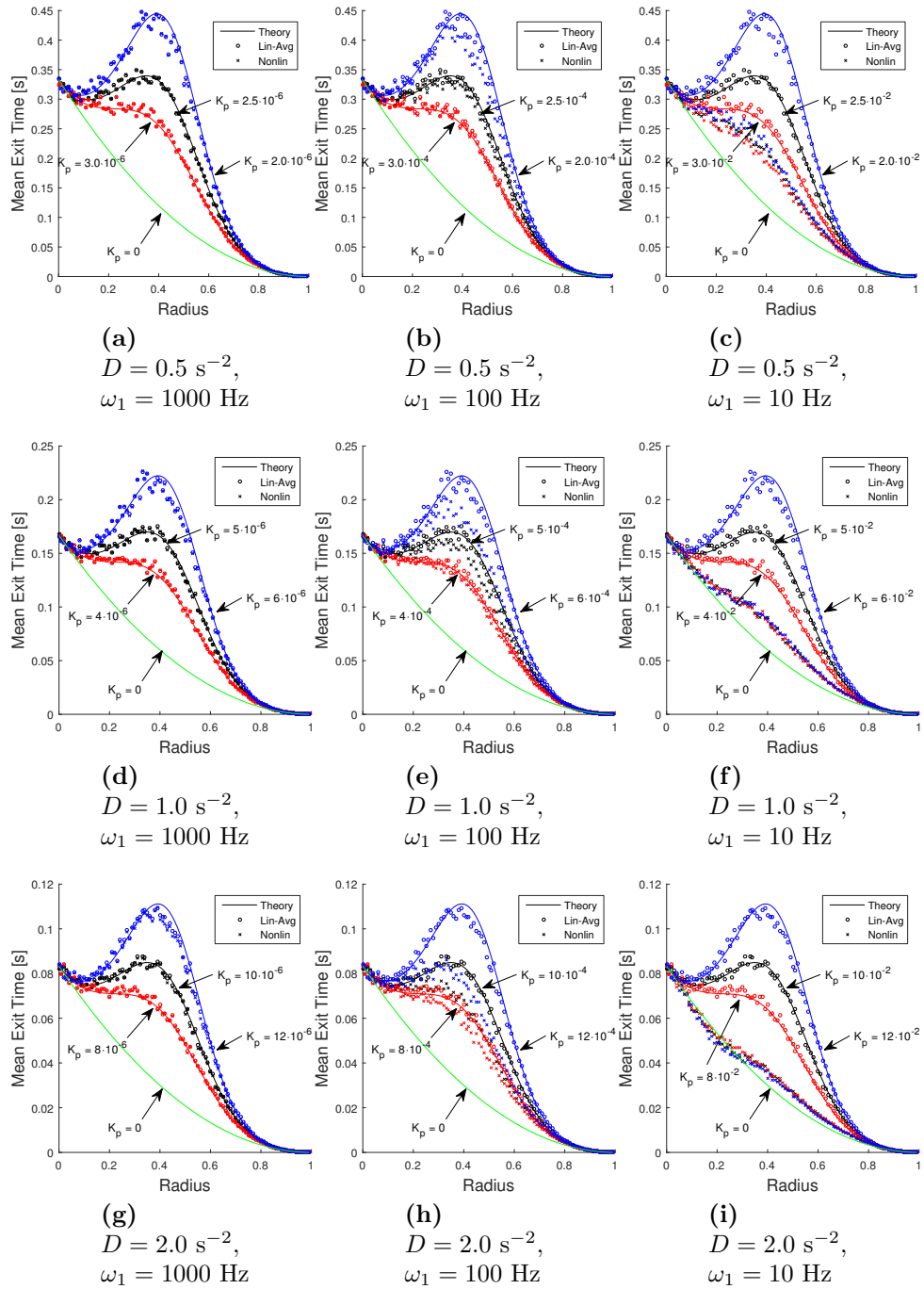


Figure 2-7: A comparison among the theoretical expected first passage time (2.32) (denoted as a solid line) and numerical simulations of the nonlinear system (2.25) (denoted by ‘x’ markers) and the linear-averaged system (2.26) (denoted by ‘o’ markers).

important facts governing the selection of ω_1 : (1) larger values of ω_1 increase the expected tracking time for a fixed value of ϵ , and (2) in order for the theoretical EFPT (2.32) to be an accurate representation of the nonlinear system (2.25), the time period corresponding to ω_1 must be small (*e.g.*, two orders of magnitude) relative to $(R^*)^2/(6D)$. This is expected due to the fact that the theoretical expected passage time is derived from the linearized-then-averaged system which relies upon averaging over a full period. Thus, to maximize the EFPT, one should select ω_1 as large as possible subject to the bandwidths allowed by the microscope's hardware.

The third fact pertains to choosing an optimal gain K_p that maximizes the EFPT given a value of ω_1 and D . We now turn our attention to Fig. 2-8 which shows the theoretical EFPT as a function of radius \bar{R} for six distinct values of K_p and for a given value of ω_1 and D . It appears that increasing K_p (ordered from red indicating small to violet indicating largest) introduces a bump near the middle of the curve. It is clear that as K_p increases, this bump increases in magnitude; as to be expected, as K_p approaches infinity the EFPT approaches infinity as well. This phenomenon is reminiscent of a first order system in negative feedback with a proportional gain. However, the influence of noise and other disturbances prohibits increasing K_p too far without risking significant noise amplification or instability. Since K_p amplifies the field measurement in the determination of θ (2.2), K_p should be chosen large enough subject to the measurement noise of the microscope.

The final fact pertains to choosing an optimal radius \bar{R} that maximizes the EFPT given a value of ω_1 , K_p , and D . In Fig. 2-8, observe the nature of the bump that occurs as K_p increases from zero. Note that for significantly small values of K_p (*e.g.*, shown by the red and orange dash-dotted curves), the radius \bar{R} that maximizes the EFPT is zero. This indicates that if K_p is chosen too small, the optimal solution is to not attempt to track the particle at all. However, there exists a critical point,

indicated by the black solid curve in Fig. 2·8 where the optimal radius is no longer zero. This discrete jump indicates that the optimal radius bifurcates as a function of K_p . As K_p is subsequently increased (indicated by the green, blue, and violet dashed curves in Fig. 2·8), the optimal radius continues to increase to approximately $R^*/2$. Unfortunately, a closed-form expression for the optimal radius does not exist, although it can be solved for numerically.

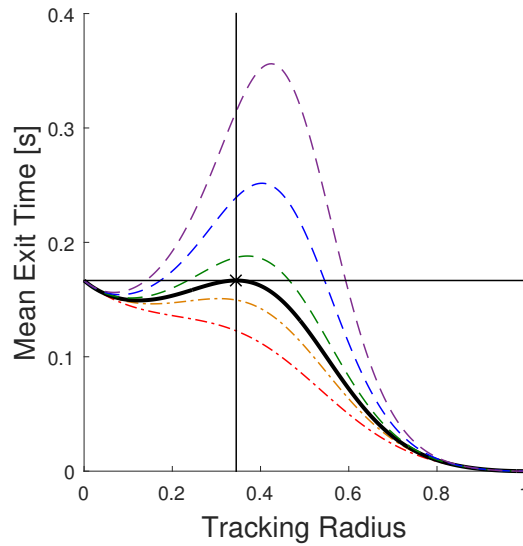


Figure 2·8: The expected first passage time (2.32) as a function of the tracking radius $\bar{R} = v/\omega_1$ as K_p increases. The point spread function for this figure was parabolic with a radius $R^* = 1$ and the particle location was diffusing with $D = 1.0$. Relatively low values of K_p are shown by dash-dotted curves in red and orange, and relatively large values are shown by dashed curves in green, blue, and violet. The black solid curve represents the expected first passage time at the bifurcation point which is denoted by the ‘x’ marker. Note that for small values of K_p the optimal tracking radius is zero; this indicates that if K_p is too low, then the expected first passage time will be maximized by not tracking at all. When K_p is increased to a critical value, however, the optimal tracking radius discontinuously changes to the solid vertical line (here, $R_{\text{Bif}} \approx 0.34$). As K_p is subsequently increased beyond the bifurcation point, the expected first passage time increases in conjunction with the optimal tracking radius.

2.5 Summary

The confocal microscope is an extension of the widefield fluorescent microscope that allows for three-dimensional imaging via optical sectioning. Unlike the widefield microscope, however, the confocal microscope acquires images by moving the location of the focal volume relative to the sample and by measuring the intensity at various locations. An important characteristic of the confocal microscope is that, when imaging a point-source, the point spread function has a maximum collocated with the position of the point-source. Thus, a potential method for tracking the a fluorescent particle would be to seek the maximum of the resulting point spread function.

In this chapter, a feedback algorithm which is capable of tracking a fluorescent particle in a confocal microscope has been presented. We have provided theoretical and numerical results for two distinct cases. We first considered the case of a stationary particle and proved the existence of an equilibrium trajectory. In addition, we proved stability of the equilibrium trajectory and characterized it as a function of the controller parameters by using Floquet theory. We then considered the case where the particle was diffusing and the PSF exhibited bounded support. In this case, we derived a metric for tracking performance based on the expected first passage time and proceeded to numerically characterize it using simulations. With this characterization, we provide insight on parameter selection that maximizes this performance metric.

The presented tracking method is novel for several reasons. The method, which is an active tracking method, requires no online localization and is computationally simple to implement. Thus, the algorithm is especially applicable to systems with tight real-time constraints and with high update-rates. Since the algorithm does not require localization it also does not require a priori knowledge of the particle's motion or the microscope's PSF aside from the existence of a maximum. In addi-

tion, the trajectories generated by the algorithm are smooth and do not produce any discontinuous jumps. Lastly, the method may implemented in a variety of confocal microscopes without requiring any non-standard hardware.

Chapter 3

Inference for Particle Tracking Experiments

Recall from Chapter 1 that the common paradigm for inferring information from particle tracking data is sequential in nature. As such, it usually involves the process of first localizing the particle within each image and subsequently applying some form of regression analysis to estimate model parameters (for example, diffusion coefficients). This procedure, however, is inherently problematic for several reasons. First, separately localizing the particle within each frame without regard to the entire data set and some model of the particle's motion could potentially reduce the precision of localization. In addition, most localization methods only produce point-estimates of the particle's location given that specific image. Moreover, most optimal methods of parameter estimation are limited to a purely diffusive motion model with normally distributed localization error.

In this chapter, we present an inference method which solves the aforementioned problems and limitations. The method, which was originally presented in the context of nonlinear system identification (Schön et al., 2011), incorporates both the Expectation Maximization (EM) algorithm and Sequential Monte Carlo (SMC) methods to calculate two important quantities. First, the algorithm produces an approximation of the posterior probability density (*i.e.*, conditioned on the entire measurement history) of the particle's location at a given time. Moreover, the algorithm provides approximate Maximum Likelihood (ML) estimates for potentially nonlinear motion

and observation models. Thus, the method can be applied in a large variety of microscopy-related scenarios, including both widefield and confocal imaging modalities. The method is iterative and both localization and parameter estimation are cyclical, unlike the common paradigm which is serial.

This chapter is organized as follows. First, we provide an overview of the method in the context of tracking fluorescent particles. We then present several biologically-inspired models of particle motion and explain how the algorithm may be used in each case. We then show the effectiveness of the method by applying it to simulated widefield tracking data. The material presented in this chapter is based on (Ashley and Andersson, 2015a; Ashley and Andersson, 2015b).

3.1 Problem Statement

Consider the problem of identifying an unknown fixed parameter $\theta \in \mathbb{R}^{n_\theta}$ for the state and observation models

$$\mathbf{x}_{\mathbf{p},1} \sim p_\theta^{\text{Init}}(\mathbf{x}_{\mathbf{p},1}), \quad (3.1)$$

$$\mathbf{x}_{\mathbf{p},k+1} \sim p_\theta^{\text{Mot}}(\mathbf{x}_{\mathbf{p},k+1} | \mathbf{x}_{\mathbf{p},k}), \quad (3.2)$$

$$I_k^{1:P} \sim p_\theta^{\text{Obs}}(I_k^{1:P} | \mathbf{x}_{\mathbf{p},k}, \mathbf{x}_{\mathbf{s},k}^{1:P}). \quad (3.3)$$

In this work, we use the notation $I_{1:k}$ to denote a collection from index 1 to k , *i.e.*, $I_{1:k} \triangleq \{I_1, I_2, \dots, I_k\}$; in the case of a pair of indices, a collection of all possible pairs is implied such that $I_{1:k}^{1:p} \triangleq \{I_1^1, I_1^2, \dots, I_1^p, I_2^1, I_2^2, \dots, I_2^p, \dots, I_k^p\}$. Here, the state $\mathbf{x}_{\mathbf{p},k} \in \mathbb{R}^{n_x}$ is an n_x -dimensional vector indexed by discrete time k , the measurement $I_k^p \in \mathbb{R}$ is a scalar indexed by both discrete time k and pixel p , and the input $\mathbf{x}_{\mathbf{s},k}^p \in \mathbb{R}^{n_x}$ is an n_x -dimensional vector indexed by both discrete time k and pixel p . We assume that the forms of probability densities $p_\theta(\cdot | \cdot)$ are of known form. Additionally, only $N \times P$ scalar measurements $I_{1:N}^{1:P}$ are available from which to estimate θ .

In the context of particle tracking, the state $\mathbf{x}_{\mathbf{p},k}$ denotes the location of the particle in either two or three dimensions at a discrete time index k . The distribution p_{θ}^{Init} describes the probability distribution of the particle location at the start of the experiment. The motion model p_{θ}^{Mot} is a probability distribution describing how the particle evolves in time and may be given by a diffusion, directed motion, or other dynamic process. The observation model describes the fluorescent measurement process. For example, assuming a widefield imaging modality, $I_k^{1:P}$ signifies a pixilated image consisting of P pixels acquired at discrete time k . The observation model $p_{\theta}^{\text{Obs}}(\cdot)$ is a probability distribution capturing the statistics of the measurement process itself and may involve, for example, Poisson-distributed shot noise, Gaussian read-out noise, or other features specific to the experimental setting. The parameter θ may describe properties of the motion (such as diffusion coefficients) as well as of the observation process (such as peak intensity). The input $\mathbf{x}_{\mathbf{s},k}^p$ is the position of the pixel p which, in conjunction with the particle position $\mathbf{x}_{\mathbf{p},k}$, yields the scalar measurement I_k^p . For example, in the context of widefield imaging, $\mathbf{x}_{\mathbf{s},k}^{1:P}$ could represent the center positions of each of the camera pixels with respect to a fixed reference frame. If preprocessing (*e.g.*, segmentation) of the images is done which centers the particle's image within each frame, then $\mathbf{x}_{\mathbf{s},k}^p$ represents the resulting center position (relative to a fixed reference frame) of the p th pixel at the k th time. Moreover, in the context of confocal tracking by the algorithm presented in Chapter 2, $\mathbf{x}_{\mathbf{s},k}^p$ represents the position of the focal volume at discrete time k ; in this context, $p = 1$ since only one measurement is taken at each time instant. It is critical to note that $\mathbf{x}_{\mathbf{s},k}^p$ is a deterministic quantity and that it does not influence the particle's motion. Moreover, we specifically define $\mathbf{x}_{\mathbf{s},k}^p$ to be in the object space of the imaging process rather than the image space.

One aim of the proposed inference method is to estimate the parameter θ . While

many different techniques could be used, we focus on the maximum likelihood estimator due to its well-characterized properties, including asymptotic consistency, efficiency, and normality (Pawitan, 2001). Deriving the maximum likelihood estimate involves maximizing the joint density (i.e. the likelihood) of the observations conditioned on the parameter θ ,

$$\hat{\theta} = \arg \max_{\theta} \log p_{\theta}(I_{1:N}^{1:P}). \quad (3.4)$$

It is most often the case that this density is unknown or intractable, and, consequently, an ML estimate cannot be derived analytically. For example, in the context of tracking a single particle, (3.4) corresponds to attempting to estimate motion and observation parameters directly from the image data, without knowledge of the particle trajectory. When the density in (3.4) is unknown or intractable, the EM algorithm provides an alternative for finding the ML estimate.

3.2 The Expectation Maximization Algorithm

The EM algorithm, originally proposed in (Dempster et al., 1977), is a numerical, iterative method for calculating ML estimates that is typically used when the joint density $p_{\theta}(\mathbf{x}_{\mathbf{p},1:N}, I_{1:N}^{1:P})$ is known, where $\mathbf{x}_{\mathbf{p},1:N}$ is often called the *latent* set of random variables. Instead of calculating the full likelihood by integrating the joint density over the full domain of the latent state, the EM algorithm approximates the likelihood by conditionally averaging over the latent state; mathematically, this is given by

$$Q(\theta, \hat{\theta}_e) \triangleq \int \log \left[p_{\theta}(\mathbf{x}_{\mathbf{p},1:N}, I_{1:N}^{1:P}) \right] p_{\hat{\theta}_e}(\mathbf{x}_{\mathbf{p},1:N} | I_{1:N}^{1:P}) d\mathbf{x}_{\mathbf{p},1:N}. \quad (3.5)$$

In the context of particle tracking, the latent state is the trajectory of the particle, and thus EM takes advantage of the coupling between the trajectory and the image data as encapsulated by the motion (3.2) and observation models (3.3).

Note that the expectation in (3.5) is with respect to the conditional density $p_{\hat{\theta}_e}(\mathbf{x}_{\mathbf{p},1:N}|I_{1:N}^{1:P})$ with $\hat{\theta}_e$ defined to be some estimate for θ at iteration e . It was shown in (Dempster et al., 1977) that for each choice of $\hat{\theta}_{e+1}$ such that $Q(\hat{\theta}_{e+1}, \hat{\theta}_e) > Q(\hat{\theta}_e, \hat{\theta}_e)$, the likelihood $p_{\hat{\theta}_{e+1}}(I_{1:N}^{1:P})$ subsequently increases. One method to guarantee an increase for each iteration is to update the new value so that

$$\hat{\theta}_{e+1} = \arg \max_{\theta} Q(\theta, \hat{\theta}_e). \quad (3.6)$$

By alternating between the expectation and maximization steps, Q as defined in (3.5) will converge to a (local) maximum as e becomes large, and, consequently, $\hat{\theta}_e$ will converge to a (local) ML estimate of θ .

Implementation of the EM algorithm requires evaluation of $Q(\theta, \hat{\theta}_e)$. A tedious but straightforward calculation (see (Schön et al., 2011)) allows (3.5) to be rewritten as

$$Q(\theta, \hat{\theta}_e) = Q_1 + Q_2 + Q_3, \quad (3.7)$$

where

$$Q_1 \triangleq \int \log \left[p_{\theta}^{\text{Init}}(\mathbf{x}_{\mathbf{p},1}) \right] p_{\hat{\theta}_e}(\mathbf{x}_{\mathbf{p},1}|I_{1:N}^{1:P}) d\mathbf{x}_{\mathbf{p},1}, \quad (3.8a)$$

$$Q_2 \triangleq \sum_{k=1}^{N-1} \int \int \log \left[p_{\theta}^{\text{Mot}}(\mathbf{x}_{\mathbf{p},k+1}|\mathbf{x}_{\mathbf{p},k}) \right] p_{\hat{\theta}_e}(\mathbf{x}_{\mathbf{p},k+1}, \mathbf{x}_{\mathbf{p},k}|I_{1:N}^{1:P}) d\mathbf{x}_{\mathbf{p},k} d\mathbf{x}_{\mathbf{p},k+1}, \quad (3.8b)$$

$$Q_3 \triangleq \sum_{k=1}^N \int \log \left[p_{\theta}^{\text{Obs}}(I_k^{1:P}|\mathbf{x}_{\mathbf{p},k}, \mathbf{x}_{\mathbf{s},k}^{1:P}) \right] p_{\hat{\theta}_e}(\mathbf{x}_{\mathbf{p},k}|I_{1:N}^{1:P}) d\mathbf{x}_{\mathbf{p},k}. \quad (3.8c)$$

Here, (3.8a) corresponds to the initial distribution (3.1), (3.8b) corresponds to the motion model (3.2), and (3.8c) corresponds to the observation model (3.3). The calculation of these expressions require evaluation of the posterior density $p_{\hat{\theta}_e}(\mathbf{x}_{\mathbf{p},k+1}|I_{1:N}^{1:P})$ and the sequential-pairwise joint posterior density $p_{\hat{\theta}_e}(\mathbf{x}_{\mathbf{p},k+1}, \mathbf{x}_{\mathbf{p},k}|I_{1:N}^{1:P})$; these are,

unfortunately, challenging to compute in most cases. For the case where both the motion and observation models constitute a linear, time-invariant system, the posterior densities are Gaussian with sufficient statistics calculated by optimal estimation methods such as the Kalman filter and smoother (Rauch et al., 1965). In general, however, the underlying models are nonlinear and non-Gaussian in nature, such as when the particle motion follows a confined diffusion or when the presence of Poisson-distributed shot noise is accounted for explicitly in the observation model. In this work, these difficulties are overcome by using Sequential Monte Carlo (SMC) methods to simplify (3.7) by approximating the posterior densities as discrete, weighted sums of delta functions.

3.2.1 Sequential Monte Carlo

SMC methods approximate the conditional posterior densities in (3.8b) and (3.8c) at each EM iteration e by assuming they may be approximated by a weighted sum of M randomly-drawn point estimates such that

$$p_{\hat{\theta}_e}(\mathbf{x}_{\mathbf{p},k} | I_{1:N}^{1:P}) \approx \sum_{i=1}^M w_{k|N,e}^i \delta(\mathbf{x}_{\mathbf{p},k} - \mathbf{x}_{k|N,e}^i), \quad (3.9a)$$

$$p_{\hat{\theta}_e}(\mathbf{x}_{\mathbf{p},k}, \mathbf{x}_{\mathbf{p},k+1} | I_{1:N}^{1:P}) \approx \sum_{i=1}^M \sum_{j=1}^M w_{k|N,e}^{ij} \delta(\mathbf{x}_{\mathbf{p},k} - \mathbf{x}_{k|N,e}^i, \mathbf{x}_{\mathbf{p},k+1} - \mathbf{x}_{k+1|N,e}^j), \quad (3.9b)$$

where $\mathbf{x}_{k|N,e}^i$ is the i th Monte Carlo estimate of $\mathbf{x}_{\mathbf{p},k}$ at discrete time k and EM iteration e , $\delta(\cdot)$ is a Dirac delta function, and $w_{k|N,e}^i$ and $w_{k|N,e}^{ij}$ are weights determined by how well the point estimates approximate the posterior distribution. The value of these weights are driven in part by determining how likely the i th measurement was given the point estimate $\mathbf{x}_{k|N,e}^i$. In the context of tracking particles, this is equivalent to setting the weight by how likely it was to acquire the actual image data assuming that the particle was at the position of the point estimate. A general

treatment for how these estimates and weights are calculated is beyond the scope of this thesis and has been established elsewhere (Doucet and Johansen, 2011; Doucet et al., 2001; Sanjeev Arulampalam et al., 2002). In the work that follows, we use two specific algorithms, namely the Sampling Importance Resampling (SIR) algorithm and the Forward-Filtering Backward-Smoothing (FFBS) algorithm, in the subsequent demonstrations.

One approach to calculate the approximate posterior densities (3.9) is to break the process into two steps. The first step, known as the *filtering step*, calculates the approximate posterior densities $p_{\hat{\theta}_e}(\mathbf{x}_{\mathbf{p},k}|I_{1:k}^{1:P})$ for $k = 1, \dots, N$; here, the SIR algorithm is used (Cappe et al., 2007). The second step, known as the *smoothing step*, operates backward in time on the posterior densities produced in the filtering step to produce the densities in (3.9); here, the FFBS algorithm is used (Lindsten and Schön, 2013). A brief description of these two methods is given in Appendix A.

Upon application of the SMC approximation (3.9) to the calculation of $Q(\theta, \hat{\theta}_e)$ in (3.7), one obtains the approximation

$$Q(\theta, \hat{\theta}_e) \approx \hat{Q}(\theta, \hat{\theta}_e) = \hat{Q}_1 + \hat{Q}_2 + \hat{Q}_3, \quad (3.10)$$

where

$$\hat{Q}_1 \triangleq \sum_{i=1}^M w_{1|N,e}^i \log [p_{\theta}^{\text{Init}}(\mathbf{x}_{1|N,e}^i)], \quad (3.11a)$$

$$\hat{Q}_2 \triangleq \sum_{k=1}^{N-1} \sum_{i=1}^M \sum_{j=1}^M w_{k|N,e}^{ij} \log [p_{\theta}^{\text{Mot}}(\mathbf{x}_{k+1|N,e}^j | \mathbf{x}_{k|N,e}^i)], \quad (3.11b)$$

$$\hat{Q}_3 \triangleq \sum_{k=1}^N \sum_{i=1}^M w_{k|N,e}^i \log [p_{\theta}^{\text{Obs}}(I_k^{1:P} | \mathbf{x}_{k|N,e}^i, \mathbf{x}_{\mathbf{s},k}^{1:P})], \quad (3.11c)$$

Note the similarities between (3.8) and (3.11); the SMC approximation of the posterior densities transforms potentially intractable integrals into straightforward sum-

mations. The SMC-based EM algorithm proceeds by calculating $\hat{Q}(\theta, \hat{\theta}_e)$ for some $\hat{\theta}_e$ and then by updating the estimate according to

$$\hat{\theta}_{e+1} = \arg \max_{\theta} \hat{Q}(\theta, \hat{\theta}_e). \quad (3.12)$$

These two steps, namely the calculation of $\hat{Q}(\theta, \hat{\theta}_e)$ via SMC (abbreviated as the *expectation step*) and its subsequent maximization over θ (abbreviated as the *maximization step*), are repeated until some convergence criterion is satisfied. For the remainder of this thesis, this process is abbreviated as the SMC-EM algorithm.

It is to be noted that the SMC-EM algorithm, unlike the original EM algorithm, provides no guarantee of convergence to a (local) maximum. However, as the number of estimates M becomes large, \hat{Q} approaches Q , thereby implying greater likelihood of converging to an extremum. Analysis of this behavior is further detailed in (Schön et al., 2011).

3.3 Relevant Models in Fluorescence Microscopy

In this section, we present several motion and observation models that are relevant to biological imaging. The models presented here may be incorporated into the SMC-EM algorithm and will be used in the demonstrations that follow.

3.3.1 Brownian Motion

The first motion model considered is a Brownian motion. This model is applicable to a large number of situations related to biology, including those involving membrane dynamics and viral trafficking (Nelson, 2013). Assuming the motion for each axis is independent and distinct, then, for the x axis in particular, the motion can be

represented by the difference equation

$$x_{k+1} = x_k + \sqrt{2D_x \Delta t'} w_k, \quad (3.13)$$

where D_x is the diffusion coefficient, $\Delta t'$ is the sampling period, and w_k is a standard normal random variable. The transition density for this model is given by the solution to the diffusion equation (Risken, 1996) and takes the form of a normal distribution; thus, the transition density for the x axis is

$$p(x_{k+1}|x_k) = \frac{1}{\sqrt{4\pi D_x \Delta t'}} \exp \left[-\frac{(x_{k+1} - x_k)^2}{4D_x \Delta t'} \right]. \quad (3.14)$$

Implementation of this motion model in the expectation step of the SMC-EM algorithm is a straightforward process since it only requires drawing samples from a normal distribution. Sampling from a normal distribution may be done with a variety of methods; see, for example, (Press et al., 2007).

During the maximization step of the SMC-EM algorithm, maximizing (3.12) with respect to D_x yields

$$\hat{D}_{x,e+1} = \frac{1}{2N\Delta t'} \sum_{k=1}^{N-1} \sum_{i=1}^M \sum_{j=1}^M w_{k|N,e}^{ij} \left(x_{k+1|N,e}^j - x_{k|N,e}^i \right)^2, \quad (3.15)$$

which is the resulting optimal diffusion coefficient for the x axis at the e th EM iteration. For the anisotropic case where the positions in all axes are generated by independent and distinct Brownian motions, then the optimal diffusion coefficient for each axis is given by the same formula (3.15) but with the respective position estimates inserted instead of x . For the isotropic case where the positions in all axes are generated by independent Brownian motions but with the same diffusion coefficient D , then D may be calculated as the average of each axis's diffusion coefficient; for example, $\hat{D}_{e+1} = \frac{1}{3} \left(\hat{D}_{x,e+1} + \hat{D}_{y,e+1} + \hat{D}_{z,e+1} \right)$ is the optimal diffusion coefficient for

a three-dimensional isotropic Brownian motion.

3.3.2 Diffusive Directed Motion

Deterministic flow is often present within biological samples. For example, the trajectory of a molecular motor is dependent on the curvature of the filament to which it is attached. Assuming the motion for each axis is independent and distinct, then a simple model for a directed motion in a given direction is given by the difference equation

$$x_{k+1} = x_k + V_x \Delta t' + \sqrt{2D_x \Delta t'} w_k, \quad (3.16)$$

where D_x is the diffusion coefficient, V_x is the speed, $\Delta t'$ is the sampling interval, and w_k is a standard normal random variable. The transition density is very similar to that of a Brownian motion and is given by

$$p(x_{k+1}|x_k) = \frac{1}{\sqrt{4\pi D_x \Delta t'}} \exp \left[-\frac{(x_{k+1} - x_k - V_x \Delta t')^2}{4D_x \Delta t'} \right]. \quad (3.17)$$

Implementation of the expectation step in SMC-EM is similar to that of the diffusion described in the previous section. As such, samples may be generated by sampling from a normal distribution but with a mean of $x_k + V_x \Delta t'$.

For the maximization step of SMC-EM, maximizing (3.12) with respect to V_x and D_x yields

$$\hat{V}_{x,e+1} = \frac{1}{N \Delta t'} \sum_{k=1}^{N-1} \sum_{i=1}^M \sum_{j=1}^M w_{k|N,e}^{ij} \left(x_{k+1|N,e}^j - x_{k|N,e}^i \right), \quad (3.18)$$

$$\hat{D}_{x,e+1} = \frac{1}{2N \Delta t'} \sum_{k=1}^{N-1} \sum_{i=1}^M \sum_{j=1}^M w_{k|N,e}^{ij} \left(x_{k+1|N,e}^j - x_{k|N,e}^i - \hat{V}_{x,e+1} \Delta t' \right)^2, \quad (3.19)$$

which are the optimal speed and diffusion coefficient (respectively) in the x axis at the e th EM iteration. For a multidimensional diffusive flow, the optimal speeds and

diffusion coefficients for both the anisotropic and the isotropic cases follow similarly to the Brownian motion case.

3.3.3 Confined Diffusion

Although unconstrained Brownian motion is typically assumed in practice, it is often not the case in real biological systems. For example, proteins on a membrane are “corralled” by other skeletal membrane proteins which inhibits their motion (Sheetz et al., 1980). As an example of this, we consider a diffusion that is confined to the interval $[-L_x/2, L_x/2]$ with L_x defining the length of the confinement channel. The transition density for this axis (here, given by x) is given by the solution to the diffusion equation with reflecting boundaries at $x = -L_x/2$ and $x = +L_x/2$, which is

$$p(x_{k+1}|x_k) = \frac{1}{L_x} + \frac{2}{L_x} \sum_{n=1}^{\infty} \exp \left[-D_x \Delta t' \left(\frac{n\pi}{L_x} \right)^2 \right] \times \cos \left[\frac{n\pi}{L_x} \left(x_{k+1} + \frac{L_x}{2} \right) \right] \cos \left[\frac{n\pi}{L_x} \left(x_k + \frac{L_x}{2} \right) \right]; \quad (3.20)$$

a derivation is provided in (Carslaw and Jaeger, 1959).

Generation of samples from this distribution during the expectation step of SMC-EM is more complicated than generating samples of a Brownian motion or a directed diffusion. In cases where samples cannot be easily derived from a distribution, the method known as rejection sampling may be employed (Robert and Casella, 2005). To generate a sample x_{k+1} from (3.20) given x_k using rejection sampling, first a bound K must be selected such that $K > L_x \max_{x_{k+1}} [p(x_{k+1}|x_k)]$. With K fixed, two independent samples are drawn: $u \sim \mathcal{U}(0, 1)$ and $x_{\text{cand}} \sim \mathcal{U}(-\frac{L_x}{2}, \frac{L_x}{2})$, where $\mathcal{U}(0, 1)$ represents a standard uniform distribution. If $u < (\frac{L_x}{K}) p(x_{\text{cand}}|x_k)$ is satisfied, then x_{cand} is accepted as the random deviate; otherwise, u and x_{cand} are resampled and the process repeats.

In the context of the SMC-EM algorithm, the optimal value for the length of the

confinement channel is found by inserting the motion model (3.20) into (3.12), using the SMC approximation (3.11), and then maximizing. This yields

$$\hat{L}_{x,e+1} = \max_{k,i} 2 |x_{k|N,e}^i|, \quad (3.21)$$

implying that the best estimate for the length of the channel is the absolute maximum position estimate.

It is important to note that the initial value for the length parameter estimate *must* be greater than its corresponding true value to guarantee convergence. To see this, consider the length parameter estimate $\hat{L}_{x,e}$. During the expectation step at iteration $e + 1$, position estimates generated according to (3.20) will be constrained to the interval $[-\hat{L}_{x,e}/2, \hat{L}_{x,e}/2]$. During the subsequent maximization step, \hat{L}_{e+1} is set to be the absolute maximum of every position estimate via (3.21). From this, it follows that $\hat{L}_{x,e+1} \leq \hat{L}_{x,e}$. As such, in practice, the user must always set the initial length parameter estimate to a value that overestimates the true length.

Unfortunately, there is no analytical solution for the confined diffusion coefficient. Thus, (3.12) must be maximized numerically with respect to D_x . For the simple case where the motion in each axis is distinct and independent, however, \hat{D}_x can be numerically calculated by solving a one-dimensional unconstrained optimization problem via, for example, the bisection method.

3.3.4 Elastic Tethering

We next consider the case where a particle is elastically tethered to a fixed anchor. This model is common in the case of tethered particle microscopy where one end of biopolymer is fixed to a coverslip and a fluorescent particle is attached the other (free) end; the position of the bead over time yields information regarding the structure of the biopolymer (see, e.g. (Nelson et al., 2006)). We assume the location of the

tethering point is known and fixed to the origin and that the tether is sufficiently stiff and obeys Hook's law. Inspired by the model presented in (Beausang et al., 2007), the position of the particle can be modeled by the Ornstein-Uhlenbeck process with transition density

$$p(x_{k+1}|x_k) = \sqrt{\frac{A_x}{2\pi D_x (1 - e^{-2A_x \Delta t'})}} \exp \left\{ -\frac{A_x}{2D_x} \left[\frac{(x_{k+1} - x_k e^{-A_x \Delta t'})^2}{1 - e^{-2A_x \Delta t'}} \right] \right\}, \quad (3.22)$$

in the x axis. The stiffness coefficient $A_x > 0$ and the diffusion coefficient D_x both determine the behavior of the motion about the tethered point.

Implementation of the expectation step within the SMC-EM algorithm is similar to that of the Brownian motion and directed diffusion cases. In particular, note that (3.22) is of the form of a normal distribution with mean and variance

$$\mu_{\text{OU}} = x_k e^{-A_x \Delta t'}, \quad (3.23)$$

$$\sigma_{\text{OU}}^2 = \left(\frac{D_x}{A_x} \right) \left(1 - e^{-2A_x \Delta t'} \right); \quad (3.24)$$

thus, samples may be drawn from a normal distribution with appropriate scale and bias.

We break the maximization step of the SMC-EM algorithm into two separate scenarios. We first consider the case where the motion is independent for each axis but is isotropic, meaning that each axis has the same stiffness coefficient A and diffusion coefficient D . For the three-dimensional case, maximization of (3.12) with respect to A yields

$$\hat{A}_{e+1} = -\frac{1}{\Delta t} \log \left(\frac{\alpha_e}{\beta_e} \right) \quad (3.25)$$

with α_e and β_e defined by

$$\alpha_e = \sum_{k=1}^{N-1} \sum_{i=1}^M \sum_{j=1}^M w_{k|N,e}^{ij} \left(\alpha_{k,e}^{ij,a} + \alpha_{k,e}^{ij,b} + \alpha_{k,e}^{ij,c} \right), \quad (3.26a)$$

$$\alpha_{k,e}^{ij,a} = x_{k+1|N,e}^j \cdot x_{k|N,e}^i, \quad (3.26b)$$

$$\alpha_{k,e}^{ij,b} = y_{k+1|N,e}^j \cdot y_{k|N,e}^i, \quad (3.26c)$$

$$\alpha_{k,e}^{ij,c} = z_{k+1|N,e}^j \cdot z_{k|N,e}^i, \quad (3.26d)$$

$$\beta_e = \sum_{k=1}^{N-1} \sum_{i=1}^M \sum_{j=1}^M w_{k|N,e}^i \left(\beta_{k,e}^{i,a} + \beta_{k,e}^{i,b} + \beta_{k,e}^{i,c} \right), \quad (3.27a)$$

$$\beta_{k,e}^{i,a} = \left(x_{k|N,e}^i \right)^2, \quad (3.27b)$$

$$\beta_{k,e}^{i,b} = \left(y_{k|N,e}^i \right)^2, \quad (3.27c)$$

$$\beta_{k,e}^{i,c} = \left(z_{k|N,e}^i \right)^2. \quad (3.27d)$$

Similarly, the parameter update equation for the diffusion coefficient D is given by

$$\hat{D}_{e+1} = \frac{\gamma_e \hat{A}_{e+1}}{3N \left(1 - \exp \left(-2\hat{A}_{e+1} \Delta t \right) \right)} \quad (3.28)$$

with γ_e defined by

$$\gamma_e = \sum_{k=1}^{N-1} \sum_{i=1}^M \sum_{j=1}^M w_{k|N,e}^{ij} \left(\gamma_{k,e}^{ij,a} + \gamma_{k,e}^{ij,b} + \gamma_{k,e}^{ij,c} \right), \quad (3.29a)$$

$$\gamma_{k,e}^{ij,a} = \left(x_{k+1|N,e}^j - x_{k|N,e}^i \cdot e^{-2\Delta t \hat{A}_e} \right)^2, \quad (3.29b)$$

$$\gamma_{k,e}^{ij,b} = \left(y_{k+1|N,e}^j - y_{k|N,e}^i \cdot e^{-2\Delta t \hat{A}_e} \right)^2, \quad (3.29c)$$

$$\gamma_{k,e}^{ij,c} = \left(z_{k+1|N,e}^j - z_{k|N,e}^i \cdot e^{-2\Delta t \hat{A}_e} \right)^2. \quad (3.29d)$$

Note that the determination of the isotropic parameters A and D are not linear combinations of the anisotropic parameters for each individual axis as they are in the

diffusive case. For the scenario where each axis is independent and anisotropic, then the resulting parameters are of similar form to (3.25) and (3.28) but with $\alpha_e, \beta_e, \gamma_e$ determined by the positions of each individual axis instead.

3.3.5 Normally Distributed Initial Condition

It is most often the case that the initial position of the particle is unknown. A simple model for the initial position of the particle consists of a normal distribution with unknown mean and variance; in the x axis for example, $x_1 \sim \mathcal{N}(\mu_x, \sigma_x^2)$. Implementation of the expectation step in SMC-EM involves drawing samples from a normal distribution. Evaluation of (3.12) with respect to the mean and variance yields

$$\hat{\mu}_{x,e+1} = \sum_{i=1}^M w_{1|N,e}^i x_{1|N,e}^i, \quad (3.30)$$

$$\hat{\sigma}_{x,e+1}^2 = \sum_{i=1}^M w_{1|N,e}^i (x_{1|N,e}^i - \hat{\mu}_{x,e+1})^2. \quad (3.31)$$

3.3.6 Poissonian Shot Noise

A potential noise source during the imaging process, often termed *shot noise*, is due to the quantized nature of light as discrete packets of photons are received by each camera pixel. Since this is the prevalent noise source for widely used CCD cameras and APDs, we next explain how to incorporate this as an observation model in SMC-EM. It is to be noted that other devices, such as electron-multiplying CCDs (EMCCD), exhibit more complicated noise models (Moran et al., 1997; Chao et al., 2012) and could also be incorporated into the SMC-EM framework described in this thesis.

To model the effect of shot noise, we assume the measurement I_k^p acquired at time k and pixel p is modeled as a Poisson random variable with a mean λ_k^p determined by the location of the particle $\mathbf{x}_{\mathbf{p},k}$ and the location of the respective pixel $\mathbf{x}_{\mathbf{s},k}^p$. We further assume the measurement acquired by each pixel is independent given the

position of the particle. The observation density in the form of (3.3) is therefore

$$p \left(I_k^{1:P} \mid \mathbf{x}_{\mathbf{p},k}, \mathbf{x}_{\mathbf{s},k}^{1:P} \right) = \prod_{p=1}^P \frac{e^{-\lambda_k^p} (\lambda_k^p)^{I_k^p}}{(I_k^p)!} \quad (3.32)$$

with the expected intensity defined as

$$\lambda_k^p = G \cdot F_{\text{PSF}} \left(\mathbf{x}_{\mathbf{p},k}, \mathbf{x}_{\mathbf{s},k}^p \right) + N_{\text{bgd}}, \quad (3.33)$$

where F_{PSF} is the point spread function (PSF) of the microscope. In the determination of the expected intensity (3.33) we also include two parameters which govern the signal to noise ratio. Specifically, we assume the intensity of the light emitted by the particle is controlled by the multiplicative gain G ; this value is determined by several factors including the intensity of the excitation source and material properties of the fluorophore. In addition, we assume the existence of an additive, spatially-uniform background noise with constant intensity N_{bgd} ; this value is determined by the particle's environment and includes the existence of nearby fluorescent particles as well as autofluorescence generated by the surrounding structures and media.

Obtaining a perfectly accurate model for the measurement process is often unrealistic if not impossible. Although the PSF may be represented by one of several models of varying degrees of accuracy and complexity, knowledge of the gain G or the background noise N_{bgd} may never be known with certainty. Consequently, they should be estimated.

Unfortunately, evaluation of (3.12) with respect to G or N_{bgd} does not yield an analytical solution. Taking the derivative of $\hat{Q}(\theta, \hat{\theta}_e)$ with respect to G and with N_{bgd} fixed we obtain the maximizing condition

$$\sum_{k=1}^N \sum_{i=1}^M \sum_{p=1}^P w_{k|N,e}^i F_{k,e}^{i,p} \left(\frac{I_k^p}{\hat{G}_{e+1} F_{k,e}^{i,p} + N_{\text{bgd}}} - 1 \right) = 0 \quad (3.34)$$

for \hat{G}_{e+1} ; here, $F_{k,e}^{i,p}$ is defined as

$$F_{k,e}^{i,p} = F_{\text{PSF}}(\mathbf{x}_{k|N,e}^i, \mathbf{x}_{\mathbf{s},k}^p). \quad (3.35)$$

Similarly, evaluating the derivative of $\hat{Q}(\theta, \hat{\theta}_e)$ with respect to N_{bgd} and with G fixed we obtain the maximizing condition

$$\sum_{k=1}^N \sum_{i=1}^M \sum_{p=1}^P w_{k|N,e}^i \left(\frac{I_k^p}{G F_{k,e}^{i,p} + \hat{N}_{\text{bgd},e+1}} - 1 \right) = 0 \quad (3.36)$$

for $\hat{N}_{\text{bgd},e+1}$ and with $F_{k,e}^{i,p}$ defined in (3.35). Both of these equations may be independently solved using any root-finding algorithm, such as the tangent-hyperbolas method (Ortega and Rheinboldt, 2000).

It is important to note that even though it is possible to simultaneously estimate both N_{bgd} and G , doing so may cause the SMC-EM algorithm to fail to converge. This is due to the fact that both parameters may not be mutually identifiable in conjunction with other unknown parameters. In other words, with a finite record of measurements it may not be possible to determine whether measurement fluctuations are due to an increased level of background noise or particle motion (which is dependent on motion model), and if there are too many degrees of freedom then the parameters may not be unique. One potentially remedy for this problem is to estimate N_{bgd} experimentally by acquiring representative images of background; then, G may be estimated using SMC-EM in the context of the experimentally measured N_{bgd} .

3.4 Demonstration: Widefield Fluorescence

In this section, we discuss four numerical demonstrations that showcase the capabilities of the SMC-EM algorithm within a widefield imaging context. The four demonstrations rely on three sets of data, each consisting of multiple trials with each

trial an image sequence of a single particle undergoing motion according to one of the models introduced in the previous section. The first data set is a two-dimensional isotropic diffusion, the second is a three-dimensional isotropic diffusion with axial confinement, and the third is a three-dimensional tether. The simulated experimental setup is a wide-field imaging scenario using a Debye diffraction integral satisfying the sine condition, in all three data sets.

The three data sets are used throughout four separate demonstrations. The first data set considers the two-dimensional diffusion and attempts to estimate, under the assumption of anisotropy, the two diffusion coefficients. To ground the results from the SMC-EM algorithm, we compare them to a conventional localize-then-estimate approach using Gaussian fit (GF) and the ML estimator developed in (Michalet and Berglund, 2012). The second data set considers the three-dimensional axially-confined isotropic diffusion and estimates each diffusion coefficient in addition to the confinement length. The third data set considers the three-dimensional isotropic tether and estimates the stiffness coefficient in addition to the diffusion coefficient. The three aforementioned demonstrations assume precise knowledge of the PSF. This is, however, often not the case in most settings and thus in the fourth demonstration we show that the SMC-EM algorithm is capable of estimating PSF parameters as well. We revisit the three-dimensional tether and estimate the peak intensity of the PSF in addition to the same parameters as before. The specific parameter values for each of these demonstrations, such as diffusion coefficients, are defined in Table 3.1.

3.4.1 Generation of Ground-Truth Data

For each of the three models, we generated 40 data sets, each comprised of 100 images. Specifically, the first set of images was generated from a two-dimensional isotropic diffusion model, the second set of images was generated from the axially confined diffusion model, and the third set of images was generated from the elastic tether

Symbol	Parameter	Value
A	Stiffness Coefficient	1.0 s^{-1}
D	Diffusion Coefficient	$0.01 \text{ } \mu\text{m}^2/\text{s}$
E	Number of SMC-EM Iterations	10 iterations
G	Peak Intensity	100 counts
K	Number of Sequences	40 sequences
L	Length of Channel	500 nm
M	Number of SMC Point Estimates	125
n	Refraction Index	1.33
N	Sequence Length	100 images
N_{bgd}	Background Noise	10 counts
N_{sub}	Subsamples per Image	100 subsamples
NA	Numerical Aperture	1.2
P	Number of Pixels	25 pixels
$\Delta x, \Delta y$	Effective Pixel Length	100 nm
δt	Shutter Period	10 ms
Δt	Imaging Period	100 ms
λ	Emission Wavelength	540 nm

Table 3.1: Parameter values used in the generation of ground-truth data and for each of the four widefield imaging demonstrations.

model. The observation models were identical for all image sequences. The number of images N was chosen with regard to the imaging time $\Delta t = 100 \text{ ms}$ (i.e. 10 frames per second), yielding a total duration of 10 s for each sequence. In practice, $N\Delta t$ is selected according to the hardware’s imaging capabilities, the fluorophore’s emission capacity, and the time scale of the particle’s motion; the values chosen in this work were inspired by a recent competition (Chenouard et al., 2014) as well as a brief survey of the literature.

To generate each sequence of images, independent trajectories consisting of $N \times N_{\text{sub}}$ positions were generated from one of the three aforementioned motion models; here, $N_{\text{sub}} = 100$ represents a subsampling factor with each position in the trajectory spaced $\delta t = \Delta t/N_{\text{sub}}$ seconds apart, where $\Delta t = 100 \text{ ms}$ is the imaging period. In this work, N_{sub} was chosen large enough so that the motion between subimages was

negligible; specifically, the value was selected to ensure that the probability that a particle following an isotropic three-dimensional diffusion deviated more than 25 nm between each subimage was less than 0.2 %.

From these trajectories, images were generated using the Poisson shot noise model with the PSF defined as

$$F_{\text{PSF}}\left(\mathbf{x}_{\mathbf{p},k}, \mathbf{x}_{\mathbf{s},k}^p\right) = \int_{\left(x_{s,k}^p - \frac{\Delta x}{2}\right)}^{\left(x_{s,k}^p + \frac{\Delta x}{2}\right)} \int_{\left(y_{s,k}^p - \frac{\Delta y}{2}\right)}^{\left(y_{s,k}^p + \frac{\Delta y}{2}\right)} F_{\text{WF}}\left(x_{p,k} - \xi', y_{p,k} - \xi'', z_{p,k}\right) d\xi' d\xi'', \quad (3.37)$$

with

$$F_{\text{WF}}(x, y, z) = \left| C \int_0^\alpha \sqrt{\cos \theta} J_0\left(\kappa \sin \theta \sqrt{x^2 + y^2}\right) \exp(-i\kappa z \cos \theta) \sin \theta d\theta \right|^2, \quad (3.38)$$

where C is a complex constant chosen so that $F_{\text{WF}}(0, 0, 0) = (\Delta x \Delta y)^{-1}$, $J_0(\cdot)$ is a zeroth-order Bessel function of the first kind, $\kappa \triangleq 2\pi n/\lambda$ is the wavenumber of the emitted light, and $\alpha \triangleq \sin^{-1}(\text{NA}/n)$ is the maximum semiangle of the objective lens. This PSF model, which is based on the Debye diffraction integral, is well-suited for approximating the near-focus non-paraxial distribution of light and is valid for high-NA objective lenses (Gu, 2000). The parameters describing the PSF were set to $\text{NA} = 1.2$, $\lambda = 540$ nm, and $n = 1.33$, which are common values that one may find in an experimental setting. In addition, we assumed the effective pixel width (after magnification) was $\Delta x = \Delta y = 100$ nm.

Realistically, an image of the particle is formed by accumulating photons during an exposure period. To replicate this effect, we assumed the camera accumulated photons continuously during the first $\delta t = 10$ ms seconds of each imaging period $\Delta t = 100$ ms by averaging the first ten consecutive images in the period and ignoring the rest. As noted above, δt was chosen sufficiently small so that the motion of particle during photon accumulation was negligible while remaining large enough to

ensure an adequate number of photons was collected.

The particle was set to have a peak fluorescence of $G = 100$ counts over the entire exposure time δt . The background noise was assumed to be uniform throughout the image with a fixed number of $N_{\text{bgd}} = 10$ counts during the exposure period. For simplicity we assumed there was no blinking or bleaching during the accumulation period.

In practice, when one acquires images in real experimental situations, many particles may be present and segmentation and linking among frames must be performed. The choice of method for this step affects the quality of the final localization and parameter estimation. To use the algorithm presented in this work, however, *any* segmentation and linking technique may be applied to generate a sequence of pixel arrays (see, e.g. (Chenouard et al., 2014)). To abstract the impact of segmentation from the behavior of the SMC-EM algorithm, “perfect segmentation” was assumed in the trials presented here. Thus, each image was approximately centered in each frame by an oracle, and only one particle was present throughout the image generation process. As will be discussed later, the computational complexity of the proposed algorithm increases with the number of pixels observed per frame; consequently, the user must be judicious as to how large the image should be to ensure that enough information regarding the particle is present without including too many “empty” pixels. For the image sequences described in this work, each image contained $P = 25$ pixels arranged into a square $\sqrt{P} \times \sqrt{P}$ array; the effective length of each segmented image was $0.5 \mu\text{m}$ which is approximately twice the full-width at half-maximum value when the particle is in focus.

Since the localization resolution depends on the total number of informative photons acquired during the imaging process, one possible metric for comparing the three data sets is the average number of photons acquired per (segmented) frame. The av-

average number of photons was 756 per frame for the first data set, 737 per frame for the second data set, and 721 per frame; recall that each segmented frame consisted of $P = 25$ pixels. Thus, the average number of photons per frame is nearly equivalent for each of the demonstrations and one may expect similar localization resolution.

3.4.2 Algorithm Implementation

Recall that the SMC-EM algorithm iterates between two distinct steps. On the first iteration of the algorithm, the expectation step yields an evaluation of (3.10) through application of SMC-based filtering and smoothing techniques to the acquired data (i.e. images) with respect to the motion (3.2) and observation (3.3) models and an a priori parameter estimate $\hat{\theta}_0$. The subsequent maximization step yields an improved estimate $\hat{\theta}_1$ through the evaluation of (3.12). The expectation step is then executed again with respect to the new estimate $\hat{\theta}_1$, and the maximization step follows afterward yielding $\hat{\theta}_2$. This process continues until a termination criterion is satisfied.

For each of the demonstrations presented in this section, the SMC-EM algorithm was terminated after a fixed number $E = 10$ of iterations. The number of iterations was chosen large enough so that the parameters approximately converged to a fixed value. We note that if the user is particularly concerned about the amount of computational time required to estimate the parameters then optimal change point methods, such as those presented in (Poor and Hadjiliadis, 2008), could be considered.

The number of Monte Carlo estimates M was chosen to be 125 for each of the four demonstrations. In general, proper selection of this parameter requires some degree of experimentation. Ideally, to minimize the Monte Carlo variability the parameter M should be large; however, as further discussed in the appendix the SMC-EM algorithm implemented in this work has a computational complexity that scales quadratically with M . Thus, using a large number of Monte Carlo estimates may significantly

impede throughput. One way of determining an appropriate value for M is to process the data using an initial value and then process the data again using double the initial value. If the statistics of the resulting parameter estimates did not improve between M_0 and M_1 , then M_0 may be deemed sufficient. Otherwise, process the data again using quadruple the value and repeat the comparison. In this work, $M = 125$ was chosen because $M = 250$ did not yield an improvement in the variance of the parameter estimates in any of the demonstrations.

For all the demonstrations, the initial parameter estimates were randomly generated within one order of magnitude of their true value (aside from the confinement length L for which an upper bound was used instead). It is important to note that the SMC-EM algorithm may fail to converge if the initial parameter estimates are too far from their true values. Since the expectation step relies on a finite number of Monte Carlo estimates to generate an approximate posterior density, a severe mismatch between the data and assumed model may result in most of the Monte Carlo estimates having low (or even zero) likelihood. In the case that all the estimates have zero likelihood, the approximate posterior density becomes degenerate and the algorithm fails. The probability of this failure occurring can be reduced by using a larger number of Monte Carlo estimates or by using more efficient SMC algorithms. Alternatively, if initial parameter estimates are not known to a degree so that the SMC-EM algorithm converges, methods other than SMC-EM may be used to provide an initial estimate that can be used in the subsequent application of SMC-EM.

3.4.3 Metrics for Algorithm Performance

Recall that the output of the SMC-EM algorithm consists of two parts - the parameter estimates and the joint posterior density estimates on the position of the particle. Although assessing the quality of the estimated parameters by comparing them to their true values is straightforward, determining the performance of localization is

not. This is mostly due to the fact that the SMC-EM algorithm yields a Monte Carlo approximation of the full joint posterior density of the particle's position over time rather than just a point estimate. This provides significantly more information than a point estimate. To assess the performance of localization in this work, we assume the most representative estimate of the particle's position at a given time is the weighted arithmetic mean over all estimates. In other words, the position estimate $(\hat{x}_{k,e}, \hat{y}_{k,e}, \hat{z}_{k,e})$ is used as a surrogate for the posterior density at time step k , where

$$\hat{x}_{k,e} \triangleq \sum_{i=1}^M w_{k|N,e}^i x_{k|N,e}^i, \quad (3.39)$$

with $\hat{y}_{k,e}$ and $\hat{z}_{k,e}$ defined similarly. Given these surrogates, the Root Mean Squared (RMS) localization error can be calculated for each image sequence.

The variability in the results presented in this section - specifically, the bias and the standard deviations in both the parameter estimates and localization errors - are primarily driven by two sources of random error. The first, experimental variability, comes from several sources, including randomness in the motion of the particle, shot and background noise in the measurement, motion blur in the data, and the finite pixel size of the detector. This variability is inherent to the experimental setting itself and is present regardless of the estimation scheme.

The second source of variability arises from the Monte Carlo nature of the SMC element of the estimation scheme. This variability scales as \sqrt{M} and thus vanishes in the limit of a large number of point estimates in the discrete representation of the densities. However, the computation time of the algorithm is driven in large part by the size of M and thus there is a trade off between error introduced by small M and the computation time needed for large M . As noted previously, the value of 125 used in these demonstrations was selected based on the observation that the standard deviations of the estimates did not diminish when doubling M to 250.

An additional source of variability includes experimental variability. For each of the following demonstrations we report sample means and sample standard deviations for both the parameter estimates and the RMS errors. As was mentioned previously, 40 independent experiments were performed for each demonstration; this value was experimentally determined to be large enough so that the experimental variability was small relative to the other sources.

We note that the fundamental limit of estimation variability for each of the fixed parameters (e.g. A , L , D , and G) is given by the Cramér-Rao lower bound (CRLB). In other words, the CRLB defines the absolute minimum variability one could obtain by estimating a set of fixed parameters using a finite number of images N , given a choice of motion and observation models but independent of the estimation algorithm used. For the case of an isotropic diffusion with diffusion coefficient D and additive Gaussian localization uncertainty with variance σ^2 , the corresponding CRLB was derived analytically in (Michalet and Berglund, 2012). In general, however, the calculation of CRLB for models that take the form of (3.2) and (3.3) are much more difficult since the exact likelihood is unknown. One approach is to condition on a latent state, as was done in the derivation of the SMC-EM algorithm, but this becomes numerically intractable for a large number of images. Recognizing this difficulty, some attempts have been made to estimate the CRLB via Monte Carlo simulations, e.g. (Spall, 2012), but there currently exists no analytical approach for the models we consider in this work.

Since most conventional approaches assume the localization uncertainty is zero-mean, additive, white, and Gaussian, a common approach is to treat the statistics of this uncertainty as a fixed parameter and, as with the motion parameters, compare localization uncertainty to the CRLB. In this case, however, the localized position of the particle is described in the SMC-EM framework by the time-dependent posterior

probability density function which takes into account the observed images. Since the CRLB is limited to *fixed parameters*, i.e. quantities that are not dependent on time and do not vary during the experiment, it is not an applicable measure for localization error in this setting. One approach that is similar to the CRLB and can handle time-varying parameters is the *posterior* Cramér-Rao lower bound (PCRLB). The PCRLB was first presented in (Trees, 1968) and later extended to the context of nonlinear filtering in (Tichavský et al., 1998). Much like the CRLB, the calculation of the PCRLB for general models of the form (3.2) and (3.3) is computationally intractable, and, although approaches have been made to numerically approximate it, e.g. (Tulsyan et al., 2013), there is no currently analytically tractable method for its calculation.

3.4.4 Demonstration No. 1: Two-Dimensional Diffusion

The goal of the first demonstration was to use the SMC-EM algorithm to estimate the diffusion coefficients and trajectory for a particle undergoing two-dimensional isotropic diffusion. For this demonstration, we analyzed the K image sequences from the first set of data that was described in Sec. 3.4.1. In addition, we compared the SMC-EM results to a conventional method of first localizing the particle in each image with a nonlinear fit to a Gaussian function and then calculating the ML estimate of the diffusion coefficients using the method proposed in (Michalet and Berglund, 2012); for brevity, we refer to this method by *GF-ML*.

The motion model was assumed to be of the form (3.14) in both x and y axes; for identification purposes, however, we assumed the diffusion was anisotropic and that the diffusion coefficients for each axis, namely D_x and D_y , needed to be identified. Moreover, the position of the particle in the z direction was assumed to be zero, its true value.

To initialize the SMC-EM algorithm for each of the image sequences, the initial

diffusion coefficient estimates, $\hat{D}_{x,0}$ and $\hat{D}_{y,0}$, were randomly generated within an order of magnitude of their true value $D = 0.01 \mu\text{m}^2/\text{s}$.

As described in the Appendix, the maximization step consisted of evaluating the parameter update equation (3.12) with respect to the motion model (3.14) to yield the parameter update equations (3.15) for both x and y axes.

For only this demonstration, we assumed

$$F_{\text{WF}}(x, y, z) = \frac{1}{\Delta x \Delta y} \exp\left(-\frac{x^2}{2\sigma_x^2} - \frac{y^2}{2\sigma_y^2}\right) \quad (3.40)$$

instead of the Debye model (3.38); in fact, it was shown in (Zhang et al., 2007) that the parameters

$$\sigma_x = \frac{\sqrt{2}\lambda}{2\pi\text{NA}}, \quad \sigma_y = \frac{\sqrt{2}\lambda}{2\pi\text{NA}}, \quad (3.41)$$

yield an optimal approximation of the Debye model (3.38) in an appropriate sense. The parameters λ and NA were assumed known with certainty, as was the background noise N_{bgd} and the z axis position of the particle (the latter of which was assumed to be zero). To clarify, the true data was generated with the Debye model (3.38) as described in Sec. 3.4.1.

The approximation (3.40) is not a requirement for use of the SMC-EM algorithm. In fact, it will be shown in the three subsequent demonstrations that the SMC-EM algorithm is not restricted to any particular PSF model and that it may incorporate those from other imaging modalities. The primary benefit of using (3.40) is that it is simple to calculate.

Recall that the true diffusion coefficient for both x and y axes was $0.01 \mu\text{m}^2/\text{s}$. After ten iterations of SMC-EM, the resulting diffusion coefficient estimates were $0.009 \pm 0.002 \mu\text{m}^2/\text{s}$ in both x and y axes; the GF-ML algorithm yielded identical results. Additionally, after ten iterations of SMC-EM, the RMS localization errors

were $0.013 \pm 0.001 \mu\text{m}$ and $0.012 \pm 0.001 \mu\text{m}$ in x and y , respectively; the GF-ML algorithm yielded $0.009 \pm 0.001 \mu\text{m}$ in both x and y axes. The resulting diffusion coefficient estimates as a function of EM iteration number are shown in Fig. 3-1 while the RMS localization errors are shown in Fig. 3-2. We note that convergence for the SMC-EM algorithm was relatively fast in this case and only needed two to three iterations to converge.

An illustration comparing the performance of the two algorithms (GF-ML and SMC-EM) on estimating the particle trajectory is given in Fig. 3-3. Although the two yielded similar parameter and localization estimates, the two methods make very different assumptions on the underlying motion and observation models. In particular, the GF-ML algorithm assumes there is no information to be gained by considering the time-history of the location of the particle during the localization step. In addition, the SMC-EM algorithm is not necessarily restricted to any motion or imaging modality so long as it can be represented in the form (3.2) and (3.3); the GF-ML algorithm is only applicable to a diffusing particle with a PSF that is approximately Gaussian and localization uncertainty that is normally distributed. Moreover, the SMC-EM algorithm yields a full, albeit approximate, probability distribution of the particle position given the acquired images, whereas the GF-ML provides Gaussian statistics.

It is important to note that blur during the exposure period may significantly affect the accuracy of both localization and estimation, especially if there is no attempt to compensate for it. To demonstrate its effect, we repeated Demonstration No. 1 with $\delta t = \Delta t = 100 \text{ ms}$ (i.e. full exposure during the imaging period). The SMC-EM method resulted in diffusion coefficient estimates of $0.007 \pm 0.001 \mu\text{m/s}$ and RMS errors of $0.026 \pm 0.002 \mu\text{m}$ for both x and y axes. The GF-ML method, however, resulted in $0.010 \pm 0.002 \mu\text{m/s}$ and RMS errors of $0.025 \pm 0.002 \mu\text{m}$ for both x and

y axes. We note that although the localization errors were nearly equivalent for both methods, the GF-ML method resulted in a more accurate diffusion coefficient estimate. This is because the parameter estimation algorithm used in the GF-ML method can compensate for the expected blur that occurs during the imaging process and that corrupts the position estimate (details on how this is done can be found in (Michalet and Berglund, 2012)).

Both the GF-ML and SMC-EM algorithms possess unique features and have their time and place for proper use. For example, when long exposure times are required (and blur contributes significantly to the localization uncertainty), the GF-ML algorithm may yield more accurate estimates. In contrast, when the experimentalist observes significant deviation from a standard diffusion and requires a more complicated motion and/or observation models, the SMC-EM algorithm may yield superior results.

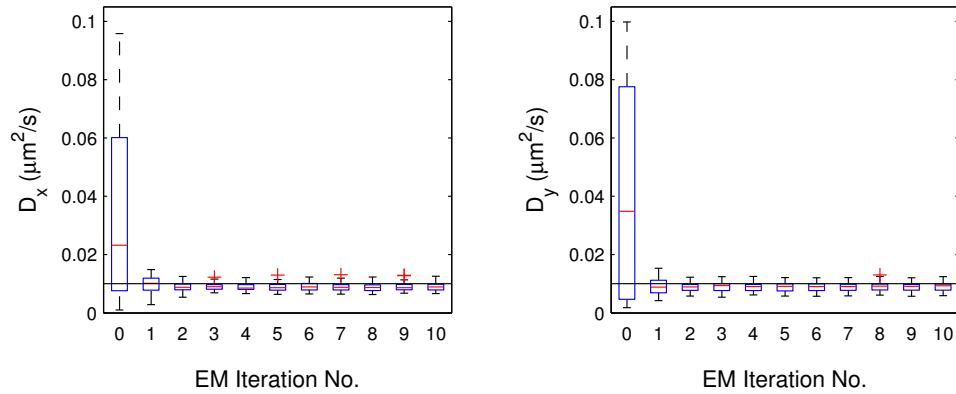


Figure 3.1: Box plots of the estimated diffusion coefficients as a function of the number of iterations of the SMC-EM algorithm for the first demonstration (2D diffusion, Sec. 3.4.4). The edges of the box represent the first and third quartiles, the red line is the median, the vertical dashed line indicates the bounds for data within 1.5 times the interquartile range, and the red + symbols are data points outside this range. The true values of the diffusion parameters, indicated by the solid black lines, were $D_x = D_y = 0.01 \mu\text{m}^2/\text{s}$.

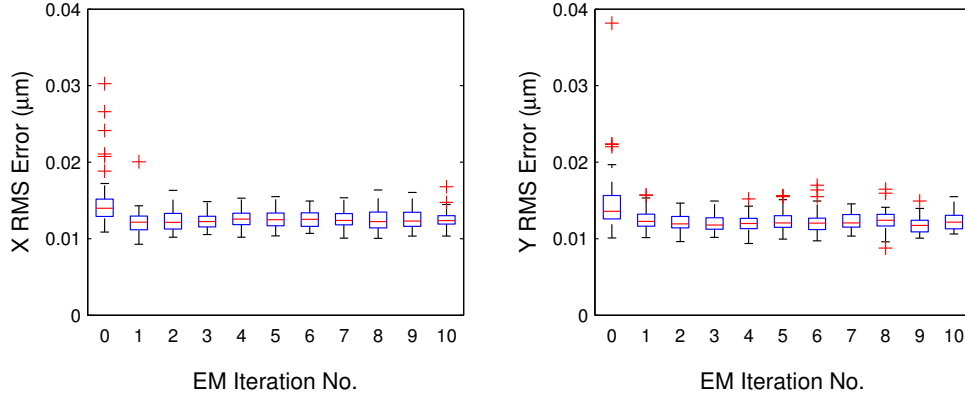


Figure 3.2: Box plots of the root mean square (RMS) localization error as a function of the number of iterations of the SMC-EM algorithm for the first demonstration (2D diffusion, Sec. 3.4.4). The edges of the box represent the first and third quartiles, the red line is the median, the vertical dashed line indicates the bounds for data within 1.5 times the interquartile range, and the red + symbols are data points outside this range.

3.4.5 Demonstration No. 2: Axially-Confining Diffusion

The second demonstration was an extension of the first; specifically, we considered an isotropic diffusion where the axial motion was confined to the interval $[-L/2, L/2]$. For both the expectation and maximization steps, the motion models in the x and y axes were assumed to be of the form of (3.14) whereas the motion model for the z axis was assumed to be of the form of (3.20). For the purposes of estimation, the diffusion was assumed to be independent and anisotropic in all three axes. The SMC-EM algorithm was used to estimate the four motion parameters, namely the confinement length L and the three diffusion coefficients D_x , D_y , and D_z .

The expectation step for this demonstration was performed similarly to the first. However, unlike the previous demonstration which used a Gaussian approximation (3.40) for its PSF model, we chose to implement the full Debye model (3.38) instead. This choice was made for two reasons; first, because no accurate Gaussian approximation exists for three-dimensional widefield PSFs (Zhang et al., 2007), and second, to

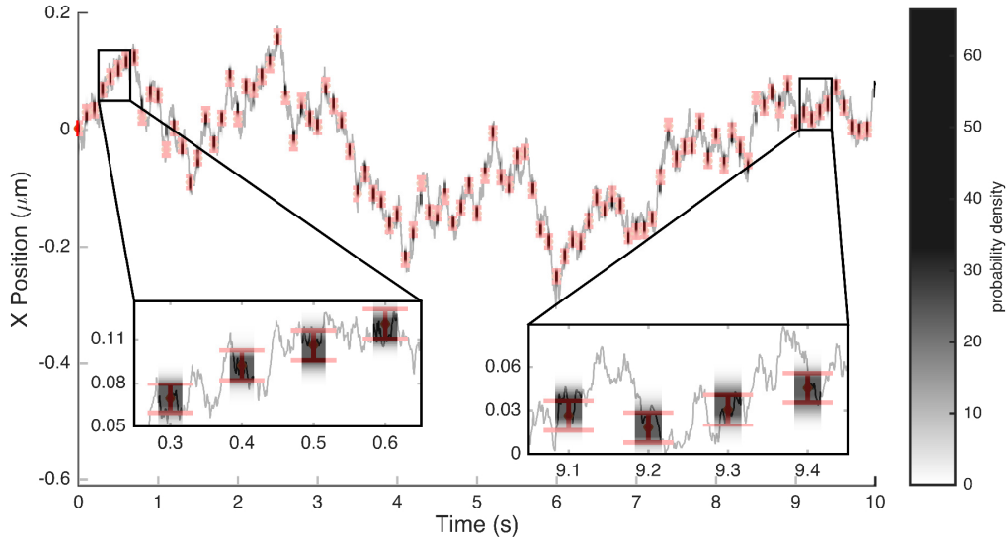


Figure 3-3: This figure illustrates a typical trajectory from the two-dimensional diffusion in the first demonstration (2D diffusion, Sec. 3.4.4); only the x axis results are shown; y axis results were similar in appearance. The random walk shown in gray represents the true position of the particle over time. The red dots indicate the Gaussian fit (GF) estimates and the red error bars are the 3σ uncertainties of these estimates as determined via maximum likelihood estimation (Michalet and Berglund, 2012). The shaded regions represent the approximate posterior probability densities for the particle positions after ten iterations of the SMC-EM algorithm.

highlight the fact that complicated PSF models can be incorporated into the SMC-EM algorithm. We assumed all PSF parameters, as well as the gain parameter G and the background noise N_{bgd} , were known with certainty. We note that SMC-EM is capable of also estimating parameters describing the observation model; this is highlighted in the fourth demonstration.

The maximization step was also performed in a similar manner to the first demonstration. In particular, both the x and y diffusion coefficient estimates are of the form (3.15). In contrast, the z axis diffusion coefficient and confinement length estimates were calculated according to the procedures described in Sec. 3.3.3.

Similar to the first demonstration, the three initial diffusion coefficient estimates

were randomly selected from within an order of magnitude of their true values $D = 0.01 \mu\text{m}^2/\text{s}$. The initial length estimate \hat{L} was set to $1.0 \mu\text{m}$ for every image sequence. The true value was 500 nm .

After ten iterations of SMC-EM, the resulting diffusion coefficient estimates were $0.010 \pm 0.001 \mu\text{m}^2/\text{s}$, $0.009 \pm 0.001 \mu\text{m}^2/\text{s}$, and $0.009 \pm 0.004 \mu\text{m}^2/\text{s}$ in the x , y , and z axes, respectively, and the confinement length estimate was $0.53 \pm 0.05 \mu\text{m}$. The RMS localization errors were $0.013 \pm 0.001 \mu\text{m}$ in both in x and y and $0.14 \pm 0.05 \mu\text{m}$ in z . The resulting parameter estimates and RMS localization errors as a function of EM iteration number are shown in Fig. 3-4 and 3-5.

Note that the error in localization along the z axis was an order of magnitude worse than in x and y ; further, as seen in Fig. 3-5, this localization error did not show significant improvement over the initial condition. This reflects the fact that there is a large amount of localization uncertainty in z since the two-dimensional image of the symmetric three-dimensional PSF provides only limited information of the particle’s axial position. This is due in part to the fact that the implemented PSF (3.38) has an effective axial slope that is much smaller than the longitudinal slope. Perhaps even more important, however, is that the axial symmetry of the PSF causes “crossing” errors about the particle center. Due to the symmetry of the PSF, the measurements cannot distinguish between positions above the focal plane and positions below the focal plane and as a result, trajectories that are mirror reflected through the focal plane are equally likely. In general, in the limit of very large M , the SMC approximation to the posterior density can maintain a bi-modal distribution reflecting these two possibilities. Given a finite (and small) M , however, the estimator tends to lock the distribution onto one side of focal plane, chosen essentially at random. (This effect is essentially the same as what is known in the SMC literature as *sample impoverishment*. See, e.g., (Cappe et al., 2007).) Unlike point

estimates based on a single frame, however, the SMC-EM approach uses the entire set of frames in conjunction with the motion model to produce position estimates. As a result the expected location of the particle will not hop from one side of the plane to the other. This is illustrated in Fig. 3·6 which shows a typical z trajectory and the posterior density estimates; the figure shows that the posterior sometimes follows the true trajectory and sometimes is reflected through the focal plane at zero. In either case, however, the dynamics are well-captured and as a result the estimates of the z diffusion coefficient and confinement length were still both quite accurate. The uncertainty did affect the convergence rate, however. As seen in Fig. 3·4, D_z took nearly all ten iterations of SMC-EM to converge while D_x and D_y both converged within two iterations.

This localization problem can be remedied in the experimental setting by using an asymmetric PSF, such as those induced by astigmatism; since the SMC-EM algorithm makes no assumption on the form of the PSF, such experimental settings can still be analyzed with the SMC-EM method. Alternatively, one could recognize that the PSF does not yield information about the sign of the z position relative to the focal plane and use an estimator that gives only the distance from that plane. For example, one could replace the arithmetic mean (3.39) with the absolute value of the arithmetic mean. Doing so yields an RMS error (relative to the absolute value of the true z position) of $0.048 \pm 0.007 \mu\text{m}$, a significant improvement over the $0.14 \mu\text{m}$ error for the signed case; these values are indicated in Fig. 3·5 in the right-most figure by boxes in blue.

3.4.6 Demonstration No. 3: Three-Dimensional Elastic Tethering

For the third demonstration, we considered the case where the fluorescent particle was elastically tethered to a fixed point. We assumed that, in all three axes, the motion was derived from the Ornstein-Uhlenbeck model (3.22). Although the motion

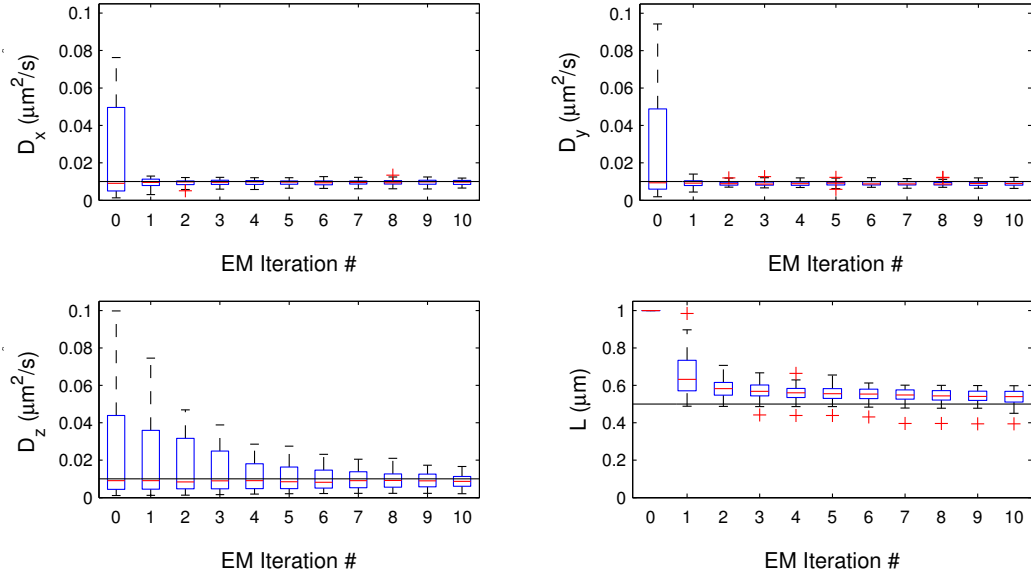


Figure 3.4: Box plots of the estimated parameters as a function of the number of iterations of the SMC-EM algorithm for the second demonstration (confined diffusion, Sec. 3.4.5). In this case, the z position of the diffusing particle was confined to the interval $[-L/2, L/2]$; the diffusion coefficients D_x, D_y, D_z and the confinement length L were assumed unknown. The edges of the box represent the first and third quartiles, the red line is the median, the vertical dashed line indicates the bounds for data within 1.5 times the interquartile range, and the red + symbols are data points outside this range. The true values, indicated by the solid black lines, were $D_x = D_y = D_z = 0.01 \mu\text{m}^2/\text{s}$ and $L = 0.5 \mu\text{m}$.

in each axis was assumed independent, each axes' motion depended on the two to-be-estimated parameters, A and D .

The implementation of the SMC-EM algorithm for this demonstration was nearly identical to that of the second demonstration. The observation model was identical to the second demonstration; that is, the full Debye model (3.38) was used and all of its parameters were assumed known with certainty. The maximization step used the formulae (3.25) and (3.28) to update the parameter estimates A and D , respectively. The initial parameter estimates \hat{A}_0 and \hat{D}_0 were randomly generated within an order of magnitude of their true values, 1.0 s^{-1} and $0.01 \mu\text{m}^2/\text{s}$, respectively.

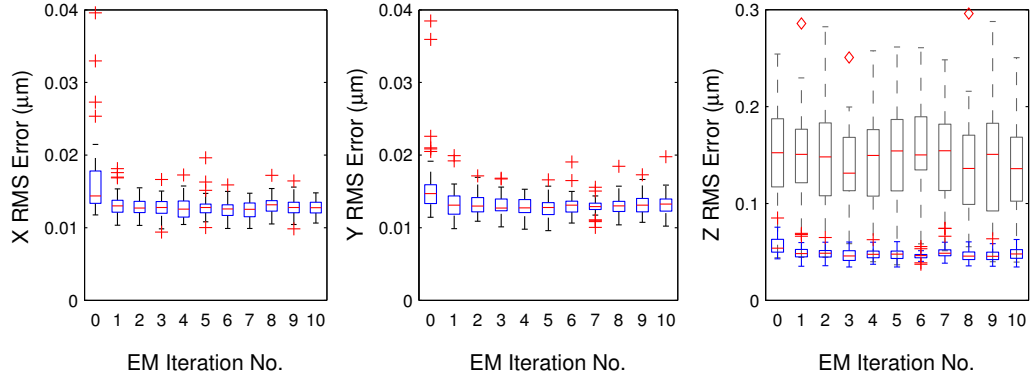


Figure 3-5: Box plots of the root mean square (RMS) localization error as a function of the number of iterations of the EM algorithm for the second demonstration (confined diffusion, Sec. 3.4.5). The edges of the box represent the first and third quartiles, the red line is the median, the vertical dashed line indicates the bounds for data within 1.5 times the interquartile range, and the red + symbols are data points outside this range. The raw RMS errors for z are indicated in the right-most figure as gray boxes (with outliers denoted by red diamonds), whereas the RMS errors for the absolute value of z are indicated by blue boxes.

After ten iterations of SMC-EM, the resulting stiffness coefficient was $1.0 \pm 0.3 \text{ s}^{-1}$ and the resulting diffusion coefficient was $0.009 \pm 0.001 \text{ } \mu\text{m}^2/\text{s}$. The resulting RMS localization errors were $0.012 \pm 0.001 \text{ } \mu\text{m}$ in both x and y and $0.12 \pm 0.05 \text{ } \mu\text{m}$ in z . The resulting parameter estimates and RMS localization errors as a function of EM iteration number are shown in Figs. 3-7 and 3-8.

The results from the third demonstration were similar in character to that of the second. In particular, we once again see significant axial localization uncertainty due to properties of the PSF, though using the absolute value as before yielded a much better error of $0.046 \pm 0.006 \text{ } \mu\text{m}$. In addition, the estimated parameters require four or five iterations to converge instead of the expected two or three. This slower convergence rate is due to the parameters' dependence on the z position; had we decoupled x and y from z and used four parameters instead, i.e. A_{xy} , A_z , D_{xy} , D_z , the convergence rates would have been faster in x and y .

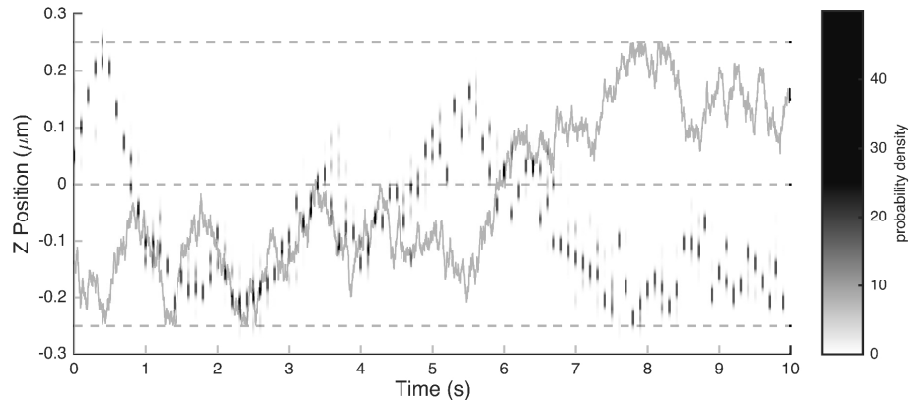


Figure 3-6: A typical z trajectory from the second demonstration (confined diffusion, Sec. 3.4.5). Here, the true trajectory is shown in grey and the posterior density estimates after ten iterations of the SMC-EM algorithm are shown with values according to the color bar. Note that estimates occur only every 100 ms while the true trajectory is defined (essentially) continuously. The dashed lines indicate the focal plane (at $z = 0$) and the bounds of the channel ($z = \pm 0.25 \mu\text{m}$). From this figure, it is clear that the PSF's symmetry about the focal point at $z = 0$ creates potential localization error in which the trajectory is essentially reflected through the focal plane (for example, from time 0 s to approximately 1 s and again from approximately 4.5 s through the end at 10 s). We note that this phenomenon is solely due to the PSF's symmetry about the focal point and is exhibited by all localization algorithms; PSFs that are asymmetric will not produce this behavior. Use of the motion model and the entire set of data prevent the estimates from randomly changing their sign relative to the focal plane and thus the motion model parameters can still be effectively estimated.

3.4.7 Demonstration No. 4: Elastic Tethering with Unknown PSF

Lastly, the fourth demonstration used exactly the same data as in the third demonstration but estimated one additional parameter. Unlike the third demonstration which assumed complete knowledge of the observation model, the fourth demonstration assumed that the gain G must be estimated. Relative to the third demonstration, the only major algorithmic change this requires is the additional calculation of the estimate of G during the maximization step; the parameter estimate equation for G

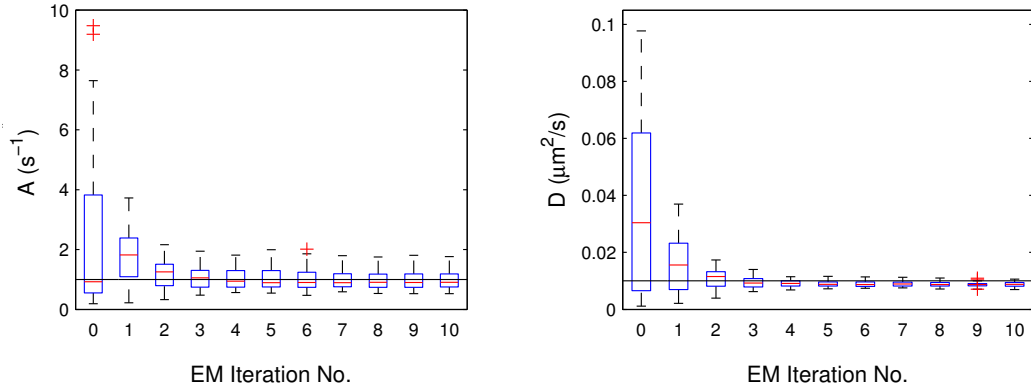


Figure 3-7: Box plots of the estimated parameters as a function of the number of iterations of the SMC-EM algorithm for the third demonstration (3D tether, Sec. 3.4.6). In this case, the particle was assumed to be elastically tethered to a known location; the stiffness coefficient A and the diffusion coefficient D were assumed unknown. The edges of the box represent the first and third quartiles, the red line is the median, the vertical dashed line indicates the bounds for data within 1.5 times the interquartile range, and the red + symbols are data points outside this range. The true values, indicated by the solid black lines, were $A = 1.0 \text{ s}^{-1}$ and $D = 0.01 \text{ } \mu\text{m}^2/\text{s}$.

is shown in (3.34). The initial estimate for G was randomly generated within 20% of the true value. In practice the initial estimate would be guided by the peak values in the data.

The true diffusion coefficient was $0.01 \text{ } \mu\text{m}^2/\text{s}$, the true stiffness coefficient was 1.0 s^{-1} , and the true gain was 100 counts. After ten iterations of SMC-EM, the resulting estimated diffusion coefficient was $0.009 \pm 0.001 \text{ } \mu\text{m}^2/\text{s}$, the resulting stiffness coefficient was $1.2 \pm 0.3 \text{ s}^{-1}$, and the resulting gain was 89 ± 1 counts. The resulting RMS localization errors were $0.012 \pm 0.001 \text{ } \mu\text{m}$ in both x and y and $0.10 \pm 0.03 \text{ } \mu\text{m}$ in z . The error for the absolute value of z was $0.047 \pm 0.006 \text{ } \mu\text{m}$. The parameter estimates and RMS localization errors as a function of EM iteration number are shown in Figs. 3-9 and 3-10.

Convergence for the fourth demonstration was very similar to the third. In particular, we see that the A , D , and G parameters all required four or five iterations to

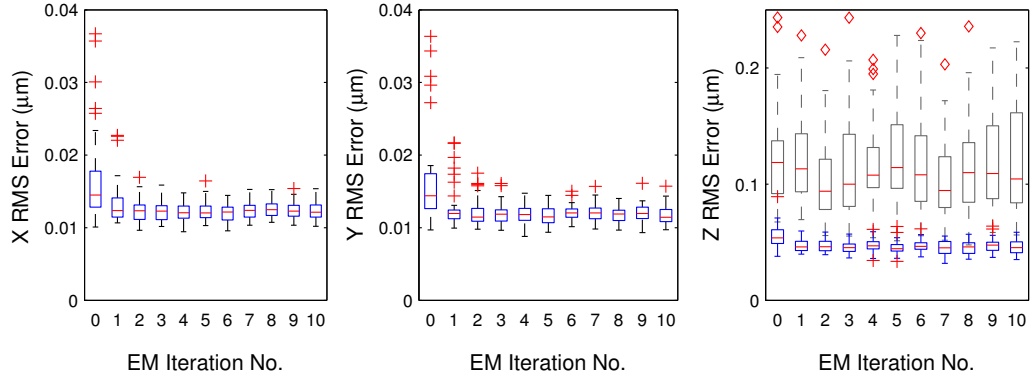


Figure 3-8: Box plots of the root mean square (RMS) localization error as a function of the number of iterations of the SMC-EM algorithm for the third demonstration (3D tether, Sec. 3.4.6). The edges of the box represent the first and third quartiles, the red line is the median, the vertical dashed line indicates the bounds for data within 1.5 times the interquartile range, and the red + symbols are data points outside this range. The raw RMS errors for z are indicated in the right-most figure as gray boxes (with outliers denoted by red diamonds), whereas the RMS errors for the absolute value of z are indicated by blue boxes.

converge. As in the third demonstration, the estimate of D is very close to the true value. The estimate of A shows a larger error than previously and perhaps some bias (though the true parameter value is within one standard deviation) while there is a clear bias in the estimate of G . These errors likely arise from two sources. The first is again the axial uncertainty in the PSF. Since the intensity gain G is affected by the axial position of the particle, errors in that localization propagate into the gain estimate. The second is the fact that the same amount of data is being used to estimate a larger number of parameters; because the ML estimators are only *asymptotically* efficient, a larger number of images would reduce variance and bias.

3.5 Summary

This chapter presented an inference method which solves some of the problems with the common inference paradigm for fluorescent particle tracking. The method com-

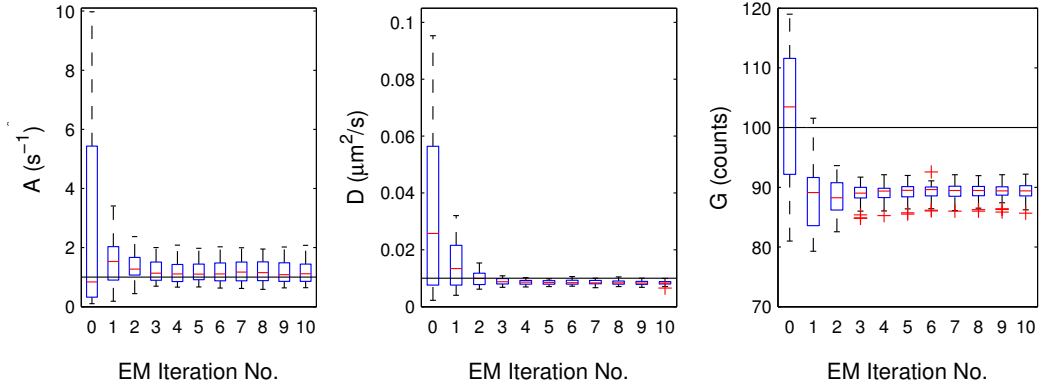


Figure 3-9: Box plots of the estimated parameters as a function of the number of iterations of the SMC-EM algorithm for the fourth demonstration (3D tether with unknown G , Sec. 3.4.7). In this case, the particle was assumed to be elastically tethered to a known location; the stiffness coefficient A , the diffusion coefficient D , and the peak fluorescence intensity G were assumed unknown. The edges of the box represent the first and third quartiles, the red line is the median, the vertical dashed line indicates the bounds for data within 1.5 times the interquartile range, and the red + symbols are data points outside this range. The true values, indicated by the solid black lines, were $A = 1.0 \text{ s}^{-1}$, $D = 0.01 \text{ } \mu\text{m}^2/\text{s}$, and $G = 100 \text{ counts}$.

combines the Expectation Maximization algorithm with Sequential Monte Carlo methods to simultaneously localize the particle’s location as well as infer model parameters governing the behavior of the particle and the measurement process. Specifically, the algorithm produces an approximation of the posterior probability density of the particle’s location at a given time; it also produces approximate Maximum Likelihood (ML) estimates for potentially nonlinear motion and observation models. The method can be applied in a wide variety of microscopy-related scenarios and we have presented four demonstrations pertaining to the widefield imaging case. In particular, we estimated the parameters for three different motion models (free, confined, and tethered diffusions) as well as the multiplicative gain for a Poisson shot noise observation model. The method is a flexible approach which, despite being unable to account for intraframe motion blur, exceeds the capabilities of the common paradigm.

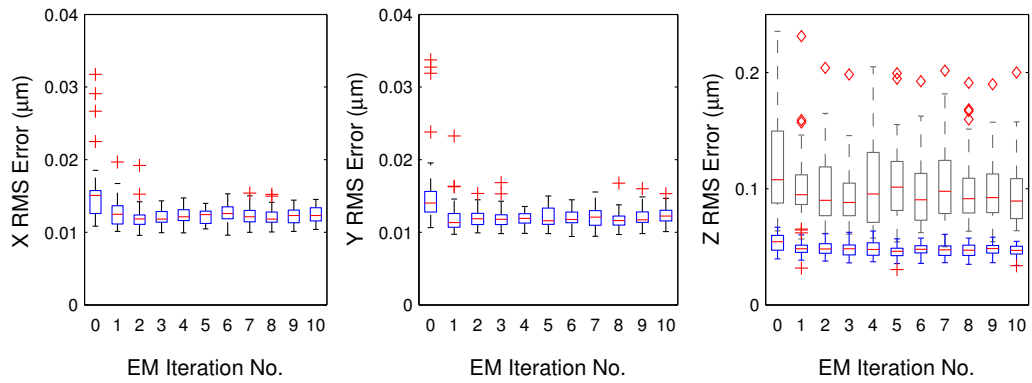


Figure 3-10: Box plots of the root mean square (RMS) localization error as a function of the number of iterations of the SMC-EM algorithm for the fourth demonstration (3D tether with unknown G , Sec. 3.4.7). The edges of the box represent the first and third quartiles, the red line is the median, the vertical dashed line indicates the bounds for data within 1.5 times the interquartile range, and the red + symbols are data points outside this range. The raw RMS errors for z are indicated in the right-most figure as gray boxes (with outliers denoted by red diamonds), whereas the RMS errors for the absolute value of z are indicated by blue boxes.

Chapter 4

Tracking a Quantum Dot within a Hydrogel

In Chapter 2, we developed a novel method for tracking a single fluorescent particle in three dimensions within a confocal microscope. The method is unique in the fact that, despite being an active tracking method, it requires no online localization to follow the particle. In addition, it produces smooth trajectories unlike many other active tracking methods. The method operates by adjusting the position of the focal volume relative to the fluorescent source so that it converges to a region near the maximum of the emitted light; in fact, the existence of a maximum is the only assumption the algorithm makes to tracking the particle.

In this chapter, we demonstrate the effectiveness of this method by tracking a quantum dot (QD) as it diffuses within a hydrogel. We begin by describing the confocal microscope hardware as well as the algorithm implementation within a real-time controller. We then describe the preparation process for the hydrogel and how tracking was performed. Since the tracking algorithm does not explicitly localize the particle, the experiment's output is a time series of three dimensional position each with an associated measured intensity; thus, the location of the particle is to be estimated offline. As such, we employ the SMC-EM method described in Chapter 3 to estimate the particle's location as well as its diffusion coefficient and speed.

4.1 Confocal Microscope Setup

The instrument used in this work consisted of an inverted epifluorescent microscope (Axiovert 200M, Zeiss) augmented with confocal optics. A 488 nm diode laser (FiberTec II, Blue Sky Research) was expanded and collimated to overfill the back aperture of the objective lens (C-Apochromat 63x/1.20 W Corr M27, Carl Zeiss). The collimated beam, after being reflected off the dichroic filter (HW625/30m, Chroma), was focused onto the sample by the objective lens. A three-axis piezoelectric nanopositioner (Nano-PDQ, Mad City Labs) with a $50 \times 50 \times 25 \mu\text{m}$ range of motion held the sample above the objective lens. The generated fluorescence was imaged by the objective and passed through the dichroic filter and tube lens where it was focused onto a $75 \mu\text{m}$ -diameter pinhole (P75S, Thorlabs) and avalanche photodiode (SPCM-AQR-14, Perkin Elmer). For diagnostics, a pellicle beam splitter (CM1-BP133, Thorlabs) split approximately one-third of the fluorescence onto a CCD camera (EXi Aqua, QImaging); the CCD was used for finding regions of interest and was not used during tracking. The tracking algorithm (2.5) was discretized in time using an Euler method and was implemented using fixed-point arithmetic on the field programmable gate array (FPGA, Spartan 6, Xilinx) of a real-time embedded controller (CompactRIO 9076, National Instruments); the real-time controller recorded the digital photodiode pulses and calculated commands for the nanopositioner according to the tracking algorithm. A picture of the instrument is shown in Fig. 4-1 and a block-diagram of the instrument is shown in Fig 4-2.

4.2 Characterization of Confocal PSF

Although the tracking algorithm described in Chapter 2 requires no specific knowledge of the point spread function (PSF) aside from it possessing a global maximum, localizing the particle given the experimental data using the SMC-EM algorithm de-

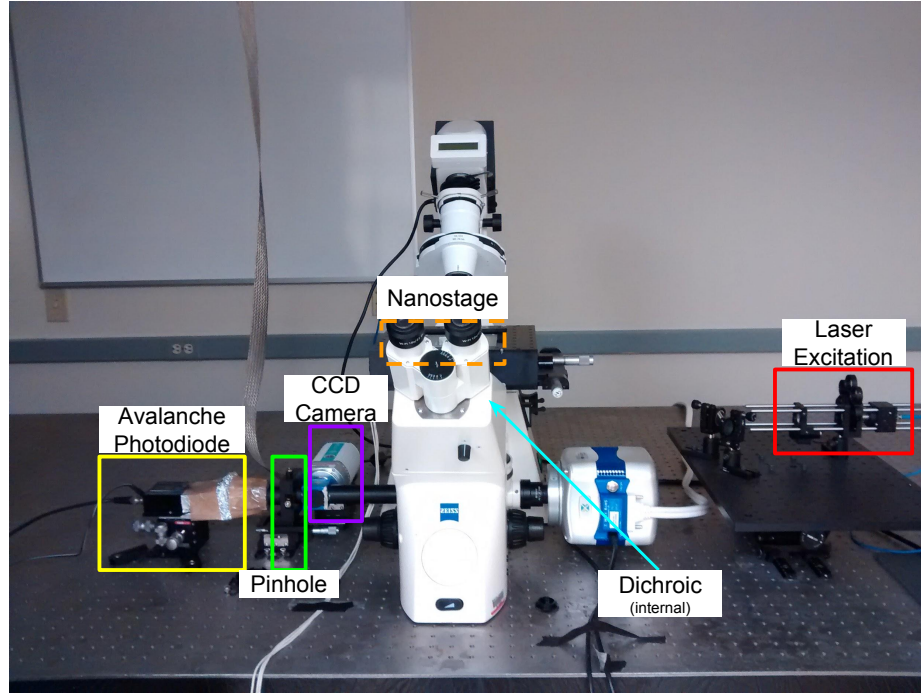


Figure 4-1: In image of the confocal microscope used for the experiment described in this work. The device is based upon a Zeiss Axiovert 200 inverted microscope which can operate in both widefield and confocal modes. The device contains an internal dichroic (not shown) which reflects the excitation source (shown in red) to a 3D piezoelectric nanostage (shown in dashed orange). The nanostage holds the specimen and can displace it in three dimensions. The fluorescence generated by the specimen is passed through the dichroic and is reflected to both the pinhole (shown in green) and the CCD camera (shown in purple) by a beam splitter. In confocal operation the avalanche photodiode (shown in yellow) measures the emitted light, whereas in widefield operation the CCD camera measures it.

described in Chapter 3 relies on an accurate measurement of the PSF. In this section, we describe how the PSF of the confocal microscope was measured and how it was modeled for the application described in Chapter 4.

The PSF of the confocal microscope was measured by performing a three-dimensional raster scan of a fixed, fluorescent point emitter. Quantum dots (Qdot 625, Life Technologies) were adhered to a coverslip using Qmount mounting media (Qdot Qmount,

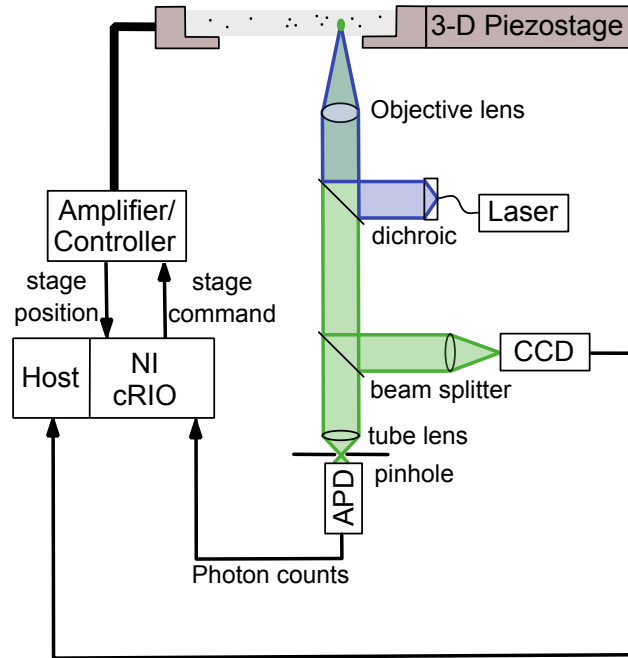


Figure 4.2: A block diagram of the optical path for the microscope described in this work. The excitation light (shown in blue) is generated by a laser diode. The light is then reflected off a dichroic, passed through the objective lens, and focused onto the sample. The sample is held by a piezoelectric nanostage. The emitted fluorescence generated by the sample is collected by the objective and passed through the dichroic where it is focused onto a pinhole which is confocal with the laser excitation. The intensity of the emitted light is then measured by the avalanche photodiode. A real-time controller (here, an NI cRIO) observes the APD’s intensity measurement and, during tracking, generates real-time position commands to the piezostages. Note that although a beam-splitter reflects some of the emitted light onto a CCD camera, the image is recorded by a host computer and is not used during tracking.

Life Technologies) by following the manufacturer’s protocol. The slide of fixed quantum dots was attached to the sample holder and the laser power was set to $7 \mu\text{W}$. A raster scan was performed with a resolution of 30 nm in x and y and 50 nm in z with a range of $2 \mu\text{m}$ in all three axes. Intensity measurements were acquired by accumulating photons during a period of 1 ms.

We assumed the PSF took the form of a three-dimensional, rotated Gaussian function. The rotation is needed to capture misalignment between the optical axis and the z -axis of the nanopositioning stage used to move the sample relative to the focal volume. Mathematically, the PSF model was

$$F_{\text{PSF}}(\mathbf{x}, \mathbf{x}_c) = F_0 \exp\left(-\frac{1}{2}(\mathbf{x} - \mathbf{x}_c)^T R(\psi)^T \Sigma^{-1} R(\psi) (\mathbf{x} - \mathbf{x}_c)\right), \quad (4.1)$$

where F_0 is the peak intensity, $\mathbf{x}_c = [x_c, y_c, z_c]^T$ denotes the particle center, $\psi = [\psi_x, \psi_y, \psi_z]^T$ denotes the rotation angles of the PSF, and $\Sigma = \text{diag}(\sigma_x^2, \sigma_y^2, \sigma_z^2)$ represents a diagonal matrix of widths. The rotation matrix $R(\psi)$ describes a ZYX rotation about the particle center such that, with some abuse of notation,

$$R(\psi) = \begin{bmatrix} \cos(\psi_z) & \sin(\psi_z) & 0 \\ -\sin(\psi_z) & \cos(\psi_z) & 0 \\ 0 & 0 & 1 \end{bmatrix} \begin{bmatrix} \cos(\psi_y) & 0 & \sin(\psi_y) \\ 0 & 1 & 0 \\ -\sin(\psi_y) & 0 & \cos(\psi_y) \end{bmatrix} \begin{bmatrix} 1 & 0 & 0 \\ 0 & \cos(\psi_x) & \sin(\psi_x) \\ 0 & -\sin(\psi_x) & \cos(\psi_x) \end{bmatrix}, \quad (4.2)$$

The following parameters were fit to the acquired data using MATLAB's `nlinfit` method: F_0 , x_c , y_c , z_c , σ_x , σ_y , σ_z , ψ_x , ψ_y , ψ_z . The relevant estimated parameters were $\hat{\sigma}_x = 216$ nm, $\hat{\sigma}_y = 270$ nm, $\hat{\sigma}_z = 533$ nm, $\hat{\psi}_x = 11.3^\circ$, $\hat{\psi}_y = -52.2^\circ$, and $\hat{\psi}_z = 131.6^\circ$.

The resulting fit can be visualized in three dimensions (Fig. 4.3) and in two dimensions (Fig. 4.4). Specifically, Fig. 4.3 compares the data and the model side-by-side and defines three mutually-orthogonal planes (denoted by the colors green, orange, and magenta) that are formed by rotating the standard Cartesian unit vectors centered about the estimated particle center using the estimated rotations. These planes are relevant to the images displayed in Fig. 4.4 where cross sections of the model and data are compared.

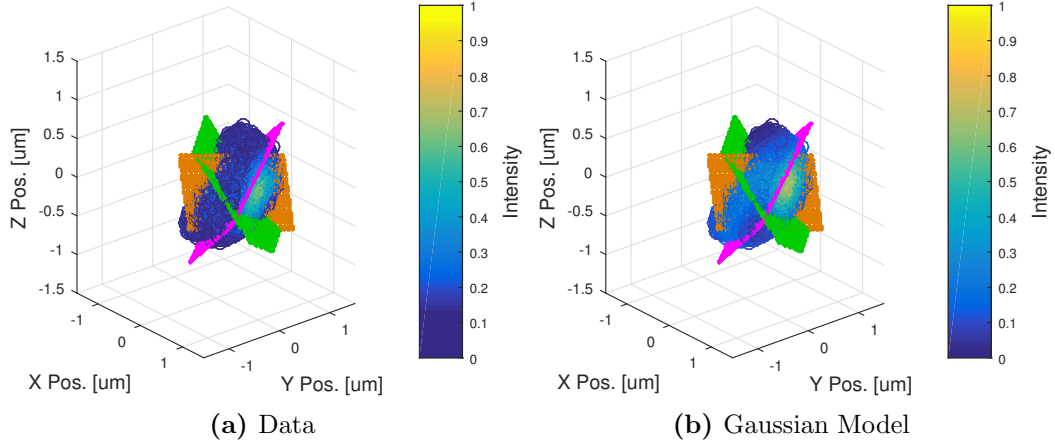


Figure 4.3: Three-dimensional point spread function (PSF) measurements (left) and the corresponding Gaussian model (right) which was calculated by a nonlinear least-squares fit. Three planes are shown in magenta, orange, and green which enable the depiction of the cross sections shown in Fig. 4.4. These planes were determined by calculating the planes through the estimated particle center, given by the least-squares fit, and normal vectors specified by the three standard Cartesian unit vectors transformed via (4.2) and the three rotations $(\hat{\psi}_x, \hat{\psi}_y, \hat{\psi}_z)$, also given by the least-squares fit. The intensity values in the measured PSF (left) are normalized by the maximum measured intensity value, and the intensity values in the model PSF (right) are normalized by the peak intensity value calculated by least-squares fit.

4.3 Experiment Details

To demonstrate the tracking method, unconjugated quantum dots (QD) were tracked in an agarose hydrogel. To prepare the sample, 1.745 g of water and 0.062 g of powdered agarose (A9539, Sigma-Aldrich) were combined and heated until boiling. Subsequently, 1.924 g of glycerol (G31-1, Fisher Scientific) was added to the mixture in addition to 200 nL of a solution (2 nM per 50 mM borate) of carboxyl QDs (Qdot 625, Life Technologies). The mixture was stirred for approximately one minute, poured onto a glass coverslip which was then adhered to a sample slide, and allowed to cool until it reached room temperature.

The hydrogel sample was fixed to the piezoelectric nanostage via a sample holder.

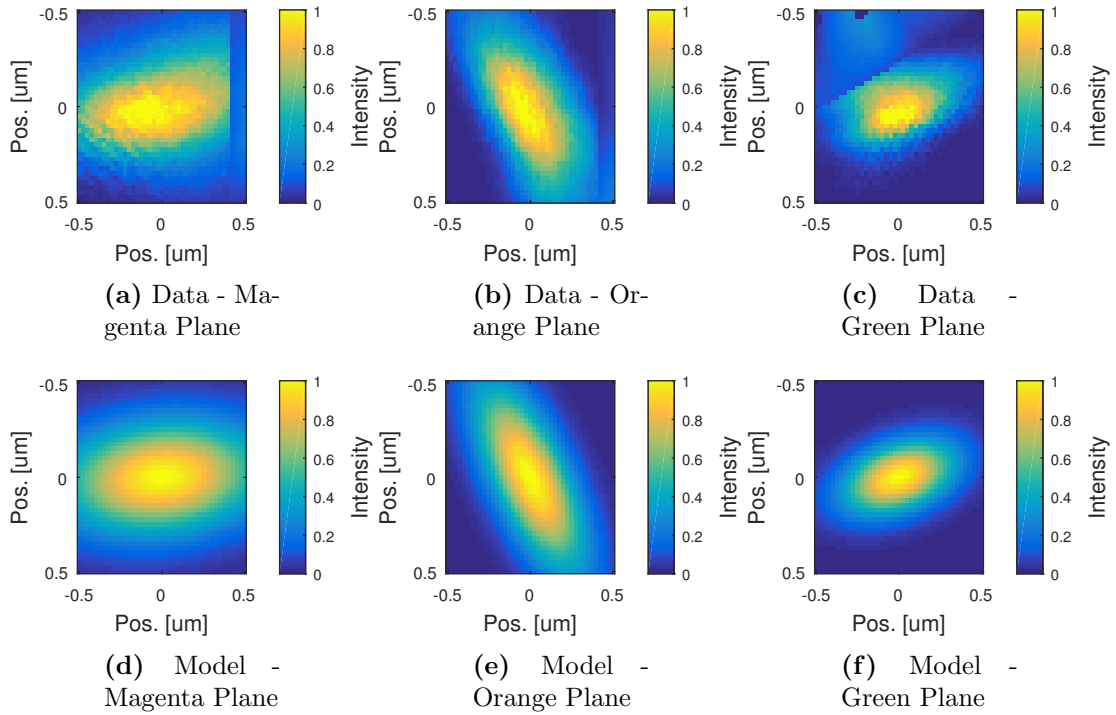


Figure 4-4: Two-dimensional point spread function measurements (top row) and their corresponding Gaussian models (bottom row) through the three planes depicted in Fig. 4-3.

The laser power was set to $25 \mu\text{W}$ as measured after the beam expander and prior to the collimating optics. The intensity measurement was formed by periodically accumulating APD output pulses over a time duration of 1 ms. This duration was selected to be fast relative to the (expected) motion while still providing significant signal in each integration period. It is, however, a user-selectable parameter limited primarily by the output emission rate and the capabilities of the avalanche photodiode. Prior to tracking, the background noise was measured to be approximately 4 counts per millisecond in a vacant section of the sample. A portion of the sample was then selected with a concentration of fewer than 5 QDs per $1 \mu\text{m}^2$. Tracking was initiated when the accumulated intensity reached a value higher than 40 count / ms and was subsequently disabled when the intensity dropped to zero. The tracking al-

gorithm parameters were set to have a scanning radius of $\bar{R} = 50$ nm, a convergence gain of $K_p = 5 \times 10^{-4}$, and angular frequencies $\omega_1 = 15$ Hz and $\omega_2 = 7$ Hz.

4.4 Experiment Results

The experimental output from the tracking algorithm is the position feedback from the nanostage; it is not the position of the particle. As such, we employ the SMC-EM method described in Chapter 3 to infer the position of the particle. In this work, we assumed that the particle moved via a combination of unconfined anisotropic diffusion and flow as described in Sec. 3.3.2; thus, the motion parameters to be estimated included three diffusion coefficients and three velocities. In addition, we assumed the observation model was in the form of the Poisson shot noise model presented in Sec. 3.3.6. The PSF model was the rotated Gaussian as described in Sec. 4.2. The peak intensity of the PSF was assumed unknown and was estimated in addition to the six aforementioned motion parameters. The background noise was assumed to be an additive constant to the rate of the Poisson process and was set to the previously measured value of 4 counts / ms.

An experimental output of length 50 s was processed by the SMC-EM algorithm using 50 Monte Carlo estimates. We note that the length of the trajectory was limited by the amount of memory required by the SMC-EM algorithm and was not due to loss of tracking during the experiment. After 1000 iterations of the SMC-EM algorithm, the estimated diffusion coefficients were $(0.139, 0.082, 0.087) \mu\text{m}^2/\text{s}$ and the estimated velocities were $(-0.009, -0.001, 0.003) \mu\text{m}/\text{s}$, in x , y , and z , respectively; the peak intensity was 1376 count / ms. The estimated particle location, depicted in blue in Fig. 4-5, was determined by calculating the weighted sample mean (3.39) of the estimated posterior density as a function of time; this is plotted relative to the measured focal volume position, depicted in black. Additionally, Fig. 4-5 shows the

measured intensity, in black, in relation to the theoretical intensity, in blue, which was determined by evaluating the Gaussian model as a function of the difference of the measured focal volume position and the estimated particle location. A three-dimensional plot of the inferred particle position is given in Fig. 4-6.

The inferred position of the particle during the experiment appears to suggest that it is confined within an ellipsoidal region with semi-major lengths between 250 to 500 nm. It is well known that the structure of agar hydrogels is comprised of anti-symmetric double helices and that agar forms fiber bundles through intermolecular hydrogen bonding (Pines and Prins, 1973; Bulone and San Biagio, 1991). It has also been observed (via fluorescence correlation spectroscopy and small angle neutron scattering experiments) that there is a pore size distribution ranging from 1 nm to 900 nm (Fatin-Rouge et al., 2003; Fatin-Rouge et al., 2006). The inferred position therefore appears consistent with what has been observed in the literature. It is important to note, however, that the medium used in the presented work was not a pure hydrogel since it was diluted with glycerol. It has been observed that the addition of glycerol to an agar hydrogel changes its structure (Boral and Bohidar, 2012). We further note that concentrated solutions of quantum dots tend to contain a relatively large concentration of aggregate crystals. Since the solution of quantum dots was not centrifuged prior to the experiment and since blinking was not observed in the measured intensity, it is very likely that the tracked fluorescent particle was much larger than expected for a single quantum dot (which is approximately 20-30 nm in diameter).

4.5 Summary

In this chapter we have demonstrated both the tracking algorithm described in Chapter 2 and the inference method described in Chapter 3 in an experimental setting.

Specifically, we implemented the tracking algorithm in a real-time controller and used it to track a quantum dot with a confocal microscope. Since the tracking algorithm does not perform online localization, an offline inference method may be used to estimate the position of the particle. In this chapter, we employed the SMC-EM algorithm and determined that the particle appeared to be confined within the hydrogel.

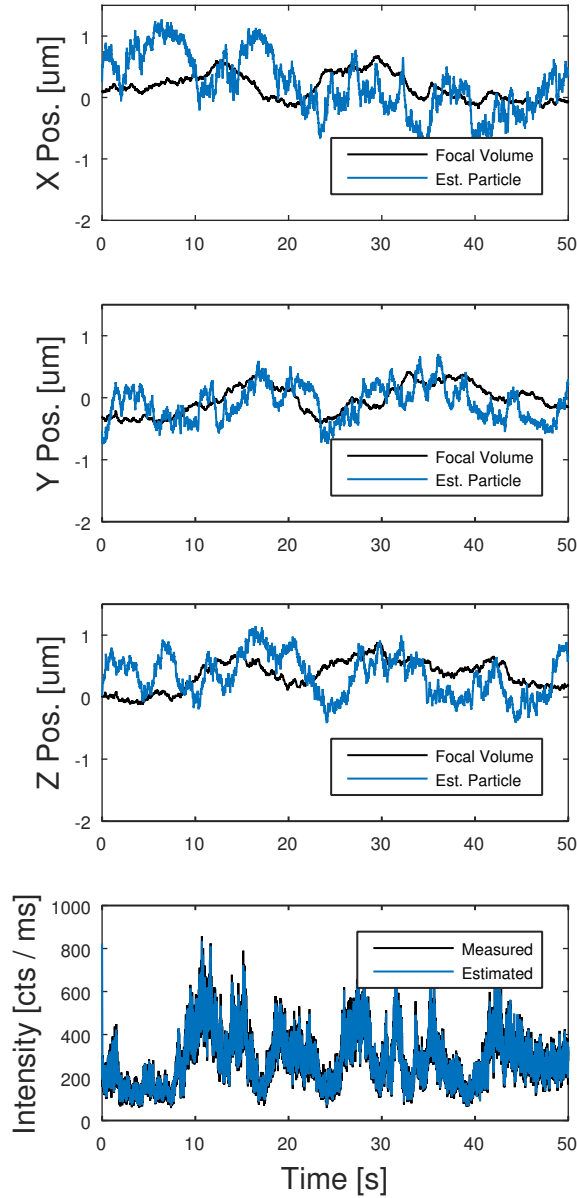


Figure 4.5: The inferred three-dimensional position of a quantum dot, in blue, diffusing in a hydrogel relative to the position of the focal volume, in black, which followed the particle in real-time using the extremum seeking method described in this work. The particle position was inferred by employing the SMC-EM algorithm described in Chapter 3. In the bottom graph, the measured intensity, in black, is shown in relation to the theoretical intensity, in blue, which was calculated by evaluating a Gaussian model of the point spread function (PSF) as a function of the inferred particle position and the measured focal volume position.

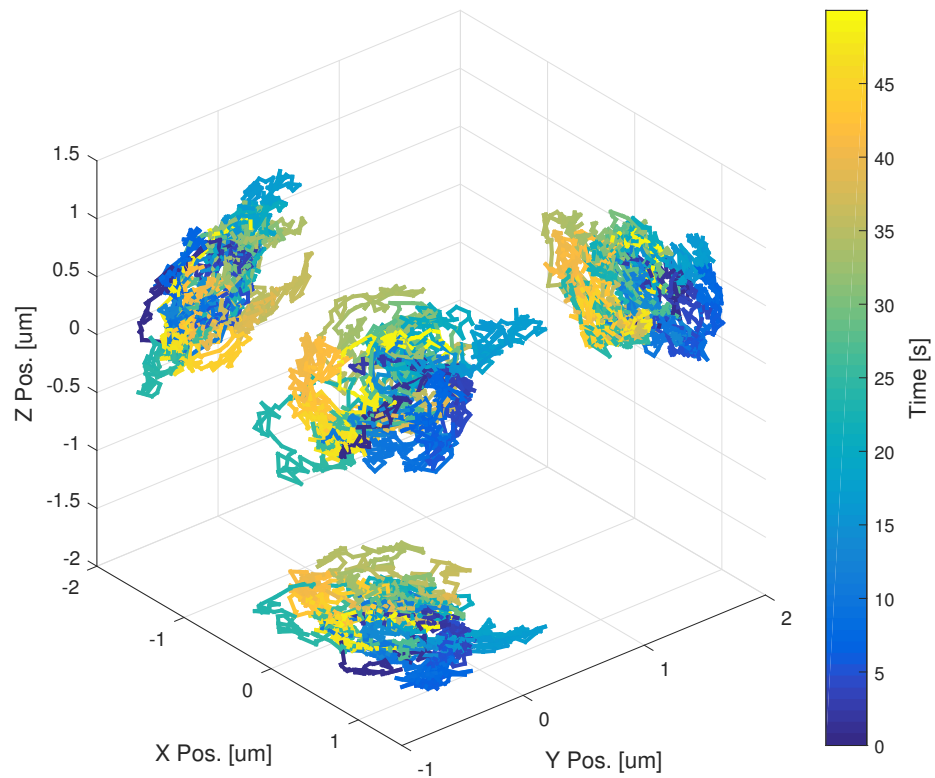


Figure 4-6: The inferred three-dimensional trajectory of a quantum dot diffusing in a hydrogel as parametrized by time. The quantum dot was tracked in a confocal microscope using the method presented in this work; the resulting particle position was inferred using the SMC-EM algorithm described in Chapter 3.

Chapter 5

Summary and Future Directions

5.1 Summary

This thesis presented two primary contributions. First, an active tracking method was developed in Chapter 2 which can be used to follow fluorescent particles in three dimensions in a confocal microscope. Second, an inference method was described in Chapter 3 which can be used for both localization and parameter estimation for a wide variety of imaging modalities. Both methods were demonstrated in Chapter 4 where a quantum dot was tracked in an agar hydrogel.

The presented tracking algorithm is novel for several reasons. First, it is an active tracking method which requires no online localization and is computationally simple; thus, the method may be implemented in systems with severe real-time requirements with fast (*i.e.*, sub-millisecond) update rates). In addition, the method produces smooth trajectories and its performance may be adjusted in a straightforward manner using four distinct parameters. Moreover, the algorithm does not require any specific knowledge of the microscope's point spread function nor does it require any a priori knowledge of how the particle moves; it only makes the assumption that the point spread function has an isolated maximum that is coincident with the fluorescent particle. Lastly, the algorithm is scalable, can be implemented on a large variety of confocal microscopes, and does not require any specialized hardware.

In Chapter 2, we proved specific properties of the proposed tracking algorithm. Specifically, we considered two separate scenarios. In the first scenario, we considered

the case where the particle is stationary. We then showed the existence of an equilibrium trajectory that is sinusoidal and centered about the maximum of the point spread function. We then proved the stability of the equilibrium and then numerically characterized it using Floquet multipliers. The second scenario considered the case where the particle was moving according to a Brownian motion and the point spread function possessed bounded support. We then derived a metric for the expected tracking time and numerically characterized it via simulation. With these results, we then provided insight on parameter selection.

The proposed inference method, which was based on the work (Schön et al., 2011), solves many problems that currently exist within the common paradigm of particle tracking inference. The common paradigm, which is serial in nature, is limited by the fact that its localization step only produces point-estimates of the particle's position and does so without taking into account the entire set of measurements. In addition, many optimal methods for parameter estimation are limited to simplistic motion and noise models. Although regression to the mean squared displacement may offer the flexibility of estimating parameters for more complex motion models, a general statistical analysis for any motion but diffusion has not been considered. The method described in Chapter 3, however, produces a posterior probability density of the particle's location given the entire measurement history. In addition, it produces optimal estimates of model parameters that may correspond to a large variety of motion and observation models that are applicable to biological microscopy. For example, we demonstrated the method via simulation in the context of tracking free, confined, and tethered diffusions.

To show the effectiveness of both tracking and inference methods, in Chapter 4 we tracked a quantum dot in an agar hydrogel and used the proposed inference method to estimate its position. We observed that the particle was confined to an ellipsoidal

region within the gel.

5.2 Future Directions

Both of the proposed tracking and inference methods show great promise in their applicability to single particle tracking in fluorescence microscopy. However, there are several uncertainties and open questions which still need to be addressed.

5.2.1 Discrete-Time Analysis of Stability

In Chapter 2, a continuous-time argument was given for the stability of the tracking algorithm. In the context of particle tracking, however, the intensity measurement is obtained at discrete time instances. Although an argument can be made that the continuous-time argument well-approximates that for a discrete-time system that is sampled fast-enough, this argument may not be valid in this case. To see this, recall that the intensity measurement is formed by accumulating photons over a periodic window; thus, as the period decreases, fewer photons are acquired and the signal to noise ratio decreases. Consequently, increasing the sample rate not only may inadvertently reduce the effectiveness of the tracking, but it could also reduce the precision of localization. Thus, a discrete-time analysis should be performed to determine how the sampling rate affects the performance of both procedures.

5.2.2 Accounting for Motion Blur

One frequently encounters low frame rates in the widefield imaging paradigm. This is due to several factors, including the efficiency of the fluorophores relative to the efficiency of the detector (which governs the signal to noise ratio, and thus the localization precision), as well as hardware limitations of the detector itself. Acquiring images of moving features, however, may produce an imaging artifact known as motion blur which can irreversibly reduce the precision of localization. Within the common

inference paradigm, methods producing optimal estimates for diffusion coefficients can directly compensate for this phenomenon. Unfortunately, in its current form, the SMC-EM algorithm cannot compensate for motion blur because it produces a temporal correlation between subsequent measurements and thus violates the assumption that the motion is Markov. Discrete-sampling of integrated diffusions was considered in (Gloter, 2000) and it was shown that it could be approximated by a Gaussian ARMA(1,1) process; thus, if the SMC-EM algorithm could be extended to this simple case, then it could at least approximately compensate for it. Parameter estimation for discrete-sampled integrated diffusions was also considered in (Ditlevsen and Sørensen, 2004), but the approach was not based on Sequential Monte Carlo methods and, despite producing maximum likelihood estimates, it would fail to produce a posterior density of the particle's location.

5.2.3 Non-Markovian Dynamics

When observed particle motion deviates from a standard diffusion, it is often termed by experimentalists to be *anomalous*. The concept of anomalous diffusion, which has given rise to the abstract terms subdiffusion and superdiffusion, describes a random process that fluctuates according to $\sigma^2 \propto Dt^\alpha$ rather than $\sigma^2 \propto Dt$. The α parameter determines whether it is a subdiffusion ($\alpha < 1$) or a superdiffusion ($\alpha > 1$) and can be easily estimated via regression to the mean squared displacement. The desire to understand the physical meaning behind anomalous diffusion has introduced several new models to the field of biology; these models include fractional Brownian motion as well as continuous-time random walks. Since these processes are inherently non-Markov, they cannot be incorporated into the SMC-EM algorithm. Thus, the utility of the SMC-EM algorithm could be significantly extended by allowing for non-Markovian dynamics.

Appendix A

Summary of Sequential Monte Carlo Methods

Here we describe the two Sequential Monte Carlo (SMC) methods described in Chapter 3 which constitute the expectation step of the SMC-EM algorithm. Specifically, two algorithms, namely the Sampling Importance Resampling (SIR) algorithm and the Forward-Filtering Backward-Smoothing (FFBS) algorithm, are described.

A.1 Sampling Importance Resampling Algorithm

The Sampling Importance Resampling (SIR) algorithm calculates the filtered posterior densities by performing three distinct operations - sampling, weighting, and resampling - at each time step. The sampling step is dependent on the discrete time index k . Starting at $k = 1$, a total of M random samples are generated from the initial condition model (3.1) such that

$$\tilde{\mathbf{x}}_{1|1,e}^i \sim p_{\hat{\theta}_e}^{\text{Init}}(\mathbf{x}_{\mathbf{p},1}). \quad (\text{A.1})$$

Here, $\tilde{\mathbf{x}}_{k|k,e}^i \in \mathbb{R}^{n_x}$ denotes the i th randomly generated estimate of the state (for $i = 1, \dots, M$) at EM iteration e at time step k and given measurements $I_{1:k}^{1:P}$; the “ \mathbf{p} ” subscript is implied and has been omitted to simplify notation. Additionally, the tilde denotes that the sample has not yet been resampled, a process which is discussed below. Instead, if $k > 1$ then the M random samples are generated according to the

motion model (3.2) such that

$$\tilde{\mathbf{x}}_{k|k,e}^i \sim p_{\hat{\theta}_e}^{\text{Mot}}(\mathbf{x}_{\mathbf{p},k} | \mathbf{x}_{k-1|k-1,e}^i), \quad (\text{A.2})$$

for $i = 1, \dots, M$; note that the samples are randomly generated with respect to the resampled randomly generated samples from the previous timestep.

The weighting step assesses the likelihood of the estimates generated in the sampling step relative to the measurements. For each individual timestep $k = 1, \dots, N$, each random sample i is weighted according to the observation model (3.3). In other words,

$$\tilde{w}_{k|k,e}^i \propto p_{\hat{\theta}_e}^{\text{Obs}}(I_k^{1:P} | \tilde{\mathbf{x}}_{k|k,e}^i), \quad (\text{A.3})$$

for $i = 1, \dots, M$. The weights are then scaled so that their sum over i is unity so as to create a discrete probability measure over the randomly generated estimates.

The resampling step then generates a new set of M samples according to the measure defined in the weighting step. Although there are many popular methods by which one may resample a finite set (Douc and Cappé, 2005), we employ the multinomial resampling method for its simplicity. Here, M new estimates j were generated such that

$$\mathbb{P}(\mathbf{x}_{k|k,e}^j = \tilde{\mathbf{x}}_{k|k,e}^i) = \tilde{w}_{k|k,e}^i, \quad (\text{A.4})$$

with corresponding weights $w_{k|k,e}^j$ set to $1/M$.

To summarize, the SIR algorithm performs three operations for each time step k before proceeding to the next time step: first, M samples are randomly generated via (A.1) (if $k = 1$) or (A.2) (if $k > 1$); secondly, the samples are weighted by the observation model according to (A.3); finally, M new samples are generated according to (A.4). Thus, the output of the SIR algorithm is the approximate posterior density

$p_{\hat{\theta}_e}(\mathbf{x}_{\mathbf{p},k}|I_{1:k}^{1:P})$ for $k = 1, \dots, N$.

A.2 Forward-Filtering Backward-Smoothing Algorithm

The FFBS algorithm is a deterministic procedure (unlike SIR, which is stochastic) which calculates the posterior densities $p_{\hat{\theta}_e}(\mathbf{x}_{\mathbf{p},k}|I_{1:N}^{1:P})$ for $k = 1, \dots, N$. To do so, it operates backward in time on the estimates produced by SIR and produces a new series of “smoothed” weights; the algorithm does not produce a new series of locations and takes $\mathbf{x}_{k|k,e}^i = \mathbf{x}_{k|N,e}^i$. Note that at $k = N$, the smoothed weights are equivalent to those produced by SIR. Proceeding *backward* in time, the smoothed weights are calculated according to

$$w_{k|N,e}^i = w_{k|k,e}^i \sum_{m=1}^M w_{k+1|N,e}^m \frac{p_{\hat{\theta}_e}^{\text{Mot}}(\mathbf{x}_{k+1|k+1,e}^m | \mathbf{x}_{k|k,e}^i)}{v_k^m}, \quad (\text{A.5a})$$

$$v_k^m \triangleq \sum_{j=1}^M w_{k|k,e}^j p_{\hat{\theta}_e}^{\text{Mot}}(\mathbf{x}_{k+1|k+1,e}^m | \mathbf{x}_{k|k,e}^j), \quad (\text{A.5b})$$

for $k = (N-1), \dots, 1$. We also require an approximation of the pairwise joint density (3.9); these were calculated in (Schön et al., 2011) to be

$$w_{k|N,e}^{ij} = \frac{w_{k|k,e}^i w_{k+1|N,e}^j p_{\hat{\theta}_e}^{\text{Mot}}(\mathbf{x}_{k+1|k+1,e}^j | \mathbf{x}_{k|k,e}^i)}{\sum_{l=1}^M w_{k|k,e}^l p_{\hat{\theta}_e}^{\text{Mot}}(\mathbf{x}_{k+1|k+1,e}^j | \mathbf{x}_{k|k,e}^l)}. \quad (\text{A.6})$$

References

- Abbe, E. (1873). Beiträge zur theorie des mikroskops und der mikroskopischen wahrnehmung. *Archiv für mikroskopische Anatomie*, 9(1):413–418.
- Andersson, S. B. (2008). Localization of a fluorescent source without numerical fitting. *Optics Express*, 16(23):18714–18724.
- Andersson, S. B. (2011). A nonlinear controller for three-dimensional tracking of a fluorescent particle in a confocal microscope. *Applied Physics B*, 104(1):161–173.
- Ando, T. (2012). High-speed atomic force microscopy coming of age. *Nanotechnology*, 23(6):062001.
- Ashley, T. T. and Andersson, S. B. (2015a). Estimating dynamics in particle tracking microscopy using nonlinear system identification. In *Proceedings of the 17th IFAC Symposium on System Identification*, pages 805–810.
- Ashley, T. T. and Andersson, S. B. (2015b). Method for simultaneous localization and parameter estimation in particle tracking experiments. *Physical Review E*, 92(5):052707.
- Ashley, T. T. and Andersson, S. B. (2016). A control law for seeking an extremum of a three-dimensional scalar potential field. In *Proceedings of the American Control Conference*.
- Ashley, T. T., Chan-Tse, C., and Andersson, S. B. (2012). Validation of a nonlinear reactive control law for three-dimensional particle tracking in confocal microscopy. In *IEEE Conference Decision and Control*, pages 2328–2333.
- Baronov, D. and Baillieul, J. (2011). A motion description language for robotic reconnaissance of unknown fields. *European Journal of Control*, 17(5–6):512–525.
- Beausang, J. F., Zurla, C., Finzi, L., Sullivan, L., and Nelson, P. C. (2007). Elementary simulation of tethered Brownian motion. *American Journal of Physics*, 75(6):520–523.
- Berglund, A. J. (2010). Statistics of camera-based single-particle tracking. *Physical Review E*, 82(1):011917.

- Betzig, E. and Chichester, R. J. (1993). Single molecules observed by near-field scanning optical microscopy. *Science*, 262(5138):1422–1425.
- Biermann, B., Sokoll, S., Klueva, J., Missler, M., Wiegert, J., Sibarita, J.-B., and Heine, M. (2014). Imaging of molecular surface dynamics in brain slices using single-particle tracking. *Nature Communications*, 5.
- Boral, S. and Bohidar, H. (2012). Effect of water structure on gelation of agar in glycerol solutions and phase diagram of agar organogels. *The Journal of Physical Chemistry B*, 116(24):7113–7121.
- Born, M. and Wolf, E. (1999). *Principles of Optics: Electromagnetic Theory of Propagation, Interference and Diffraction of Light*. Cambridge University Press, Cambridge, 7th edition.
- Brockett, R. W. (2015). *Finite Dimensional Linear Systems*. Classics in Applied Mathematics. SIAM, Philadelphia.
- Bulone, D. and San Biagio, P. L. (1991). Microgel regions in dilute agarose solutions: the notion of non-gelling concentration, and the role of spinodal demixing. *Chemical Physics Letters*, 179(4):339–343.
- Butterworth, J. A., Pao, L. Y., and Abramovitch, D. Y. (2010). Adaptive-delay combined feedforward/feedback control for raster tracking with applications to AFMs. In *Proceedings of the American Control Conference*, pages 5738–5744. IEEE.
- Cang, H., Xu, C. S., Montiel, D., , and Yang, H. (2007). Guiding a confocal microscope by single fluorescent nanoparticles. *Optics Letters*, 32(18):2729–2732.
- Cappe, O., Godsill, S. J., and Moulines, E. (2007). An overview of existing methods and recent advances in sequential Monte Carlo. *Proceedings of the IEEE*, 95(5):899–924.
- Carslaw, H. S. and Jaeger, J. C. (1959). *Conduction of Heat in Solids*. Clarendon Press, Oxford, 2nd edition.
- Chao, J., Ward, E. S., and Ober, R. J. (2012). Fisher information matrix for branching processes with application to electron-multiplying charge-coupled devices. *Multidimensional Systems and Signal Processing*, 23(3):349–379.
- Cheezum, M. K., Walker, W. F., and Guilford, W. H. (2001). Quantitative comparison of algorithms for tracking single fluorescent particles. *Biophysical Journal*, 81(4):2378–2388.

- Chenouard, N., Smal, I., de Chaumont, F., Maka, M., Sbalzarini, I. F., Gong, Y., Cardinale, J., Carthel, C., Coraluppi, S., Mark Winter, A. R. C., Godinez, W. J., Rohr, K., Kalaidzidis, Y., Liang, L., Duncan, J., Shen, H., Xu, Y., Magnusson, K. E. G., Jaldn, J., Blau, H. M., Paul-Gilloteaux, P., Roudot, P., Kervrann, C., Waharte, F., Jean-Yves Tinevez, S. L. S., Joost Willemse, K. C., van Wezel, G. P., Dan, H.-W., Tsai, Y.-S., Carlos Ortiz de Solrzano, J.-C. O.-M., and Meijering, E. (2014). Objective comparison of particle tracking methods. *Nature Methods*, 11(3):281–289.
- Cochran, J. and Krstic, M. (2009). Nonholonomic source seeking with tuning of angular velocity. *IEEE Transactions on Automatic Control*, 54(4):717–731.
- Cohen, A. E. and Moerner, W. (2005). Method for trapping and manipulating nanoscale objects in solution. *Applied Physics Letters*, 86(9):093109.
- Dempster, A. P., Laird, N. M., and Rubin, D. B. (1977). Maximum likelihood from incomplete data via the EM algorithm. *Journal of the Royal Statistical Society Series B (Methodological)*, 39(1):1–38.
- Ditlevsen, S. and Sørensen, M. (2004). Inference for observations of integrated diffusion processes. *Scandinavian Journal of Statistics*, 31(3):417–429.
- Dormand, J. R. and Prince, P. J. (1980). A family of embedded Runge-Kutta formulae. *Journal of Computational and Applied Mathematics*, 6:19–26.
- Douc, R. and Cappé, O. (2005). Comparison of resampling schemes for particle filtering. In *Proceedings of the 4th International Symposium on Image and Signal Processing and Analysis*, pages 64–69. IEEE.
- Doucet, A., de Freitas, N., and Gordon, N., editors (2001). *Sequential Monte Carlo Methods in Practice*. Springer, New York.
- Doucet, A. and Johansen, A. M. (2011). A tutorial on particle filtering and smoothing: Fifteen years later. In Crisan, D. and Rozovskiĭ, B., editors, *The Oxford Handbook of Nonlinear Filtering*, pages 656–704. Oxford University Press, New York.
- Driscoll, R. J., Youngquist, M. G., and Baldeschwieler, J. D. (1990). Atomic-scale imaging of DNA using scanning tunnelling microscopy. *Nature*, 346(6281):294–296.
- Fatin-Rouge, N., Milon, A., Buffle, J., Goulet, R. R., and Tessier, A. (2003). Diffusion and partitioning of solutes in agarose hydrogels: the relative influence of electrostatic and specific interactions. *The Journal of Physical Chemistry B*, 107(44):12126–12137.

- Fatin-Rouge, N., Wilkinson, K. J., and Buffle, J. (2006). Combining small angle neutron scattering (SANS) and fluorescence correlation spectroscopy (FCS) measurements to relate diffusion in agarose gels to structure. *The Journal of Physical Chemistry B*, 110(41):20133–20142.
- Fuller, S. D., Wilk, T., Gowen, B. E., Kräusslich, H.-G., and Vogt, V. M. (1997). Cryo-electron microscopy reveals ordered domains in the immature HIV-1 particle. *Current Biology*, 7(10):729–738.
- Funatsu, T., Harada, Y., Tokunaga, M., Saito, K., Yanagida, T., et al. (1995). Imaging of single fluorescent molecules and individual ATP turnovers by single myosin molecules in aqueous solution. *Nature*, 374(6522):555–559.
- Gloter, A. (2000). Discrete sampling of an integrated diffusion process and parameter estimation of the diffusion coefficient. *ESAIM: Probability and Statistics*, 4:205–227.
- Graczyk, P. and Jakubowski, T. (2008). Exit times and Poisson kernels of the Ornstein-Uhlenbeck diffusion. *Stochastic Models*, 24(2):314–337.
- Gu, M. (2000). *Advanced Optical Imaging Theory*. Springer, Berlin.
- Gustafsson, M. G. (2000). Surpassing the lateral resolution limit by a factor of two using structured illumination microscopy. *Journal of Microscopy*, 198(2):82–87.
- Han, J. J., Kiss, C., Bradbury, A. R. M., and Werner, J. H. (2012). Time-resolved, confocal single-molecule tracking of individual organic dyes and fluorescent proteins in three dimensions. *ACS Nano*, 6(10):8922–8932.
- Hell, S. W. and Wichmann, J. (1994). Breaking the diffraction resolution limit by stimulated emission: stimulated-emission-depletion fluorescence microscopy. *Optics Letters*, 19(11):780–782.
- Hess, S. T., Girirajan, T. P., and Mason, M. D. (2006). Ultra-high resolution imaging by fluorescence photoactivation localization microscopy. *Biophysical Journal*, 91(11):4258–4272.
- Huang, B., Wang, W., Bates, M., and Zhuang, X. (2008). Three-dimensional super-resolution imaging by stochastic optical reconstruction microscopy. *Science*, 319(5864):810–813.
- Juette, M. F. and Bewersdorf, J. (2010). Three-dimensional tracking of single fluorescent particles with submillisecond temporal resolution. *Nano Letters*, 10(11):4657–4663.

- Juette, M. F., Gould, T. J., Lessard, M. D., Mlodzianoski, M. J., Nagpure, B. S., Bennett, B. T., Hess, S. T., and Bewersdorf, J. (2008). Three-dimensional sub-100 nm resolution fluorescence microscopy of thick samples. *Nature Methods*, 5(6):527–529.
- Kao, H. P. and Verkman, A. S. (1994). Tracking of single fluorescent particles in three dimensions: use of cylindrical optics to encode particle position. *Biophysical Journal*, 64(3):1291–1300.
- Khalil, H. K. (2002). *Nonlinear Systems*. Prentice Hall, New Jersey, 3rd edition.
- Kloeden, P. E. and Platen, E. (1999). Numerical solution of stochastic differential equations. In Karatzas, I. and Yor, M., editors, *Applications of Mathematics: Stochastic Modelling and Applied Probability*, volume 23. Springer, Berlin.
- Lakadamyali, M., Rust, M. J., and Zhuang, X. (2004). Endocytosis of influenza viruses. *Microbes and Infection*, 6(10):929–936.
- Leang, K. K., Zou, Q., and Devasia, S. (2009). Feedforward control of piezoactuators in atomic force microscope systems. *IEEE Control Systems Magazine*, 29(1):70–82.
- Levi, V., Ruan, Q., Kis-Petikova, K., and Gratton, E. (2003). Scanning FCS, a novel method for three-dimensional particle tracking. *Biochemical Society Transactions*, 31(5):997–1000.
- Lindsten, F. and Schön, T. B. (2013). Backward simulation methods for monte carlo statistical inference. *Foundations and Trends in Machine Learning*, 6(1):1–143.
- Lust, K. (2001). Improved numerical Floquet multipliers. *International Journal of Bifurcation and Chaos*, 11(9):2389–2410.
- Macierzanka, A., Mackie, A. R., Bajka, B. H., Rigby, N. M., Nau, F., and Dupont, D. (2014). Transport of particles in intestinal mucus under simulated infant and adult physiological conditions: Impact of mucus structure and extracellular DNA. *PloS one*, 9(4):e95274.
- Martin, D. S., Forstner, M. B., and Käs, J. A. (2002). Apparent subdiffusion inherent to single particle tracking. *Biophysical Journal*, 83(4):2109–2117.
- Masai, J., Shibata, T., Kondo, S., and Ishiwata, S. (1991). Scanning tunneling microscopy of actin filament. *Journal of Vacuum Science & Technology B*, 9(2):1177–1179.
- McHale, K., Berglund, A. J., and Mabuchi, H. (2007). Quantum dot photon statistics measured by three-dimensional particle tracking. *Nano Letters*, 7(11):3535–3539.

- Michalet, X. (2010). Mean square displacement analysis of single-particle trajectories with localization error: Brownian motion in an isotropic medium. *Physical Review E*, 82(4):041914.
- Michalet, X. and Berglund, A. J. (2012). Optimal diffusion coefficient estimation in single-particle tracking. *Physical Review E*, 85(6):061916.
- Moran, S. E., Ulich, B. L., Elkins, W. P., Strittmatter, R. L., , and Deweert, M. J. (1997). Intensified ccd (ICCD) dynamic range and noise performance. *Proceedings of SPIE*, 3173:430–457.
- Nelson, P. (2013). *Biological Physics: Energy, Information, Life*. W. H. Freeman and Co., New York.
- Nelson, P. C., Zurla, C., Brogioli, D., Beausang, J. F., Finzi, L., and Dunlap, D. (2006). Tethered particle motion as a diagnostic of DNA tether length. *The Journal of Physical Chemistry B*, 110(34):17260–17267.
- Øksendal, B. (2013). *Stochastic Differential Equations: An Introduction with Applications*. Universitext. Springer, Heidelberg, 6th edition.
- Ortega, J. M. and Rheinboldt, W. C. (2000). *Iterative Solution of Nonlinear Equations in Several Variables*, volume 30 of *Classics in Applied Mathematics*. SIAM, Philadelphia.
- Parthasarathy, R. (2012). Rapid, accurate particle tracking by calculation of radial symmetry centers. *Nature Methods*, 9(7):724726.
- Pavani, S. R. P., Thompson, M. A., Biteen, J. S., Lord, S. J., Liu, N., Twieg, R. J., Piestun, R., and Moerner, W. E. (2009). Three-dimensional, single-molecule fluorescence imaging beyond the diffraction limit by using a double-helix point spread function. *Proceedings of the National Academy of Sciences*, 106(9):2995–2999.
- Pawitan, Y. (2001). *In All Likelihood: Statistical Modelling and Inference Using Likelihood*. Oxford University Press, Oxford.
- Pawley, J. B., editor (2006). *Handbook of Biological Confocal Microscopy*. Springer, New York, 3rd edition.
- Pines, E. and Prins, W. (1973). Structure-property relations of thermoreversible macromolecular hydrogels. *Macromolecules*, 6(6):888–895.
- Poor, H. V. and Hadjiliadis, O. (2008). *Quickest Detection*. Cambridge University Press, Cambridge.

- Prabhat, P., Ram, S., Ward, E. S., and Ober, R. J. (2004). Simultaneous imaging of different focal planes in fluorescence microscopy for the study of cellular dynamics in three dimensions. *IEEE Transactions on NanoBioscience*, 3(4):237–242.
- Press, W. H., Teukolsky, S. A., Vetterling, W. T., and Flannery, B. P. (2007). *Numerical Recipes: The Art of Scientific Computing*. Cambridge University Press, Cambridge, 3rd edition.
- Ragan, T., Huang, H., So, P., and Gratton, E. (2006). 3D particle tracking on a two-photon microscope. *Journal of Fluorescence*, 16(3):325–336.
- Rauch, H. E., Striebel, C. T., and Tung, F. (1965). Maximum likelihood estimates of linear dynamic systems. *AIAA Journal*, 3(8):1445–1450.
- Risken, H. (1996). *The Fokker-Planck Equation: Methods of Solution and Applications*. Springer, Berlin.
- Robert, C. P. and Casella, G. (2005). *Monte Carlo Statistical Methods*. Springer, New York.
- Rust, M. J., Bates, M., and Zhuang, X. (2006). Sub-diffraction-limit imaging by stochastic optical reconstruction microscopy (STORM). *Nature Methods*, 3(10):793–796.
- Sanjeev Arulampalam, M., Maskell, S., Gordon, N., and Clapp, T. (2002). A tutorial on particle filters for online nonlinear/non-Gaussian bayesian tracking. *IEEE Transactions on Signal Processing*, 50(2):174–188.
- Saxton, M. J. (1997). Single-particle tracking: the distribution of diffusion coefficients. *Biophysical Journal*, 72(4):1744–1753.
- Saxton, M. J. and Jacobson, K. (1997). Single-particle tracking: applications to membrane dynamics. *Annual Review of Biophysics and Biomolecular Structure*, 26(1):373–399.
- Schmidt, T., Schütz, G., Baumgartner, W., Gruber, H., and Schindler, H. (1996). Imaging of single molecule diffusion. *Proceedings of the National Academy of Sciences*, 93(7):2926–2929.
- Schön, T. B., Wills, A., and Ninness, B. (2011). System identification of nonlinear state-space models. *Automatica*, 47(1):39–49.
- Shechtman, Y., Weiss, L. E., Backer, A. S., Sahl, S. J., and Moerner, W. (2015). Precise three-dimensional scan-free multiple-particle tracking over large axial ranges with tetrapod point spread functions. *Nano Letters*, 15(6):4194–4199.

- Sheetz, M. P., Schindler, M., and Koppel, D. E. (1980). Lateral mobility of integral membrane proteins is increased in spherocytic erythrocytes. *Nature*, 285:510–512.
- Shen, Z. and Andersson, S. B. (2011). 3-D tracking of fluorescent nanoparticles in a confocal microscope. In *Proceedings of the 2011 50th IEEE Conference on Decision and Control and European Control Conference*, pages 5856–5861.
- Shen, Z. and Andersson, S. B. (2012). Optimal measurement constellation of the fluoroBancroft localization algorithm for position estimation in tracking confocal microscopy. *Mechatronics*, 22(3):320–326.
- Shtengel, G., Galbraith, J. A., Galbraith, C. G., Lippincott-Schwartz, J., Gillette, J. M., Manley, S., Sougrat, R., Waterman, C. M., Kanchanawong, P., Davidson, M. W., et al. (2009). Interferometric fluorescent super-resolution microscopy resolves 3D cellular ultrastructure. *Proceedings of the National Academy of Sciences*, 106(9):3125–3130.
- Shuang, B., Byers, C. P., Kisley, L., Wang, L.-Y., Zhao, J., Morimura, H., Link, S., and Landes, C. F. (2012). Improved analysis for determining diffusion coefficients from short, single-molecule trajectories with photoblinking. *Langmuir*, 29(1):228–234.
- Spall, J. C. (2012). Monte carlo computation of the fisher information matrix in non-standard settings. *Journal of Computational and Graphical Statistics*, 14(4):889–909.
- Tang, J., Akerboom, J., Vaziri, A., Looger, L. L., and Shank, C. V. (2010). Near-isotropic 3D optical nanoscopy with photon-limited chromophores. *Proceedings of the National Academy of Sciences*, 107(22):10068–10073.
- Thompson, R. E., Larson, D. R., and Webb, W. W. (2002). Precise nanometer localization analysis for individual fluorescent probes. *Biophysical Journal*, 82(5):2775–2783.
- Tichavský, P., Muravchik, C. H., and Nehorai, A. (1998). Posterior Cramér-Rao bounds for discrete-time nonlinear filtering. *IEEE Transactions on Signal Processing*, 46(5):1386–1396.
- Toprak, E., Balci, H., Blehm, B. H., and Selvin, P. R. (2007). Three-dimensional particle tracking via bifocal imaging. *Nano Letters*, 7(7):2043–2045.
- Trees, H. (1968). *Detection, Estimation, and Modulation Theory*. Wiley, New York.
- Tulsyan, A., Huang, B., Gopaluni, R. B., and Forbes, J. F. (2013). A particle filter approach to approximate posterior Cramér-Rao lower bound: The case of hidden states. *IEEE Transaction on Aerospace and Electronic Systems*, 49(4):2478–2495.

- Uhlenbeck, G. E. and Ornstein, L. S. (1930). On the theory of the Brownian motion. *Physical Review*, 36(5):823–841.
- Verhulst, F. (2005). *Methods and Applications of Singular Perturbations: Boundary Layers and Multiple Timescale Dynamics*. Springer, New York.
- Welsher, K. and Yang, H. (2014). Multi-resolution 3D visualization of the early stages of cellular uptake of peptide-coated nanoparticles. *Nature Nanotechnology*, 9(3):198–203.
- Yildiz, A., Forkey, J. N., McKinney, S. A., Ha, T., Goldman, Y. E., and Selvin, P. R. (2003). Myosin V walks hand-over-hand: single fluorophore imaging with 1.5-nm localization. *Science*, 300(5628):2061–2065.
- Yildiz, A., Tomishige, M., Vale, R. D., and Selvin, P. R. (2004). Kinesin walks hand-over-hand. *Science*, 303(5658):676–678.
- Yong, Y., Moheimani, S., Kenton, B. J., and Leang, K. (2012). Invited review article: High-speed flexure-guided nanopositioning: Mechanical design and control issues. *Review of scientific instruments*, 83(12):121101.
- Zhang, B., Zerubia, J., and Olivo-Marin, J.-C. (2007). Gaussian approximations of fluorescence microscope point-spread function models. *Applied Optics*, 46(10):1819–1829.

Trevor T. Ashley

260 Main St.
Apt. 403
Malden, MA 02148

Tel: 509-570-2579
Fax: 617-353-5866
E-mail: trevor.ashley@gmail.com

Education:

- 2016 Ph.D. in Mechanical Engineering
Boston University, Boston, Massachusetts, USA
- 2016 M.S. in Mechanical Engineering
Boston University, Boston, Massachusetts, USA
- 2009 B.S. in Engineering
Harvey Mudd College, Claremont, California, USA

Positions:

- 2012-2016 Graduate Research Assistant
Boston University, Boston, Massachusetts, USA
- 2013-2014 NSF GK-12 Fellow
Boston University, Boston, Massachusetts, USA
- 2011-2012 Graduate Teaching Assistant
Boston University, Boston, Massachusetts, USA
- 2009-2011 Control Systems Engineer
Electro Scientific Industries, Inc., Portland, Oregon, USA
- 2007-2009 Clay-Wolkin Fellow
Harvey Mudd College, Claremont, California, USA

Honors and Awards:

- 2011-2012 Teaching Fellow of the Year
Boston University, Boston, Massachusetts, USA
 - 2009 Departmental Honors
Harvey Mudd College, Claremont, California, USA
-

Publications:

Journal Articles Under Review:

1. T. T. Ashley and S. B. Andersson. Tracking Single Fluorescent Particles in Three Dimensions via Extremum Seeking. *Nano Letters*.
2. T. T. Ashley and S. B. Andersson. Tracking a Diffusing Three-Dimensional Source via Nonholonomic Extremum Seeking. *IEEE Transactions on Automatic Control*.

Journal Articles:

1. T. T. Ashley and S. B. Andersson. Method for Simultaneous Localization and Parameter Estimation in Particle Tracking Experiments. *Physical Review E*, no. 92, 052707, 2015.

Refereed Conference Articles:

1. T. T. Ashley and S. B. Andersson. A Control Law for Seeking an Extremum of a Three-Dimensional Scalar Potential Field. In *Proceedings of the American Control Conference*, Boston, Massachusetts, USA, 2016.
2. T. T. Ashley and S. B. Andersson. Estimating Dynamics in Particle Tracking Microscopy Using Nonlinear System Identification. In *Proceedings of the 17th IFAC Symposium on System Identification*, Beijing, China, 2015.
3. T. T. Ashley and S. B. Andersson. A Sequential Monte Carlo Framework for the System Identification of Jump Markov State Space Models. In *Proceedings of the American Control Conference*, Portland, Oregon, USA, 2014.
4. T. T. Ashley, C. Chan-Tse, and S. B. Andersson. Validation of a Nonlinear Reactive Control Law for Three-Dimensional Particle Tracking in Confocal Microscopy. In *Proceedings of the Conference on Decision and Control*, Maui, Hawaii, USA, 2012.
5. A. Joshi, T. Ashley, Y. R. Huang, A. L. Bertozzi. Experimental Validation of Cooperative Environmental Boundary Tracking with On-Board Sensors. In *Proceedings of the American Control Conference*, St. Louis, Missouri, USA, 2009.

Poster Sessions:

1. “High Speed AFM Through Non-Raster Scanning and High Speed Actuation,” Biophysical Society, 2016.
2. “A Method for Estimating Unknown Parameters from Particle Tracking Experiments,” Biophysical Society, 2016.
3. “A Sequential Monte Carlo Method for Identifying Motion Parameters from Particle Tracking Trajectories,” Biophysical Society, 2014.
4. “Three-Dimensional Tracking of Fluorescent Particles in Confocal Microscopy,” Biophysical Society, 2013.

Invited Presentations:

1. Quantitative Bioimaging. Albuquerque, New Mexico, USA. January 10, 2014.

Professional Membership and Service:

- Student member: IEEE and Biophysical Society.
- Reviewer: IEEE Transactions on Automatic Control, Optics Letters, American Control Conference, IEEE Conference on Decision and Control, IEEE Multi-Conference on Systems and Control.

University Service:

- High School Mentorship and Outreach: Nanocamp (Upward Bound), RISE, AMS Materials Day, U-Design.